(12) INTERNATIONAL APPLICATION PUBLISHED UNDER THE PATENT COOPERATION TREATY (PCT)

(19) **World Intellectual Property Organization**
International Bureau

PCT

(43) **International Publication Date**
3 June 2011 (03.06.2011)

(10) **International Publication Number**
WO 2011/066570 A2

(51) **International Patent Classification**:
H01L 31/042 (2006.01) *H01L 31/0236* (2006.01)

(21) **International Application Number**:
PCT/US2010/058422

(22) **International Filing Date**:
30 November 2010 (30.11.2010)

(25) **Filing Language**: English

(26) **Publication Language**: English

(30) **Priority Data**:
61/265,297 30 November 2009 (30.11.2009) US
61/265,306 30 November 2009 (30.11.2009) US
61/313,654 12 March 2010 (12.03.2010) US

(71) **Applicant** *(for all designated States except US)*: **CALIFORNIA INSTITUTE OF TECHNOLOGY** [US/US]; 1200 E. California Blvd., M/C 210-85, Pasadena, California 91125 (US).

(72) **Inventors; and**
(75) **Inventors/Applicants** *(for US only)*: **KELZENBERG, Michael, D.** [US/US]; 124 N. Wilson Ave., Apt. 5, Pasadena, California 91106 (US). **ATWATER, Harry, A.** [US/US]; 1945 Leman St., South Pasadena, California 91030 (US). **BIGGS, Ryan, M.** [US/US]; c/o California Institute of Technology, 1200 E. California Blvd. M/C 128-95, Pasadena, California 91125 (US). **BOETTCHER, Shannon, W.** [US/US]; c/o California Institute of Technology, 1200 E. California Blvd. M/C 127-72, Pasadena, California 91125 (US). **LEWIS, Nathan, S.** [US/US]; 4808 Gould Avenue, La Canada, California 91011 (US). **PETYKIEWICZ, Jan, A.** [US/US]; c/o California Institute of Technology, 1200 E. California Blvd. MSC 664, Pasadena, California 91125 (US).

(74) **Agents**: **STEINFL & BRUNO** et al.; 301 N. Lake Avenue, Suite 810, Pasadena, California 91101 (US).

(81) **Designated States** *(unless otherwise indicated, for every kind of national protection available)*: AE, AG, AL, AM, AO, AT, AU, AZ, BA, BB, BG, BH, BR, BW, BY, BZ, CA, CH, CL, CN, CO, CR, CU, CZ, DE, DK, DM, DO, DZ, EC, EE, EG, ES, FI, GB, GD, GE, GH, GM, GT, HN, HR, HU, ID, IL, IN, IS, JP, KE, KG, KM, KN, KP, KR, KZ, LA, LC, LK, LR, LS, LT, LU, LY, MA, MD, ME, MG, MK, MN, MW, MX, MY, MZ, NA, NG, NI, NO, NZ, OM, PE, PG, PH, PL, PT, RO, RS, RU, SC, SD, SE, SG, SK, SL, SM, ST, SV, SY, TH, TJ, TM, TN, TR, TT, TZ, UA, UG, US, UZ, VC, VN, ZA, ZM, ZW.

(84) **Designated States** *(unless otherwise indicated, for every kind of regional protection available)*: ARIPO (BW, GH,

[Continued on next page]

(54) **Title**: SEMICONDUCTOR WIRE ARRAY STRUCTURES, AND SOLAR CELLS AND PHOTODETECTORS BASED ON SUCH STRUCTURES

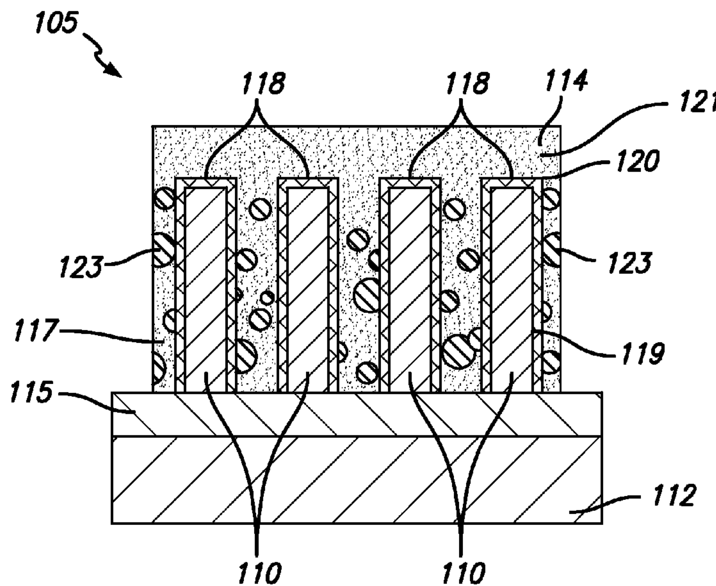

FIG. 5

(57) **Abstract**: A structure comprising an array of semiconductor structures, an infill material between the semiconductor materials, and one or more light-trapping elements is described. Photoconverters and photoelectrochemical devices based on such structure also described.

WO 2011/066570 A2

GM, KE, LR, LS, MW, MZ, NA, SD, SL, SZ, TZ, UG, ZM, ZW), Eurasian (AM, AZ, BY, KG, KZ, MD, RU, TJ, TM), European (AL, AT, BE, BG, CH, CY, CZ, DE, DK, EE, ES, FI, FR, GB, GR, HR, HU, IE, IS, IT, LT, LU, LV, MC, MK, MT, NL, NO, PL, PT, RO, RS, SE, SI, SK, SM, TR), OAPI (BF, BJ, CF, CG, CI, CM, GA, GN, GQ, GW, ML, MR, NE, SN, TD, TG).

Published:

— *without international search report and to be republished upon receipt of that report (Rule 48.2(g))*

SEMICONDUCTOR WIRE ARRAY STRUCTURES, AND SOLAR CELLS AND PHOTODETECTORS BASED ON SUCH STRUCTURES

CROSS REFERENCE TO RELATED APPLICATIONS

[0001] The present application claims priority to US provisional application 61/265,306 for "Light-trapping Si wire-array structure for solar cells and photodetectors" filed on November 30, 2009, US provisional application 61/265,297 for "Selective p-n junction fabrication technique for high-aspect-ratio semiconductor microstructures" filed on November 30, 2009, and US provisional application 61/313,654 for "Processing Steps for the Fabrication of a Microwire Array Solar Cell" filed on March 12, 2010, all three of which are herein incorporated by reference in their entirety. The present application is also related to US Patent Application S/N ______________ for "Three-dimensional patterning methods and related devices" filed on even date herewith, Attorney Docket Number P707-US, also incorporated herein by reference in its entirety.

FIELD

[0002] The present disclosure relates to semiconductor microstructures, such as high-aspect-ratio of semiconductor microstructures. More in particular, the present disclosure relates to semiconductor wire array structures, such as silicon (Si) wire arrays structures, especially for solar cells and photodetectors.

STATEMENT OF GOVERNMENT GRANT

[0003]

The present application was supported in part by the Department of Energy under grant DE-SC0001293 and grant DE-FG02-07ER46405. The US government may have certain rights in the invention.

BACKGROUND

[0004] Solar cells based on arrays of Si micro- or nanowires have been proposed as a potentially low-cost alternative to conventional wafer-based Si solar cells. See reference [1], incorporated herein by reference in its entirety.

[0005] Device physics modeling, based on experimentally measured properties of Si wires, has predicted that wires of micron-scale diameter will achieve the greatest photovoltaic energy conversion efficiency. See reference [2], incorporated herein by reference in its entirety.

Such solar-cell structure should effectively absorb all above-bandgap incident sunlight, over a broad range of incidence angle.

SUMMARY

[0006] According to a first aspect of the disclosure, a structure is provided, comprising: an array of elongated semiconductor elements; an infill material located in a space between the elongated semiconductor elements; and a reflective material, configured to reflect incident light and direct the incident light to the elongated semiconductor elements.

[0007] According to a second aspect of the disclosure, a structure is provided, comprising: an array of elongated semiconductor elements; an infill material located between the elongated semiconductor elements; and an antireflective coating at least partially and superficially covering a respective elongated semiconductor element, the antireflective layer being interposed between the infill material and the respective elongated semiconductor element.

[0008] According to a third aspect of the disclosure, a structure is provided, comprising: an array of elongated semiconductor elements; an infill material located in a space among the elongated semiconductor elements; and a light scattering material included in the infill material and surrounding the elongated semiconductor elements.

[0009] According to a fourth aspect of the disclosure, a structure is provided, comprising: an array of substantially vertically oriented elongated semiconductor elements; an infill material located in a space among the elongated semiconductor elements; and a material applied at least partially on a surface of the infill material, said material being selected from the group consisting of: light scattering material, concentrating material, and a texture.

[0010] According to further aspects of the disclosure, solar cells, photoconverter devices and photoelectrochemical devices comprising the above structures are also provided.

[0011] Further aspects of the disclosure are shown in the specification, drawings and claims of the present application.

[0012] Appendix 1, Appendix 2, and Appendix 3 are filed together with the present application and form integral part of the specification of the present application.

BRIEF DESCRIPTION OF THE DRAWINGS

[0013]

FIGURE 1 shows a schematic partial cross sectional view of a baseline structure including a wire array.

FIGURE 2 shows a schematic partial cross sectional view of a structure according to an embodiment of the present disclosure.

FIGURE 3 shows a schematic partial cross sectional view of a structure according to another embodiment of the present disclosure.

FIGURE 4 shows a schematic partial cross sectional view of a structure according to a further embodiment of the present disclosure.

FIGURE 5 shows a schematic partial cross sectional view of a structure according to a further embodiment of the present disclosure.

FIGURE 5 shows a schematic partial cross sectional view of a structure according to yet another embodiment of the present disclosure.

FIGURE 6 shows a schematic partial cross sectional view of a structure according to still another embodiment of the present disclosure.

FIGURE 7 shows a schematic partial cross sectional view of a structure according to a further embodiment of the present disclosure.

FIGURE 8 shows a schematic partial cross sectional view of a structure according to a further embodiment of the present disclosure.

FIGURE 9 shows a schematic partial cross sectional view of a structure according to a further embodiment of the present disclosure.

FIGURE 10 shows a schematic partial cross sectional view of a structure according to another embodiment of the present disclosure.

FIGURE 11 shows a schematic partial cross sectional view of a structure according to yet another embodiment of the present disclosure.

FIGURE 12 shows a schematic partial cross sectional view of a structure according to still another embodiment of the present disclosure.

FIGURE 13 shows a perspective view of a solar cell according to a further embodiment of the present disclosure.

FIGURE 14 shows a schematic partial cross sectional view of a solar cell according to a further embodiment of the present disclosure.

FIGURE 15 shows a schematic partial cross sectional view of a photoelectrochemical device in accordance with the present disclosure.

FIGURE 16 shows a schematic partial cross sectional view of a structure according to a further embodiment of the present disclosure.

FIGURE 17 shows a schematic partial cross sectional view of a structure according to a further embodiment of the present disclosure.

FIGURE 18 shows a schematic partial cross sectional view of a structure according to a further embodiment of the present disclosure.

FIGURE 19 shows a schematic partial cross sectional view of a structure according to a further embodiment of the present disclosure.

FIGURE 20 shows a schematic partial cross sectional view of a structure according to a further embodiment of the present disclosure.

FIGURE 21 shows a schematic partial cross sectional view of a structure according to a further embodiment of the present disclosure.

FIGURE 22 shows a schematic partial cross sectional view of a structure according to a further embodiment of the present disclosure.

DETAILED DESCRIPTION

[0014] With reference to FIGURES 1-22, the present disclosure describes structures, solar cells, photoconverts and/or photoelectrochemical devices comprising an array of semiconductor

structures, an infill material between the semiconductor materials, and one or more of the following light-trapping elements: textured surfaces, light-concentrators, light-scatterers, antireflective layers, or reflective layers; or combinations of such elements. These light trapping elements can be opportunely located in the structures to direct incident light to the semiconductor materials. These light trapping elements can furthermore provide, in accordance with some embodiments, one or more of the following synergistic functionalities to photoconverters based on these structures: passivation of the semiconductor surfaces, conduction of electrical current, or structural support.

[0015] FIGURE 1 shows a schematic partial cross sectional view of a baseline structure (101) including an array of elongated semiconductor elements (110), such as Si wires. In general, FIGURES 1-12 and 16-22 show schematic partial cross sectional views of structures (102), (103), (104), (105), (106), (107), (108), (109), (1001), (1002), (1003) and further structures (1004) (1005), (1006), (1007), (1008), (1009) and (1010), according to respective embodiments of the present disclosure. All of the structures (102), (103), (104), (105), (106), (107), (108) (109), (1001), (1002), (1003), (1004), (1005), (1006), (1007), (1008), (1009) and (1010) can include the baseline structure (101) of FIGURE 1.

[0016] The baseline structure (101) comprises an array of wires (110), such as elongated semiconductor elements, which, by way of example and not of limitation, is a square-tiled array of 67-μm-long Si wires (110) having an areal packing fraction of $\eta f = 4.2\%$. In such specific embodiment, the structure (101) contains the same volume of Si as a 2.8 μm-thick planar sheet of Si. Such array (101) shows peak absorption at normal incidence (< 0.5), and increased absorption at steeper angles of incidence. The wires can have any kind of shape, such as a cylindrical shape and have the same shape. In other embodiments of the disclosure, the wires are cones, pyramids, wires or whiskers. Moreover, the semiconductor wires (110) can be tiled according to an ordered lattice pattern within the array. Moreover, in some embodiments, the semiconductor elongated elements can be coated with additional materials for reasons other than the improvement of optical absorption.

[0017] The Si wires (110) extend from a substrate (112), for example a quartz slide, which is a well-suited substrate for optical transmission and reflection measurements. The Si wires (110) are embedded in a transparent casing, infill material or environment (114). The infill material (114) is generally transparent and has an index of refraction that is greater than 1.0 and less than that of the semiconductor material, including such materials such as a polymer casing, in particular polydimethlysiloxane (PDMS), air, EVA (ethylene vinyl acetate), liquids, oxides, mylar, or wax. In particular, the infill material (114) is located in a space between the elongated semiconductor elements or Si wires (110). The infill material (114) is able to effectively reduce the reflectivity of the semiconductor wires.

[0018] According to several embodiments, the structure (101) has non-subwavelength dimensions. The expression "subwavelength" is intended to mean that the wires or wire-like or elongated semiconductor elements (shaped e.g. as cylinders, cones, pyramids, elongated solids, tree-shaped elements etc.) have average minimum dimension (e.g. radius, width, etc.) that is less than the free space wavelength of sunlight, for wavelengths of sunlight having photon energy in excess of the semiconductor bandgap. In some embodiments, the elongated semiconductor elements have diameters of at least 1 microns, lengths of at least 20 microns or more and length to diameter rations of at least 5. For silicon, the structure (101) has an average minimum dimension less than about 1100 nm (1.1 microns). According to further embodiments, the structure (101) includes non-Si elongated semiconductor elements, such as, for example Ge, GaP, GaAs, InP, InGaAs, SiC.

[0019] In some embodiments, the structure (101) has a packing fraction lower than 10%. In other words, in some embodiments, the volume occupied by the semiconductor material or wires forms less than 10% of the volume of the structure. In fact, the expression "packing fraction" or "aerial packing fraction" is defined as the relative percentage (by volume) of semiconductor material within the array structure. The structure is intended as including the semiconductor wires and other materials (voids, casing, particles, coatings, etc.) lying between the horizontal planes that confine the upper and lower extent of the wires and their coatings. As an example, an array of vertical cylindrical semiconductor wires tiled in a square lattice can be considered, in which each wire has height h and radius r and is spaced a distance l from adjacent wires. With

reference to this example, the packing fraction is $\pi r^2 / l^2$. In some embodiments, a structure including the structure (101) is configured in such a manner that at least 80% of visible light incident on the structure from one or more angles of incidence is absorbed by the structure. More in particular, at least 50% of photons from the solar spectrum having energy greater than the semiconductor bandgap energy that are incident on the structure from one or more angles of incidence are absorbed within the semiconductor material. In some embodiments, the projected area of the semiconductor structures occupy less than 10% of the optical incidence plane.

[0020] FIGURE 2 shows a structure (102), which includes the structure (101) and further includes a back reflector (115), for example a metal layer, such as a mirror-like Ag back-reflector, interposed between the Si wires (110) and the substrate (112). According to further embodiments, other metallic or dielectric back-reflectors, having specular or non-specular (e.g. Lambertian) reflectance, can be used instead of a mirror-like Ag back-reflector. The back reflector can be made, for example, of metals like Al, Ag, Au, Cu, Ni, Ti, or In. In other embodiments, the back reflector (115) acts as substrate and entirely replaces the substrate (112), as shown in FIGURE 17.

[0021] The back reflector (115) increases an optical path length within the array (102). In particular, the presence of the back reflector (115) increases the optical path length for absorption within the wire array (102) (approaching peak normal-incidence values of 0.8). In this embodiment, the normal-incidence absorption can remain weaker than that at off-normal-incidence angles because there is no randomization of light within the array. At normal incidence, light travels parallel to the wires, hits the back reflector, and then travels vertically upward again to escape the array structure without striking the wires.

[0022] According to further embodiments, the back reflector can be positioned only under the Si wires (110), or only under the infill material (114), or under both the Si wires (110) and the infill material (114). It follows that the back-reflector extend either partially over the entire substrate (112), as shown for example in the structure 1004 of FIGURE 16 (where the back reflector is

beneath the infill only) or beneath the entire structure as shown in the structure 1005 of FIGURE 17.

[0023] According to further embodiments, light-scattering material or surface texture (115a) is applied on the back reflector (115). Such light-scattering material (115a) is able to change the direction of incident light upon reflecting from the back reflector in a manner so as to increase the optical path length within the structure, particularly from incidence at angles normal to the reflector. In one embodiment, the structure 1006, shown in FIGURE 18, includes the back-reflector features random texture so as to produce Lambertian reflectivity. Such light-scattering causes light to strike the wires (110) that might otherwise have traveled between the wires without being absorbed. In one embodiment, such light-scattering is achieved through random surface texturing applied to the top surface of the infill material, as shown in the structure (1008) of FIGURE 20, whereas in another embodiment such light-scattering is achieved through a curvature of the infill top surface near the wires due to surface tension, volumetric expansion or contraction, or other means, as shown in the structure (1009) of FIGURE 22.

[0024] FIGURE 3 shows a portion of a structure (103), which is similar to the structure (102) of FIGURE 2, and further includes a light-concentrating texture (116) located on the upper surface of the infill material (114) and facing the incident light (L). Such light-concentrating material (116) serves to change the direction of incident light upon transmission into the infill material or wires in a matter that increases the average optical path length within the structure. According to further embodiments, light-concentrating material or surface texture (116) is applied on the back reflector (115). Such light-concentrating material acts as a focusing reflector that focuses the light towards the Si wires (110) and improves light absorption. In one embodiment such light-concentrating texture (116) is approximated by parabolic dish reflectors beneath each wire (110), as shown in the structure (1007) of FIGURE 19.

[0025] FIGURE 21 shows a portion of a structure (1010), which is similar to the structure (102) of FIGURE 2, and further includes a light-concentrating texture (116) located on the upper surface of the infill material (114) and facing the incident light (L). Such light-concentrating material (116) serves to focus the light (L) towards the Si wires (110) and improves light

absorption, while decreasing the light acceptance angle of the structure. The structure (1010) differs from the structure (103) of FIGURE 3 for the absence of any substrate physically distinct from the back reflector. In FIGURE 21 the back reflector (115) acts as substrate.

[0026] FIGURE 4 shows a structure (104), which includes the structure (101) of FIGURE 1, and further includes an antireflective coating (118) deposited on each Si wire (110). In the depicted embodiment, the antireflective coating consists of amorphous silicon nitride (a-SiN_x), which also serves as a surface passivation layer on the Si surfaces. According to further embodiments, other materials can be used instead of a silicon nitride antireflective layer, which may or may not also serve as surface passivation. Such surface passivation and/or antireflective coating (118) is deposited on the top (120) and side (119) walls of the Si wires (110). According to further embodiments, the antireflective coating (118) partially covers the surfaces of the Si wires. In the embodiment of FIGURE 4 the surface passivation antireflective coating (118) is, for example, a-SiN_x AR-coating (e.g., 80 nm nominal thickness) and is deposited on the Si wires (110) prior to embedding the Si wires (110) in the infill or casing (114). According to further embodiments the antireflective coating (118) can include one or more of nitrogen, oxygen, hydrogen, and/or silicon.

[0027] According to further embodiments, the antireflective layer (118) varies in thickness along a surface of the elongated semiconductor elements, for example, to minimize reflection of certain wavelengths of light at various positions along the elongated semiconductor elements. For a simple quarter-wave antireflective coatings, the ideal layer thickness depends directly on the wavelength of light, which for solar applications, can span from 280–4000 nm, as well as the refractive index of the antireflective material. By varying the antireflective layer thickness along the surface of the elongated semiconductor structure, optimal antireflection for one particular wavelength can be achieved at one location along the structure, whereas optimal antireflection for a different wavelength can be achieved elsewhere along the structure. According to a further embodiment, the antireflective layer (118) varies in composition along a surface of the elongated semiconductor elements. In one embodiment, the antireflective layer consists of a transparent conductive oxide such as indium tin oxide at the tops of the elongated semiconductor elements, and a transparent dielectric such as silicon nitride along the sides of the elongated semiconductor

elements. This configuration is beneficial for solar cells comprising arrays of elongated semiconductor structures, wherein the conductive top-layer antireflective material also serves as a device electrode, and wherein the dielectric sidewall antireflective material also serves as a surface passivation layer. In further embodiments, light scattering materials are further applied on the antireflective layer (118). In some embodiments, the antireflective coating is produced by plasma-enhanced chemical vapor deposition.

[0028] The structure (104) of FIGURE 4 also includes light scattering particles (123), for example Al_2O_3 particles (e.g., 0.9 μm nominal diameter). Such particles are added to the infill material (114) and laterally surround the Si wires (110), to scatter the light that might otherwise pass between the Si wires (110). In particular, in some embodiments, the light scattering particles (123) uniformly surround all of the sides (119) of the Si wires (110). According to further embodiments, instead of the light scattering particles (123), the structure includes light-scattering elements selected from the group including void, bubble, dielectric composition, metal particle, and a polymer. In particular, the dielectric composition comprises one element selected from the group including Al_2O_3, $BaSO_4$, TiO_2, SiO_2 and the metal particle comprises one element selected from the group including Ag, Au, Ni, Al and Cu.

[0029] In FIGURE 5, the infill material (114) includes an infill bottom zone (117) and a different infill top zone (121). Concentration of the light scattering elements (123) is greater in the infill bottom zone (117) than in the infill top zone (121). In other words, the light scattering elements (123) are concentrated near the bottom of the wire array in a zone opposite to the incident light, or near the substrate, and more diffused or less concentrated in a zone faced to the incident light. In this way, light that is reflected or scattered upwards has more distance with which to interact with the wires, thus increasing the probability of absorption. Similar results can be obtained when density of the light scattering elements (123) is higher in the infill bottom zone (117) than in the infill top zone (121). These results can be obtained, for example, by centrifugation to force the particles to the bottom. In other embodiments, the light-scattering structure or material within the infill material is varied in density or composition with proximity to the semiconductor structures. In other words, concentration of the light scattering elements (123) is higher in proximity to the elongated semiconductor elements (110) than in a far zone thus further

increasing the probability of absorption into the elongated semiconductor elements (110). In some embodiments, the light-scattering material within the infill material (114) comprises the incorporation of a translucent material, such as wax or a white polymer to increase the scattering capacity of the light-scattering material. In other embodiments, light-scattering structure within the infill material comprises voids of the material or bubbles of air. Moreover, in some embodiments, in order to further increase the probability of absorption into the elongated semiconductor elements (110) the light-scattering material is applied to the surface of the semiconductor, infill, antireflective, or reflective materials.

[0030] With continued reference to FIGURE 4 and FIGURE 5, the structure (104) and the structure (105) can include a light-scattering material located on the upper surface of the infill material (114) and facing the incident light. Such light-scattering material scatters the light towards the Si wires (110) and improves light absorption, as already described above. According to further embodiments, a light-scattering material is placed on the surface of the infill material.

[0031] Such surface passivation antireflective coating (118) and light scattering particles (123) were chosen because they have negligible absorption across defined wavelengths of 500-1100 nm, and thus enable a direct observation of absorption enhancement within the Si wires (110) themselves. The surface passivation antireflective coating (118) and light scattering particles (123) virtually eliminate an angular sensitivity of the wire array's absorption, and increase the peak normal-incidence absorption to 0.92. This is desirable because maximal absorption is desired at normal incidence for most solar applications. If the absorption is significantly less at normal incidence than for other angles, then a solar cell will produce less electricity when the sun is directly overhead, when there is the greatest potential to produce solar energy.

[0032] FIGURE 5 shows a structure (105) which is similar to the structure (104) of FIGURE 4 and further includes the back reflector (115) such as the Ag back-reflector shown in FIGURE 2. It follows that the structure (105) of FIGURE 5 differs from the structure (104) of FIGURE 4 for the presence of the back reflector (115).

[0033] It is noted that such presence of the back reflector determines, in some embodiments, an array's peak absorption increasing to 0.96, which is nearly the maximal absorption achievable by any material fully embedded within an infill (114) such as PDMS due to the about 3% reflectivity of the PDMS-air dielectric interface.

[0034] FIGURE 6 shows a structure (106), which includes the structure (101) of FIGURE 1, and further includes the previously described surface passivation antireflective coating (118), placed on each Si wire (110). The surface passivation antireflective coating (118) is deposited onto the top (120) and side (119) walls of the Si wires (110).

[0035] FIGURE 7 shows a structure (107), which includes the structure (101) of FIGURE 1, and further includes the previously described light scattering particles (123), for example Al_2O_3 particles (0.9 μm nominal diameter). Such particles are added to the infill and randomly surround the Si wires (110), to scatter the light that might otherwise pass between the Si wires (110). In particular, the light scattering particles (123) surround the Si wires (110) near the bottom.

[0036] FIGURE 8 shows a structure (108) which is similar to the structure (105) of FIGURE 5, with the difference that the coating (118) is located only on the top of the elongated elements or wires (110), facing the incident light (L). Moreover, the structure (108) includes elongated semiconductor elements (110), which are randomly located and randomly oriented. Moreover the elongated semiconductor elements (110) present angled or angular or sharp profile. Both these features increase, in combination with light scattering material or texture material or reflective material, the probability of light absorption.

[0037] FIGURE 9 shows a structure (109) according to a further embodiment of the present disclosure which includes an array of elongated semiconductor elements (110). The semiconductor elements (110) have top ends (120) and free bottom ends (130). The semiconductor elements (110) are embedded in the infill material (114) and the antireflective coating (118) is located on a free bottom end (130) of the elongated semiconductor elements (110). The structure (109) further includes a back reflector (115) which is shaped as a

concentrating lens (116). The concentrating lens (116) focuses some or all of the light (L) incident on the structure (109) onto the smaller area occupied by the semiconductor wires.

[0038] According to a further embodiment of the present disclosure, a structure comprises an array of elongated semiconductor wires, such as the structure (101) disclosed above, wherein the semiconductor wires are generally oriented vertically; and an optical concentrator element, such as, for example, the concentrating lens (116) mentioned above that focuses some or all of the light incident on the structure onto the smaller area occupied by the semiconductor wires. According to further embodiments, light concentrators are placed on the semiconductor wires. In some embodiments, the concentrating lens (116) can be included in any one of the embodiments of figures 2-8, 10-12 and 16-22.

[0039] The focusing lens (116) can focus the light to one or more of the semiconductor wires. According to a further embodiment, the concentrator element is below or adjacent to one or more of the semiconductor wires. According to further embodiments, the average cross-sectional area of the semiconductor wires within the array comprises less than 10% of the cross-sectional area of the optical incidence plane. In particular, the absorption of light (L) within the semiconductor material decreases to less than 50% of the value produced under normal-incidence illumination for illumination incidence angles exceeding 45° from normal.

[0040] The infill material can be textured to produce the focusing lens above one or more of the semiconductor wires. According to further embodiments, the focusing lens is coated with a reflective material to produce a focusing reflector below or adjacent to one or more of the semiconductor wires. The surface texturing can be produced by the contraction of the infill material, surface tension of the infill material, particles or voids within the infill material, imprint lithography, or casting. The semiconductor wires can be tiled according to an ordered lattice pattern within the array, and the ordered array of focusing lenses is positioned above the structure or an ordered array of focusing reflectors is positioned below the structure.

[0041] FIGURE 10 shows a structure (1001), which includes an array of semiconductor wires or cones generally vertically oriented, wherein the diameter of one or more wires or cones is flared

near either or both ends of the structure, to produce a feed horn structure including at least one elongated portion (110b) and one flared portion (110a), or a truncated cone portion. The flared portion (110a) faces the incident light (L). The average diameter of each wire or cone (110) is sufficiently large to support guided optical modes within the semiconductor material. Instead of the feed horn structure, the structure (1001) can include a plurality of truncated cone wires.

[0042] According to further embodiments, the flared portion (110a) can be opposite to the incident light (L). Additionally, the cross-sectional area of the larger end of the flared portion (110a) can be at least four times the average cross-sectional area of the elongated portion of the semiconductor wire. The taper in the diameter of the feed horn structure or of a truncated cone wire can provide total internal reflection of light incident into the wire at normal incidence.

[0043] The structure (1001) of FIGURE 10 includes an antireflective layer (118) placed on the top of the infill material (114). Other trapping light elements can be present, such as the focusing lens (116) and/or the light scattering particles (123) and/or the back reflector (115), as also those described in structures (102)-(109).

[0044] According to further embodiments, the feed horn structure, or each truncated cone wire, is produced by an increase or decrease in the diameter of a semiconductor wire or cone during its growth. The feed horn structure can be produced by etching a semiconductor wire or of a cone. The feed horn structure can produced at the bottom of a semiconductor wire or cone and then subsequently relocated to top of the structure by removing the wire or cone from the original support substrate and turning it upside-down.

[0045] FIGURE 11 shows a structure (1002) according to a further embodiment of the disclosure. In particular, the structure (1002) includes wires having frusto-conical shape or feed horn structure as in the embodiment of FIGURE 10, and a back reflector (115) placed under the wires (110). A larger flared portion (110a) of the frusto-conical wires (110) is located opposite to the incident light (L).

[0046] FIGURE 12 shows a structure (1003) according to a further embodiment of the present disclosure. In particular, the structure (1003) comprises an array of semiconductor wires (110), which are tilted to a non-vertical orientation so as to increase the projected cross-sectional area of the semiconductor wires within the optical incidence plane at normal-incidence illumination. In the embodiment of FIGURE 12, the wires (110) are generally oriented parallel to one another and share similar diameter and height.

[0047] According to further embodiments, the non-vertical orientation of the semiconductor wires is produced by growing the wires on a substrate in a manner that yields non-vertical growth, or by etching the wires from a substrate in a manner that yields non-vertical wires. According to alternative embodiments, the non-vertical orientation of the semiconductor wires is produced by growing or etching the wires in a manner that yields vertical or near vertical wires, then embedding the wires within an infill material and exerting a sheer force such that the wires remain tilted at a non-vertical angle within the plane of the structure.

[0048] The structure (1003) of FIGURE 12 includes the back reflector (115) placed under the infill material (114). Other trapping light elements can be present, such as the focusing lens (116) the light scattering particles (123), the antireflective coating (118), and/or those described in structures (102)-(109).

[0049] The structures (101), (102), (103), (104), (105), (106), (107), (108), (109), (1001), (1002), (1003), (1004), (1005), (1006), (1007), (1008), (1009) and (1010), or any combination of such structures, described above can be manufactured according to the technique described in reference [3], incorporated herein by reference in its entirety. Si wires (110) are grown on p type <111> Si wafers ($\rho < 0.001$ Ω•cm), using, for example, a 300 nm thermal oxide for catalyst confinement and evaporated Au, Cu, or Ni (400–700 nm thickness) as the VLS catalyst. No notable differences were observed between the optical properties of wires grown using Au, Cu, or Ni catalyst metal.

[0050] Following growth, the wire arrays were etched in 5% HF(aq) for 30 s. To remove the catalyst metal, Au-catalyzed wires were then etched for 30 min in a solution of 9:1 Gold Etchant

TFA (Transene) to 36% HCl(aq) and then rinsed for 30 s in 5% HCl(aq). Cu- and Ni-catalyzed wires were instead etched for 20 min at 70 °C in a 6:1:1 solution of H2O:H2O2:HCl. Both groups of wires were then HF-etched as described above, dried, and momentarily dipped in a 50% (wt) solution of KOH (aq) at 55 °C, to remove ~20 nm of Si, thus removing the metal-rich surface layer observed in similarly grown wires. For the structures including surface passivation antireflective coating (118), a SiN_x film of 80-nm nominal thickness was conformally deposited onto the wire arrays by plasma-enhanced CVD at 350°C. In some embodiments, the reflective material comprises the substrate on which the elongated semiconductor structures were grown, or the substrate from which the elongated semiconductor structures were etched.

[0051] The lengths, diameters, and areal fractions of each wire array can be determined by computer-processing of high-resolution SEM images, taken from a 200 x 200 μm area at the center of each array. Only near-perfect wire arrays, defined as those that had at most one defect within this area (e.g. non-vertical or spurious growth, or a wire missing from the pattern), were considered. Arrays were embedded in PDMS and peeled-off.

[0052] The PDMS can be, for example, drop-cast, spun at 3000 rpm, and then cured at 120 °C for ≥ 1 hr, resulting in a smooth film whose overall thickness ranged from 10 to 50 μm greater than the height of the wire array. Subsequently, the wire arrays are transferred on the quartz slides for optical measurements. The arrays themselves are flexible polymer films, and could be transferred to any substrate (e.g. a window) or left as a free-standing flexible film. They have properties similar to a window decal.

[0053] For the structures which incorporate light scattering particles, e.g. Al_2O_3 light-scatterers, particles of 0.9 μm nominal diameter, whose surfaces had been modified with trimethylchlorosilane, were dispersed into CH_2Cl_2 by sonication. This solution was mixed into the PDMS to yield a ratio of 1:10:10 Al_2O_3:CH_2Cl_2:PDMS by weight. The suspension was drop cast, spun, and cured as described above. Prior to curing, the arrays were centrifuged for several minutes to drive the Al_2O_3 particles towards the bottom of the PDMS layer. In particular, in some embodiments, light-scattering materials are placed between the semiconductor structures before the infill material is added to the structure. The light-scattering materials can be mixed

into the infill material before the infill is added to the structure. In some embodiments, the light-scattering property of the infill material is produced by a chemical process following the addition of the infill material to the structure. In some embodiments, the composition of the infill material is varied as it is added to the structure to produce an inhomogeneous distribution of light-scattering materials or structures within the structure. In some embodiments the distribution of light-scattering materials or structures is produced through evaporation or contraction of the infill material. For the structures including the back reflector, such back reflector is placed on the quartz slides using a thermal evaporator. Each array is placed on a clear quartz slide or a metal-coated one to compare their absorption with vs. without the back reflector. In an envisioned solar cell (Figure 8) the metal would be deposited directly onto the wire arrays rather than onto quartz slides. In that case, it would also serve as a back metal contact. For structure including light-scattering texture such texture is produced by the contraction of the infill material, surface tension of the infill material, particles or voids within the infill material, imprint lithography, or casting.

[0054] To provide a figure of merit for the absorption measurements, the overall fraction of above-bandgap photons that each wire array would absorb throughout a day of operation as a non-tracking solar cell, A_{avg}, was calculated based on a time-resolved reference spectrum of direct solar insolation, see reference [4], incorporated herein by reference in its entirety, in conjunction with the measured angle- and wavelength-dependent absorption values of the wire arrays of FIGURES 2-5. A_{avg} calculations that correspond to the absorption measurements are compared with the A_{avg} calculation that corresponds to the measured absorption of a commercial, 280-μm-thick polycrystalline Si solar cell with a dielectric AR-surface passivation antireflective coating. In a particular embodiment, the optimal Si wire array (105) of FIGURE 5 exhibited A_{avg} = 0.85, which although slightly below that of the commercial Si solar cell (A_{avg} = 0.87), is remarkable considering that this wire array film contained ~1% as much Si (per specimen area) as the commercial solar cell. This volume reduction implies substantial optical concentration within the Si wires.

[0055] To further gauge the absorption enhancement of the wire array geometry, the measured absorption, $A_{WA}(\theta_x,\lambda)$, of the wire array (105) from FIGURE 5 was compared to the theoretical

absorption limits of a "equivalently thick" (2.8 μm) planar Si absorber. Based on bulk Si properties, see reference [5], incorporated herein by reference in its entirety, and neglecting interference effects, two theoretical absorption limits were calculated for the equivalently thick Si slab: *i)* A_{Si}, which results from the use of bare, non-textured Si surfaces (black); and *ii)* A_{LT}, which results from ideal classical light-trapping at the Si surfaces. The latter case, the "Ergodic limit," is the maximally achievable absorption (in the ray-optic limit) of a planar-sheet absorber that utilizes ideally random (e.g. Lambertian) light trapping, see references [6], [7], incorporated herein by reference in their entirety.

[0056] The wire array's absorption exceeds the planar light-trapping limit for infrared wavelengths ($\lambda > 800$ nm). This behavior exemplifies a useful property of micro-structured, non-planar absorber geometries (including wire arrays), in that they can achieve greater absorption per material volume than achievable by a randomly textured, planar-sheet absorber geometry. This effect has been described, through use of a statistical ray optics model, for idealized films of polymer-embedded Si granules, see reference [7], and has also been simulated for Si wire arrays, see references [8] and [9], incorporated herein by reference in their entirety. The enhanced infrared absorption of the Si wire array yielded a greater overall absorption of above-bandgap photons than the equivalently thick, ideally light-trapping planar absorber. In fact, taking all measured incidence angles into account, the day-integrated absorption of the wire array ($A_{avg} = 0.85$) slightly exceeded that of the planar light-trapping case ($A_{avg} = 0.82$). Thus, the Si wire array geometry can enable solar cells that reach, and potentially even exceed, the theoretical absorption limit, per volume of Si, of ideal light-trapping within a conventional planar geometry.

[0057] The enhanced absorption properties of Si wire arrays enable high quantum efficiencies for photovoltaic applications. To demonstrate this, a photoelectrochemical cell was used to measure the external quantum efficiency (EQE) of Si wire-array photoelectrodes, which consisted of p-type wire arrays grown on degenerately doped (and thus photovoltaically inactive) Si wafers. The transparent electrolyte formed a rectifying junction to the top and sides of each wire (analogous to a radial p-n junction), enabling photoelectrochemical characterization of the angle- and wavelength-dependent EQE of the wire-array electrode. However, because the wires

were immersed in an electrolyte and attached to their growth substrate, this technique did not permit the use of a polymer infill, a dielectric antireflective coating and/or a planar metal back-reflector. Thus, relatively long (130 μm) and sparse (η_f = 6.2%) square-tiled wire arrays were grown, to minimize the transmission of light into the photovoltaically inactive growth substrate while also minimizing the area of the reflective top surface of the Si wires. This geometry yielded up to 0.85 peak EQE, but suffered from substantially reduced EQE at normal incidence. Evaluating the EQE across the day-integrated solar spectrum (as carried out for A_{avg} above) yielded EQE_{avg} = 0.56. When Al_2O_3 light-scattering particles were drop-cast into this wire array, the normal-incidence `dead spot' was virtually eliminated, the peak EQE increased to 0.89 and the day-integrated EQE_{avg} increased to 0.68. This value is significant, considering that the photoelectrochemical cell configuration precluded the use of a metal back-reflector or an antireflective coating, both of which are known to substantially improve the optical absorption as described above, and both of which could be used within a solid-state, radial p-n junction wire-array solar cell. Thus, the results described here represent lower bounds, rather than upper limits, on the EQE that could be achieved by use of the Si wire-array geometry making use of the light-trapping elements disclosed herein. The configuration of the electrode described in this paragraph is depicted in FIGURE 15.

[0058] FIGURES 13 and 14 of the present application describe embodiments relating to the applications, for example, of the structures (101), (102), (103), (104), (105), (106), (107), (108), (109), (1001), (1002), (1003), (1004), (1005), (1006), (1007), (1008), (1009) and (1010) or any combination of such structures, to semiconductor wire-array photovoltaics and photoconverters, i.e. devices that convert light into electricity, including solar cells, photoelectrochemical cells, photodiodes, phototransistors, and other photosensitive wire-array electronic devices. Such semiconductor wire-array photovoltaics and photoconverters can indifferently be based on any one of the structures (102), (103), (104, (105), (106), (108), (109), (1001), (1002), (1003), (1004), (1005), (1006), (1007), (1008), (1009) and (1010) or any combination of such structures.

[0059] In particular, FIGURE 13 shows an embodiment where the teachings of the present disclosure are combined with the teachings of US Patent Application S/N ______________. In fact, as already mentioned in the introductory paragraph of the present application, the present

application is also related to US Patent Application S/N ______________ for "Three-dimensional patterning methods and related devices" filed on even date herewith, Attorney Docket Number P707-US, incorporated herein by reference in its entirety, and claiming priority to the same US provisional applications of the present application. Such US Patent Application S/N ______________ describes selective p-n junction fabrication for semiconductor microstructures, and related methods and devices.

[0060] In particular, shown in FIGURE 13 is a perspective view of a Si wire array solar cell (600) with a transparent top contact (610) (e.g. an indium tin oxide (ITO) contact) and a metallic bottom contact (620) acting as a back reflector. Solar cell (600) is embedded into a polymer encasing or environment (630), e.g. a flexible transparent polymer such as PDMS. Light scattering particles (640) (e.g., Al_2O_3 particles as described before) are embedded inside the infill or environment (630), so as to surround and circle the Si wires (101). The solar cell (600) further comprises an array of mechanically flexible vertically aligned wires (650). The wires (650) are coated with a surface passivation antireflective coating (660). In particular FIGURE 13 corresponds to FIGURE 6 of the above mentioned US Patent Application S/N ______________.

[0061] The device of FIGURE 14 differs from the device of FIGURE 13 for the wires which remain on a rigid growth substrate (612) and for which the back reflector (620) is placed between the wires on top of said growth substrate rather than forming a continuous film beneath the infill and semiconductor structures. Furthermore, the bases or bottom of the semiconductor structures, shown in FIGURE 14, exhibit feedhorn-like structures as described above and therefore includes a flared portion (110a). Moreover, the device of FIGURE 14 includes light scattering material (640) having a light scattering material concentration higher in a bottom zone (630b) of the infill material than in a top zone (630a) of the infill material. In the present embodiment the back reflector (620) is the metal layer and the substrate (612) functions as the contact. Devices of the type depicted in FIGURE 14 were fabricated according to the teachings of US Patent Application S/N ______________, incorporated herein by reference in its entirety. Three different types of Si microwire solar cells were fabricated. The "As-Grown" cell contained no light trapping elements or antireflective coating on the semiconductor surfaces. The "Scatterer" cell incorporated light-scattering Al_2O_3 particles (nominally 80 nm in diameter) in-between the wires.

The "PRS" cell utilized an a-SiN_x:H passivation layer to minimize surface recombination and to serve as an anti-reflection coating, a Ag back reflector to prevent the loss of incident illumination into the growth substrate, and Al_2O_3 particles to scatter light incident between the Si microwires. Following the inclusion of the selected light-trapping elements, each wire array was filled to the tips of the wires with mounting wax (a transparent, non-conducting, thermoplastic polymer). Indium tin oxide (ITO) (120–150 nm thick) was then sputtered through a shadow mask to form a top-contact pad and to define individual cells. For both the Scatterer and PRS solar cells, the 80 nm Al_2O_3 particles were observed to form micron-sized agglomerates that were located near the base of the wires, permitting the infill region to be conceptually divided into an upper and lower region, for which the density of Al_2O_3 particles was significantly lower within the lower infill region. In the PRS solar cells, the 1000 nm thick Ag back reflector covered the growth substrate and the tapered base of the wires.

[0062] Under simulated AM 1.5G illumination, the champion PRS solar cell exhibited markedly higher photovoltaic performance than the champion Scatterer and As-Grown solar cells, as a result of a significant increase in short-circuit current density (J_{SC}) brought about by the combination of light-trapping elements exemplifying embodiments of the present disclosure. The champion PRS solar cell produced an open-circuit voltage (V_{OC}) of 498 mV, J_{SC} of 24.3 mA/cm^2, and a fill factor (FF) of 65.4%, for an efficiency of 7.92%. The champion Scatterer and As-Grown solar cells exhibited efficiencies of 5.64% and 3.81%, respectively, with similar V_{OC} and FF but lower J_{SC}: 16.6 mA/cm^2 and 11.8 mA/cm^2, respectively. The improved efficiencies of the Scatter and PRS cells over the As-Grown cells exemplify the benefits to photovoltaic performance afforded by the light-trapping structures of the present disclosure.

[0063] A device, such as the one of FIGURE 13 or FIGURE 14, includes one or more conductive layers, wherein at least some portion of each conductive layer is in contact with one or more of the semiconductor structures or wires (650), whose conductivity provides a path for current collection from the photovoltaic device. The device further includes one or more of the following features: a reflective structure, such as the back reflector (115, 620), an antireflective structure, such as the coating (118, 660), a light-scattering structure, such as the light scattering particles (123, 640), or a light-concentrating structure, such material (116). Additional reflective,

antireflective, light-scattering, or light-concentrating structures are applied above or below the conductive layers.

[0064] Moreover, according to further embodiments, in such device (600) at least 80% of the carriers excited by the absorption of light within the semiconductor material are collected as current from the photovoltaic device. Additionally, conductive layers can be located above and below the array of elongated semiconductor structures. Moreover, the semiconductor material occupies less than 10% of the volume of the structure enclosed between the two conductive layers.

[0065] According to further embodiments, the conductive layer comprises one or more of Ag, In, Al. Each conductive layer can be either at least 90% transparent or at least 90% reflective at a visible wavelength of light. According to further embodiments, some or all of the infill material comprises a conductive layer for the photovoltaic device. According to further embodiments, the antireflective coating or infill material serves to passivate some or all of the surfaces of the semiconductor structures. Some or all of the surfaces of the semiconductor structures are coated by one or more additional layers to provide passivation of the semiconductor surfaces or to increase the conductivity of the photovoltaic device. Moreover, the reflective material may also serve as a conductive layer.

[0066] According to a further embodiment, the present disclosure includes a photoelectrochemical device comprising, for example, any one of the structures (101), (102), (103), (104), (105), (106), (107), (108), (109), (1001), (1002), (1003), (1004), (1005), (1006), (1007), (1008), (1009) and (1010) or any combination of such structures. In particular, as mentioned above, FIGURE 15 shows a device (700) including an array of wires (110) and a liquid electrolyte solution (1114). The liquid electrolyte solution (114) can include any one of the liquid substances used as infill material, for example, in the structures (101), (102), (103), (104), (105), (106), (107), (108), (109), (1001), (1002), (1003), (1004), (1005), (1006), (1007), (1008), (1009) and (1010) disclosed in the previous paragraphs.

[0067] The examples set forth above are provided to give those of ordinary skill in the art a complete disclosure and description of how to make and use the embodiments of the disclosure, and are not intended to limit the scope of what the inventors regard as their disclosure. Modifications of the above-described modes for carrying out the disclosure may be used by persons of skill in the art, and are intended to be within the scope of the following claims. All patents and publications mentioned in the specification may be indicative of the levels of skill of those skilled in the art to which the disclosure pertains. All references cited in this disclosure are incorporated by reference to the same extent as if each reference had been incorporated by reference in its entirety individually.

[0068] It is to be understood that the disclosure is not limited to particular methods or systems, which can, of course, vary. It is also to be understood that the terminology used herein is for the purpose of describing particular embodiments only, and is not intended to be limiting. As used in this specification and the appended claims, the singular forms "a," "an," and "the" include plural referents unless the content clearly dictates otherwise. The term “plurality” includes two or more referents unless the content clearly dictates otherwise. Unless defined otherwise, all technical and scientific terms used herein have the same meaning as commonly understood by one of ordinary skill in the art to which the disclosure pertains.

[0069] A number of embodiments of the disclosure have been described. Nevertheless, it will be understood that various modifications may be made without departing from the spirit and scope of the present disclosure. Accordingly, other embodiments are within the scope of the following claims.

LIST OF CITED REFERENCES

[1] Kayes, B. M., Atwater, H. A. & Lewis, N. S. Comparison of the device physics principles of planar and radial p-n junction nanorod solar cells. J. Appl. Phys. 97, 114302-114311 (2005)

[2] Kelzenberg, M. D. et al. Predicted efficiency of Si wire array solar cells. 34th IEEE Photovoltaic Specialists Conference 1-6 (2009).

[3] Kayes, B. M. et al. Growth of vertically aligned Si wire arrays over large areas (> 1 cm2) with Au and Cu catalysts. Appl. Phys. Lett. 91, 103110-103113 (2007).

[4] Marion, B. et al. Validation of a photovoltaic module energy ratings procedure at NREL. Report No. NREL/TP-520-26909, (1999).

[5] Aspnes, D. E. in Properties of crystalline silicon (ed Robert Hull) 677 (INSPEC, IEE, 1999).

[6] Tiedje, T., Yablonovitch, E., Cody, G. D. & Brooks, B. G. Limiting efficiency of silicon solar-cells. IEEE Trans. Electron Devices 31, 711-716 (1984).

[7] Yablonovitch, E. Statistical ray optics. J. Opt. Soc. Am. 72, 899-907 (1982).

[8] Kelzenberg, M. D., Putnam, M. C., Turner-Evans, D. B., Lewis, N. S. & Atwater, H. A. Predicted efficiency of Si wire array solar cells. 34th IEEE Photovoltaic Specialists Conference 1-6 (2009).

[9] Altermatt, P. P., Yang, Y., Langer, T., Schenk, A. & Brendel, R. Simulation of Optical Properties of Si Wire Cells. Photovoltaic Specialists Conference, 2009. PVSC '09. 34th IEEE 1-6.

APPENDIX 1

Si microwire-array solar cells

Si microwire-array solar cells with Air Mass 1.5 Global conversion efficiencies of up to 7.9% have been fabricated using an active volume of Si equivalent to a 4 μm thick Si wafer. These solar cells exhibited open-circuit voltages of 500 mV, short-circuit current densities (J_{sc}) of up to 24 mA cm^{-2}, and fill factors >65% and employed Al_2O_3 dielectric particles that scattered light incident in the space between the wires, a Ag back reflector that prevented the escape of incident illumination from the back surface of the solar cell, and an a-SiN_x:H passivation/anti-reflection layer. Wire-array solar cells without some or all of these design features were also fabricated to demonstrate the importance of the light-trapping elements in achieving a high J_{sc}. Scanning photocurrent microscopy images of the microwire-array solar cells revealed that the higher J_{sc} of the most advanced cell design resulted from an increased absorption of light incident in the space between the wires. Spectral response measurements further revealed that solar cells with light-trapping elements exhibited improved red and infrared response, as compared to solar cells without light-trapping elements.

Vertically aligned arrays of crystalline-Si (c-Si) microwires may enable the fabrication of flexible c-Si solar cells with near unity internal quantum yield that are capable of absorbing >85% of the day-integrated (above band gap) direct solar illumination using a volume of Si equivalent to a 2.8 μm thick Si film.[1] Two advantages conferred by the three-dimensional geometry of vertically aligned, high-aspect ratio Si microwires are: (1) the ability to create high-quality single crystal Si structures with passivated surfaces *via* a vapor growth process;[2–4] and (2) enhanced absorption relative to planar c-Si absorbers.[1] These two advantages, in combination with the ability to grow arrays of Si microwires over large areas (>1 cm^2),[5] to peel the wire arrays from the growth substrate in a flexible polymer,[6] and to re-use the growth substrate,[7] offer the potential to fabricate flexible, high efficiency c-Si solar cells.[8,9]

Wire solar cells have been fabricated using c-Si,[10–20] amorphous-Si,[21] GaAs,[22] III-nitride,[23] and InP,[24] *via* a variety of growth techniques, including vapor-liquid-solid (VLS) growth,[10–16,19,20] metal-catalyzed chemical etching,[17,21] molecular beam epitaxy,[22] metal–organic chemical vapor deposition,[23,24] and deep reactive-ion-etching.[18] In particular, the VLS growth method offers a materials-efficient and scalable route for the synthesis of semiconducting wires. However, the efficiencies of VLS-grown, c-Si, single-wire[13,14,16] and wire-array[10–12,15,19,20] solar cells, up to 3.4%[13] and 1.8%[15] respectively, have fallen short of the ~15% photovoltaic efficiency predicted from simple considerations.[8,9] In particular these solar cells have failed to demonstrate open-circuit voltages (V_{oc}) in excess of 300 mV, possibly indicative of significant recombination within the depletion region and/or at the surfaces of the cells.[8,12,25] We report c-Si microwire-array solar cells that have exhibited 7.9% conversion of simulated Air Mass (AM) 1.5 Global (G) solar illumination to electrical energy with negligible photovoltaic response from the growth substrate.

Square-tiled arrays of vertically aligned Si microwires (2–3 μm in diameter on a 7 μm pitch) were grown on p^{++} (resistivity, ρ, <0.001 Ω cm) Si(111) wafers using the VLS growth method, as described previously.[5] P-type doping of the Si microwires was achieved during growth using BCl_3 as a gaseous dopant source.[4] Four-point electrical measurements performed on individual Si wires from arrays grown

Broader context

Driven by the restructuring of Germany's Renewable Energy Sources Act in 2000, the photovoltaics industry has grown tremendously, demonstrating an average compound annual growth rate of 56% in the five-year period prior to 2008. As a result of this growth and the subsequent development of the industry, the cost of photovoltaic electricity will likely reach grid-parity within the next 6–10 years (without significant technological advances.) However, for photovoltaics to generate an appreciable fraction of electricity, costs must be further reduced such that energy storage systems (batteries, hydrogen production coupled with fuel cells) can be implemented. Recently, Si microwire-array solar cells have emerged as a promising new type of low-cost solar cell with the potential for dramatically reduced Si consumption and flexible modules, while offering c-Si photovoltaic efficiencies. In this work we demonstrate the fabrication of Si microwire-array solar cells with high open-circuit voltages, short-circuit current densities and fill factors. These solar cells exhibit photovoltaic efficiencies of up to 7.9% and should achieve efficiencies of ~15% with known improvements in cell design.

under nominally identical conditions indicated that the wires were p-type with $\rho = 0.05\ \Omega$ cm, which corresponds to an electrically active dopant concentration (N_A) of 7×10^{17} cm^{-3}, assuming a bulk hole mobility of 1.8×10^2 cm^2 V^{-1} s^{-1} for Si.

Radial p–n junctions were fabricated within each wire, as illustrated in Fig. 1. First, the as-grown wire arrays (Fig. 1a) were chemically etched to remove the Cu-catalyst and to remove a thin layer (~50 nm) of surface Si, prior to the growth of a 200 nm thick thermal oxide (Fig. 1b). The thermal oxide was then selectively removed in a hydrofluoric acid (HF) solution (aq.), using polydimethylsiloxane (PDMS) as an etch barrier for the thermal oxide located at the bases of the microwires (Fig. 1c). After removal of the PDMS,[26] radial p–n junctions were formed in the upper region of the Si microwires during a phosphorus diffusion (junction depth of ~80 nm in a planar control), while the thermal oxide functioned as a phosphorus diffusion barrier for the lower region of the wires (Fig. 1d). We note that by appropriate choice of the PDMS layer thickness, the p–n junction could be defined to approximate either a radial or an axial p–n junction, or some combination of the two.

Three different types of Si microwire solar cells were fabricated. The As-Grown cell contained no light trapping elements or surface passivation. The Scatterer cell incorporated light-scattering Al_2O_3 particles (nominally 80 nm in diameter) in-between the wires. The *PRS* cell utilized an a-SiN_x:H passivation layer to minimize surface recombination and to serve as an anti-reflection coating, a Ag back reflector to prevent the loss of incident illumination into the growth substrate, and Al_2O_3 particles to scatter light incident between the Si microwires. Following the inclusion of the selected light-trapping elements (see ESI†), each wire array was filled to the tips of the wires with mounting wax (a transparent, non-conducting, thermoplastic polymer). Indium tin oxide (ITO) (120–150 nm thick, $\rho \approx 7 \times 10^{-4}\ \Omega$ cm) was then sputtered through a shadow mask to form a top-contact pad and to define individual cells.

Fig. 2 displays cross-sectional scanning electron microscope (SEM) images of a wire array after p–n junction formation and of a microwire solar cell for each cell type. As seen in Fig. 2a, the height of the thermal oxide (and thus the extent of the radial p–n junction) was uniform across the wire array. Wire heights ranged from 57–63 μm, 71–78 μm, and 43–49 μm for the As-Grown (Fig. 2b), Scatterer (Fig. 2c), and PRS (Fig. 2d) microwire solar cells, respectively. The thermal oxide covered the lower 27–32 μm of the wires in the As-Grown and Scatterer solar cells, but was removed prior to the desorption of the a-SiN_x:H layer in the PRS solar cells. For both the Scatterer and PRS solar cells, the 80 nm Al_2O_3 particles were observed to form micron-sized agglomerates that were located near the base of the wires, as evidenced by the granular texture of the mounting wax near the bottom of the wire array (Fig. 2c and d) and at the wire tips and sidewalls (Fig. 2c and d, inset). In the PRS solar cells, the 1000 nm thick Ag back reflector covered the growth substrate and the tapered base of the wires (Fig. 2d and S1†). The a-SiN_x:H anti-reflection/passivation layer in the PRS cell is not visible in Fig. 2d. However, the a-SiN_x:H layer conformally coated the wires and substrate prior to selective removal of the a-SiN_x:H from the tips of the wires, which allowed for the ITO to contact the n-Si emitter (Fig. S2†). For all devices, the mounting wax uniformly infilled the wire array, and the ITO conformally coated the mounting wax and the wire tips, thereby providing a continuous top contact despite the highly textured surface.

An important consideration for measurements of the photovoltaic performance of wire-array solar cells is the contribution from the growth substrate to the observed photocurrent. Though the fabrication of an appropriate control cell is not straightforward (even if the emitter doping compensated the substrate doping, the n^+ emitter and p^{++} substrate would form a tunnel junction) significant photocurrent from the substrate can be ruled out in our microwire-array solar cells. For the As-Grown and Scatterer solar cells, scanning photocurrent microscopy measurements indicated an effective minority-carrier diffusion length < 0.5 μm for electrons in the thermal-oxide-coated bases of the wires.[3] Consequently, neither the growth substrate nor the lower 27–32 μm of the wires contributed significantly to the observed photocurrent of the As-Grown and Scatterer solar cells. For the PRS microwire solar cells, the removal of the thermal oxide, followed by the deposition of the a-SiN_x:H passivation layer, produced an effective electron minority-carrier diffusion length ≫ 30 μm in the p-type bases of the wires.[3] Taken together, these results suggest that the bulk minority-carrier diffusion length is ≫ 30 μm throughout the wire but that the thermal-oxide-coated bases of the wires, for the Scatterer and As-Grown cells, exhibited very high surface recombination velocities, limiting the effective diffusion length in the oxide-coated wire bases to <0.5 μm. Hence, a photovoltaic response from the entire length of the wires was possible for the PRS solar cells. However, the photovoltaic contribution from the substrate for the PRS cells should be negligibly small, as the optically thick Ag back reflector coated the entire substrate except for where the wires had grown, ensuring that only the light guided through the Si microwires was able to reach the substrate. Consequently, 95% of the illumination ≤800 nm should have been absorbed over the 43–49 μm length of the wires, by a simple Beer–Lambert law analysis. The remaining illumination entered the p^{++} Si substrate (ρ < 0.001 Ω cm), which has been shown to exhibit an external quantum yield <0.05 for 800–1100 nm illumination.[1,2]

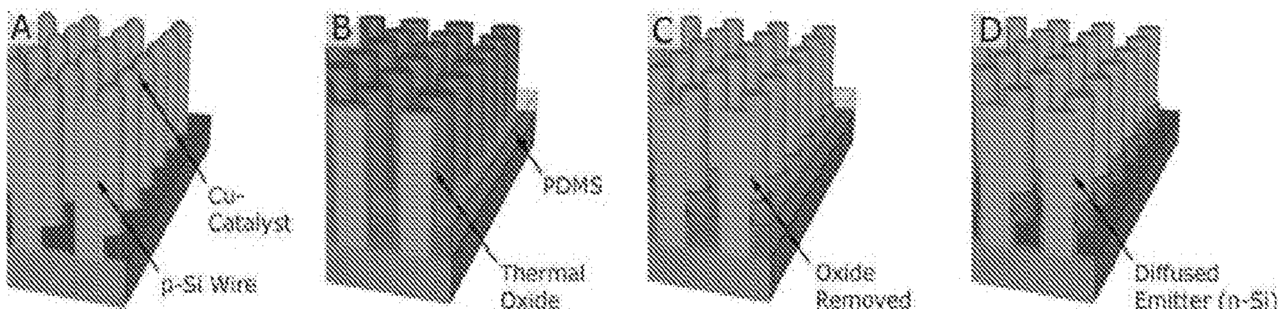

Fig. 1 Schematic of the radial p–n junction fabrication process. (a) VLS-grown, p-Si microwire array. (b) Microwire array after catalyst removal, growth of a thermal oxide and deposition of a PDMS layer. (c) Removal of the unprotected thermal oxide. (d) Removal of the PDMS and subsequent phosphorus diffusion to complete the fabrication of a radial p–n junction.

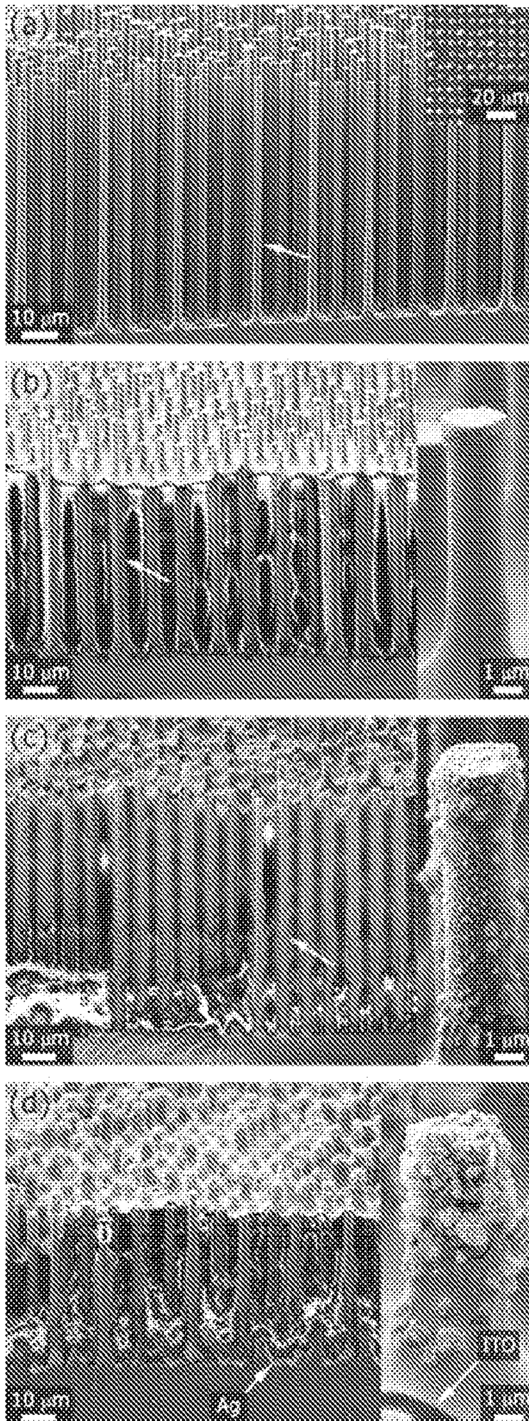

Fig. 2 Si microwire array solar cell device geometry. (a) Cross-sectional scanning electron microscope (SEM) image of a Si microwire array after radial p–n junction formation. The white arrow denotes the height of the thermal oxide (used as a phosphorus diffusion barrier in the radial p–n junction fabrication process). *Inset*: top-down SEM image of the same Si microwire array illustrating the pattern fidelity and slight variation in wire diameter. Cross-sectional SEM image of (b) an As-Grown solar cell, (c) a Scatterer solar cell, and (d) a PRS solar cell. *Insets*: higher magnification SEM images of the wire tips coated with ITO. For (b) and (c) the white arrow again denotes the height of the thermal oxide. For (d) the white arrow denotes the presence of the Ag back reflector. For the inset of (d) the white arrow denotes the ITO layer.

In total, 15 As-Grown microwire solar cells, 12 Scatterer microwire solar cells, and 24 PRS microwire solar cells were fabricated. The area of the fabricated cells spanned a range from 0.12 to 0.21 mm^2, as a result of variations in the gap between the top of the microwire arrays and the shadow mask during the deposition of the ITO. For each cell type, the majority of the cells were found to exhibit mutually similar V_{oc} and fill factor (FF) values (see Table S1†). To convert the measured short-circuit currents to short-circuit current densities (J_{sc}) and to calculate the photovoltaic efficiency (η), scanning photocurrent microscopy (SPCM) was used to image the perimeter of 2–3 cells from each cell type and thus accurately determine the photoactive cell area (see Fig. S3†).

Fig. 3 plots the measured current density as a function of voltage for the champion microwire solar cell of each cell type, in the dark (Fig. 3a) and under 100 mW cm^{-2} of simulated AM 1.5G illumination (Fig. 3b), respectively. In the dark, the microwire solar cells exhibited rectifying behavior with diode ideality factors between 1.7 and 2.2. The roll-off in the current density near 0.5 V in forward-bias resulted from the series resistance of the solar cells, which ranged from 300 to 3000 Ω and was dependent upon the quality of the contact between the electrical probe and the ITO.

Under simulated AM 1.5G illumination, the champion PRS solar cell exhibited markedly higher photovoltaic performance than the champion Scatterer and As-Grown solar cells, as a result of a significant increase in J_{sc} (Fig. 3b). Table 1 displays the values of V_{oc}, J_{sc}, FF, and η for all of the microwire solar cells whose cell areas were

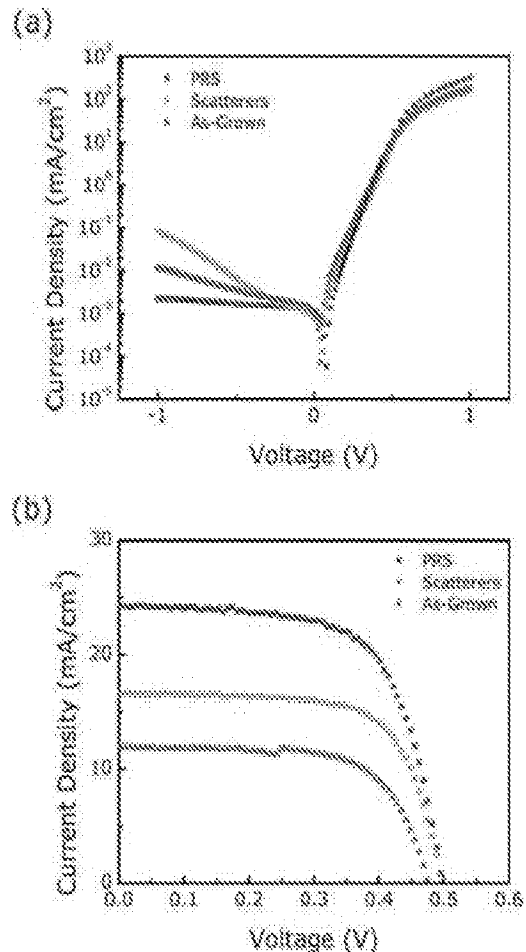

Fig. 3 Current density as a function of voltage for the champion microwire solar cell of each cell type (a) in the dark and (b) under simulated AM 1.5G illumination. The black line in (a) is an exponential fit to the dark J–V data of the PRS solar cell and was used to extract an ideality factor of 1.8.

measured by SPCM. V_{oc} of ~500 mV and FF > 65% were observed for all three cell types. The champion PRS solar cell produced a V_{oc} of 498 mV, J_{sc} of 24.3 mA cm^{-2}, and FF of 65.4%, for an $\eta = 7.92\%$. The champion Scatterer and As-Grown solar cells exhibited $\eta = 5.64\%$ and $\eta = 3.81\%$, respectively, with similar V_{oc} and FF but lower J_{sc}. For the PRS and Scatterer cells, the differences in η within a cell type largely resulted from differences in J_{sc}, which may have resulted from variations in the incorporation of the Al_2O_3 scattering particles or from variations in the fraction of electrically contacted wires (see Fig. 4b and c and S3†). We estimate the internal error in the measurement of the cell area to be 5% and the internal error in the AM 1.5G illumination intensity to be 5%, yielding a ~7% internal error in the measurement of J_{sc} and η.

To better understand the differences in J_{sc} between the PRS, Scatterer, and As-Grown solar cells, scanning photocurrent microscopy was used to map the photocurrent produced by the wire-array solar cells as a function of localized laser illumination (λ = 650 nm, ~1.0 μm beam waist), as seen in Fig. 4. To facilitate comparison between the different types of cells, each scanning photocurrent image was normalized to its maximum photocurrent. The measured photocurrent was maximized when the laser illumination was centered on a wire and was minimized when the illumination was centered between four adjacent wires. The photocurrent cross-sections shown below each scanning photocurrent image indicated that the relative magnitude of the decay in photocurrent as the laser moved from a peak (centered on a wire) to a valley (between two adjacent wires) clearly decreased from the As-Grown cell (Fig. 4a) to the Scatterer cell (Fig. 4b) and from the Scatterer cell to the PRS cell (Fig. 4c). In particular, the PRS solar cell exhibited nearly uniform photocurrent across the array, demonstrating that the Ag back reflector and Al_2O_3 dielectric scattering particles allowed for the effective collection of light incident between the wires.

The spots of greatly reduced photocurrent in the Scatterer and PRS solar cells arose from wires that were not electrically contacted by the ITO (wire vacancies would be expected to produce a photocurrent similar to the valley photocurrent, whereas, uncontacted wires parasitically absorb incident illumination). The small fraction of electrically inactive wires seen for the PRS and Scatterer cells likely results from the presence of Al_2O_3 scattering particles at the wire tips preventing the fabrication of a good electrical contact between the n^+-Si emitter and the ITO.

As seen in Fig. 5, the As-Grown and Scatterer solar cells exhibited similarly shaped spectral response curves (though different in absolute magnitude), both exhibiting a decline in the external quantum yield (EQY) at wavelengths >550 nm. By comparison, the PRS solar cell exhibited nearly constant EQY between 500 nm and 800 nm. The increased red and infrared response of the PRS cell presumably arose from light incident between the wires that was scattered multiple times from the Al_2O_3 scattering particles and the Ag back reflector. Integration of the observed EQY with the AM 1.5G solar spectrum predicted J_{sc} values of 13.3 mA cm^{-2}, 18.0 mA cm^{-2}, and 23.3 mA cm^{-2} for the As-Grown, Scatterer, and PRS solar cells, respectively, in good agreement with the measured J_{sc} values.

The three types of microwire solar cells were fabricated to facilitate a comparison between the cell types. However, three differences between the cells are worth noting. First, the wire length and thermal oxide heights translated to active wire lengths of 27–33 μm, 41–48 μm, and 43–49 μm for the As-Grown, Scatterer and PRS solar cells, respectively. Assuming no reflection losses and single-pass absorption, the theoretical increase in J_{sc} from a 30 μm thick Si wafer to a 45 μm thick Si wafer is 1.75 mA cm^{-2}, a 5.3% increase. Applying a 5.3% increase to the 11.8 mA cm^{-2} J_{sc} of the As-Grown champion

Table 1 Photovoltaic performance under simulated AM 1.5G illumination. The champion solar cell from each cell type is bolded

Sample	V_{oc}/mV	J_{sc}/mA cm^{-2}	*FF* (%)	η (%)
As-Grown C2R3	482	11.2	69.4	3.75
As-Grown C4R6	**477**	**11.8**	**67.5**	**3.81**
Scatterer C2R4	**499**	**16.6**	**68.0**	**5.64**
Scatterer C3R3	504	15.2	68.8	5.28
PRS C2R5	503	22.2	66.1	7.38
PRS C3R5	500	22.8	67.2	7.65
PRS C4R5	**498**	**24.3**	**65.4**	**7.92**

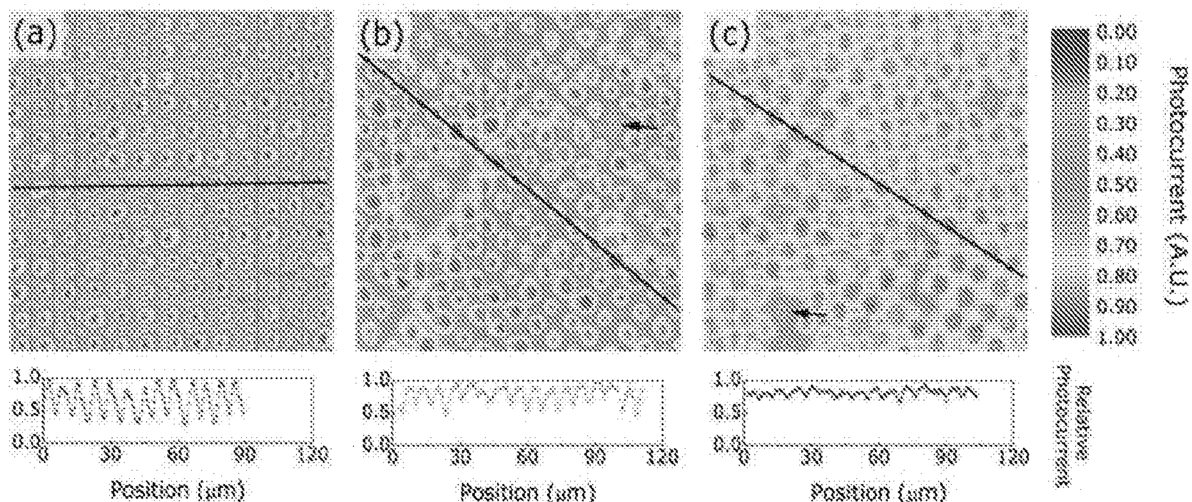

Fig. 4 Scanning photocurrent microscopy (SPCM) images and associated photocurrent line profiles from the center of (a) an As-Grown solar cell, (b) a Scatterer solar cell, and (c) a PRS solar cell. The SPCM images are 90 μm × 90 μm and were normalized to the maximum measured photocurrent in each image. The black lines on each SPCM image denote the cross-section used to produce the associated photocurrent line profiles. The black arrows denote spots of greatly reduced photocurrent believed to result from wires that were not in contact with the ITO.

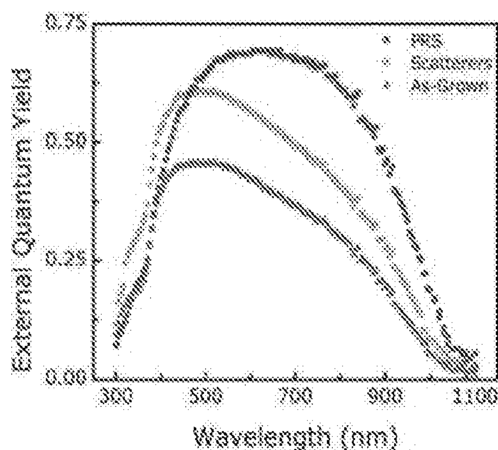

Fig. 5 Spectral response of the champion Si microwire solar cell of each cell type.

solar cell yields a J_{sc} of 12.4 mA cm^{-2}, well below the observed 16.6 mA cm^{-2} J_{sc} for the Scatterer champion solar cell. Thus, the additional active wire length alone cannot explain the increase in J_{sc} from the As-Grown solar cells to the Scatterer solar cells. Second, the Al_2O_3 scattering particles were largely located adjacent to the photo-inactive, thermal-oxide-coated, bases of the wires. Consequently, the full effect of the Al_2O_3 scattering particles is unlikely to have been seen in the Scatterer solar cells. Third, for the PRS and Scatterer cell types, ~2% of the wires in the center of the cell (Fig. 4) and 2–20% of the wires near the perimeter of the cell (Fig. S3†) were not electrically active. Thus, with improved contacting, the PRS and Scatterer cell types would be expected to produce a still slightly higher J_{sc} and η.

Recently, we have demonstrated single-wire solar cells with V_{oc} of up to 600 mV and FF of up to 82%.[3] Additionally, we have previously shown that wire-array photoelectrochemical cells can exhibit near-unity internal quantum yields.[1] Based on these measurements, efficiencies for wire arrays of ~15%, *as compared to the simple theoretical expectation of 17%*, could potentially be achieved by increasing the J_{sc} to 32 mA cm^{-2} (*e.g.*, by using longer wires and increasing the electrically active wire fraction, while accounting for parasitic absorption in the ITO and contact shading), by increasing the FF to 80% (through the addition of a metallic grid on the top contact), and by increasing the V_{oc} to 600 mV.[3] Separately, the design of our p–n junction, which does not extend to the base of the wire array, should prevent shunting of the p–n junction at the back contact in wire-array solar cells that have been removed from the growth wafer.

Acknowledgements

This work was supported by BP and in part by the Department of Energy (Basic Energy Sciences, Energy Frontier Research Center under grant DE-SC0001293 and also grant DE-FG02-07ER46405) and made use of facilities supported by the Caltech Center for Sustainable Energy Research, the Center for Science and Engineering of Materials—an NSF Materials Research Science and Engineering Center at Caltech (DMR 0520565), the Molecular Materials Research Center of the Beckman Institute at Caltech, and the Kavli Nanoscience Institute at Caltech. S.W.B. acknowledges the Kavli Nanoscience Institute for fellowship support, and D.B.T.-E. acknowledges the National Science Foundation for fellowship support. The authors acknowledge Dr Michael Walter for helpful discussions.

References

1 M. D. Kelzenberg, S. W. Boettcher, J. A. Petykiewicz, D. B. Turner-Evans, M. C. Putnam, E. L. Warren, J. M. Spurgeon, R. M. Briggs, N. S. Lewis and H. A. Atwater, *Nat. Mater.*, 2010, **9**, 239–244.
2 S. W. Boettcher, J. M. Spurgeon, M. C. Putnam, E. L. Warren, D. B. Turner-Evans, M. D. Kelzenberg, J. R. Maiolo, H. A. Atwater and N. S. Lewis, *Science*, 2010, 327, 185–187.
3 M. D. Kelzenberg, D. B. Turner-Evans, M. C. Putnam, S. W. Boettcher, R. M. Briggs, C. M. Baek, N. S. Lewis and H. A. Atwater, 2010, submitted.
4 M. C. Putnam, D. B. Turner-Evans, M. D. Kelzenberg, S. W. Boettcher, N. S. Lewis and H. A. Atwater, *Appl. Phys. Lett.*, 2009, **95**, 163116.
5 B. M. Kayes, M. A. Filler, M. C. Putnam, M. D. Kelzenberg, N. S. Lewis and H. A. Atwater, *Appl. Phys. Lett.*, 2007, **91**, 103110.
6 K. E. Plass, M. A. Filler, J. M. Spurgeon, B. M. Kayes, S. Maldonado, B. S. Brunschwig, H. A. Atwater and N. S. Lewis, *Adv. Mater.*, 2009, **21**, 325–328.
7 J. M. Spurgeon, K. E. Plass, B. M. Kayes, B. S. Brunschwig, H. A. Atwater and N. S. Lewis, *Appl. Phys. Lett.*, 2008, **93**, 032112.
8 B. M. Kayes, H. A. Atwater and N. S. Lewis, *J. Appl. Phys.*, 2005, **97**, 114302–114311.
9 M. D. Kelzenberg, M. C. Putnam, D. B. Turner-Evans, N. S. Lewis and H. A. Atwater, in 34th IEEE PVSC, Philadelphia, PA, 2009.
10 J. R. Maiolo, B. M. Kayes, M. A. Filler, M. C. Putnam, M. D. Kelzenberg, H. A. Atwater and N. S. Lewis, *J. Am. Chem. Soc.*, 2007, **129**, 12346–12347.
11 A. P. Goodey, S. M. Eichfeld, K. K. Lew, J. M. Redwing and T. E. Mallouk, *J. Am. Chem. Soc.*, 2007, **129**, 12344–12345.
12 L. Tsakalakos, J. Balch, J. Fronheiser, B. A. Korevaar, O. Sulima and J. Rand, *Appl. Phys. Lett.*, 2007, **91**, 233117.
13 B. Z. Tian, X. L. Zheng, T. J. Kempa, Y. Fang, N. F. Yu, G. H. Yu, J. L. Huang and C. M. Lieber, *Nature*, 2007, **449**, 885–889.
14 M. D. Kelzenberg, D. B. Turner-Evans, B. M. Kayes, M. A. Filler, M. C. Putnam, M. D. Kelzenberg, N. S. Lewis and H. A. Atwater, *Nano Lett.*, 2008, **8**, 710–714.
15 O. Gunawan and S. Guha, *Sol. Energy Mater. Sol. Cells*, 2009, **93**, 1388–1393.
16 T. J. Kempa, B. Z. Tian, D. R. Kim, J. S. Hu, X. L. Zheng and C. M. Lieber, *Nano Lett.*, 2008, **8**, 3456–3460.
17 K. Q. Peng, Y. Xu, Y. Wu, Y. J. Yan, S. T. Lee and J. Zhu, *Small*, 2005, **1**, 1062–1067.
18 E. C. Garnett and P. Yang, *Nano Lett.*, 2010, **10**, 1082–1087.
19 T. Stelzner, M. Pietsch, G. Andra, F. Falk, E. Ose and S. Christiansen, *Nanotechnology*, 2008, **19**, 295203.
20 B. M. Kayes, PhD , California Institute of Technology, 2009.
21 E. C. Garnett and P. D. Yang, *J. Am. Chem. Soc.*, 2008, **130**, 9224–9225.
22 C. Colombo, M. Heiss, M. Gratzel and A. F. I. Morral, *Appl. Phys. Lett.*, 2009, **94**, 173108.
23 Y. J. Dong, B. Z. Tian, T. J. Kempa and C. M. Lieber, *Nano Lett.*, 2009, **9**, 2183–2187.
24 H. Goto, K. Nosaki, K. Tomioka, S. Hara, K. Hiruma, J. Motohisa and T. Fukui, *Appl. Phys. Express*, 2009, **2**, 035004.
25 M. C. Putnam, M. A. Filler, B. M. Kayes, M. D. Kelzenberg, Y. B. Guan, N. S. Lewis, J. M. Eiler and H. A. Atwater, *Nano Lett.*, 2008, **8**, 3109–3113.
26 B. Balakrisnan, S. Patil and E. Smela, *J. Micromech. Microeng.*, 2009, **19**, 047002.

Si Microwire-Array Solar Cells -- Supporting Information

Ag Back Reflector:

Figure S1 provides scanning electron microscope (SEM) images that document the fabrication of a Ag back reflector. Following two 500 nm Ag evaporations Ag uniformly coated the substrate and the wire sidewalls (Fig. S1A). PDMS was then deposited and continuously coated the Ag-coated substrate (Fig. S1A,B). (Because the SEM images shown are from the edge of a wire array, the PDMS is thinner than in the center of the wire array and there exists a small area at the immediate wafer edge where no PDMS coating exists.) A Ag etch was then used to remove any Ag that was not protected by the PDMS film at the base of the wire array (Fig. S1B). After PRS cell fabrication, the PDMS-protected Ag back reflector was revealed by cell cross-sectioning (Fig. S1C).

Separately, the textured nature of the mounting wax, which results from the presence of the Al_2O_3 scattering particles, was visible above the protective PDMS layer (Fig. S1C).

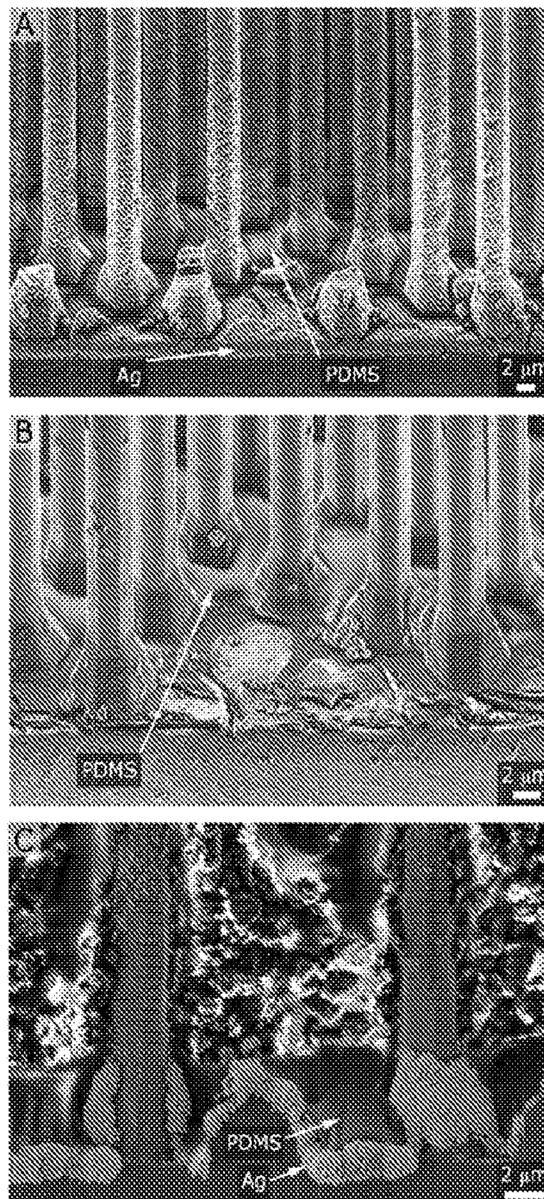

Figure S1. Tilted scanning electron microscope (SEM) images illustrating the fabrication of a Ag back reflector. A) SEM image post Ag and protective polydimethylsiloxane (PDMS) deposition. B) SEM image of the wire array from A) after a Ag-etch. C) Cross-sectional SEM image of a PRS microwire solar cell.

a-SiN_x:H Layer:

Figure S2 is an SEM image of a wire array after selective removal of the *a*-SiN_x:H layer from the wire tips. The bright tip is the c-Si wire, while the darker base is the *a*-SiN_x:H-coated c-Si wire. The difference in the extent of the exposed tip relates to variations in the wire height and variations in the height of the mounting wax etch barrier (removed prior to imaging.)

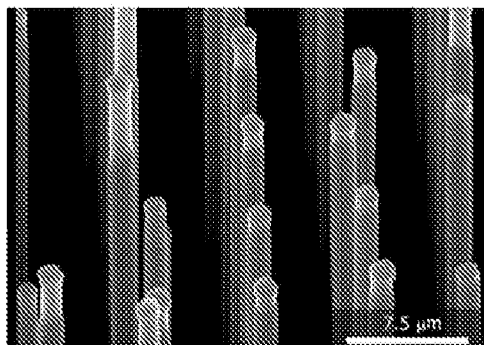

Figure S2. SEM image of a wire array after selective removal of a-SiN_x:H from the wire tips. The mounting wax, which was used as an etch barrier, has been removed from the wire array for clarity.

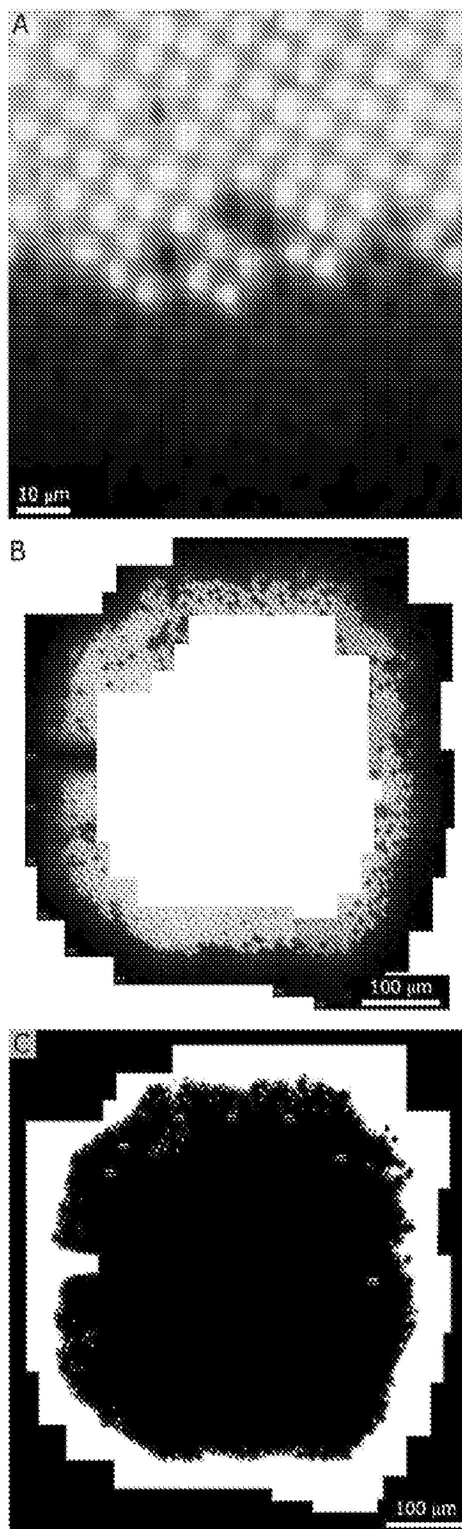

Figure S3. Measuring PRS C4R5's active area. A) 90 μm x 90 μm scanning photocurrent microscopy (SPCM) image along the cell perimeter. B) Twenty-six SPCM images over-laid to map out the cell perimeter. C) Image of B) after thresholding. The blue line is the cell perimeter from which the cell area was calculated.

Cell Area:

Scanning photocurrent microscopy (SPCM) images (90 μm x 90 μm) (Fig. S3A) were overlaid to produce a photocurrent map of the cell perimeter (Fig. S3B), which was then analyzed to calculate the cell area (Fig. S3C).

Area analysis was performed using the 'thresholding' feature in Image J. Thresholding was done in such a way that all of the wires within the cell perimeter (defined by the photoactive wires) were selected. The indent on the left side of the cell resulted from contact shadowing and an appropriate correction to the cell area was made. A small photocurrent signal was present outside of the cell perimeter (Fig. S3A) and is presumed to arise from light that was scattered/reflected into the active area. Though this additional collection area was accounted for during the thresholding process, no correction should have been necessary given that an equivalent amount of light would have also been scattered/reflected out of the cell.

As discussed in the text the dark spots (Fig. S3A,B) indicate wires that are not electrically contacted by the indium tin oxide (ITO). Comparing Fig. S3B with Fig. 4C, the fraction of electrically inactive wires was higher near the cell perimeter (2-20%), which is not unexpected given the decreased ITO thickness at the device edge.

Table S1. V_{oc} and FF (All Devices)

As-Grown:	V_{oc} (mV)	FF (%)
C4R2	401	59.3
C4R3	209	44.9
C4R4	452	61.4
C4R5	257	42.2
C4R6	478	59.1
C3R2	419	43
C3R3	339	52
C3R4	474	66.2
C3R5	453	65.8
C3R6	485	68.4
C2R3	482	69.4
C2R4	492	70.1
C2R5	484	71.6
C2R6	429	59.1
C1R6	463	54.4

Scatterer:	V_{oc} (mV)	FF (%)
C1R1	477	61.7
C2R1	429	54.8
C3R1	387	53.5
C4R1	475	61.4
C1R2	498	67.5
C2R2	503	68.6
C3R2	481	54.3
C4R2	475	65.1
C1R3	497	64.9
C2R3	486	60.4
C3R3	505	68.8
C2R4	499	68

PRS:	V_{oc} (mV)	FF (%)
C2R1	491	59.3
C3R1	487	61.2
C4R1	488	59.7
C5R1	485	61.9
C2R2	497	61
C3R2	493	60.8
C4R2	495	61.1
C5R2	489	60
C2R3	499	63.3
C3R3	497	63
C4R3	495	62.9
C5R3	493	61.5
C2R4	504	62.6
C3R4	494	64.5
C4R4	502	62.5
C5R4	501	61.5
C2R5	503	66.1
C3R5	500	67.2
C4R5	498	65.4
C5R5	497	62.6
C2R6	502	63.4
C3R6	499	63.3
C4R6	489	61
C5R6	485	64.3

V_{oc} and FF:

As seen in Table S1 above, the V_{oc} and FF were remarkably consistent for the PRS solar cells. The V_{oc} and FF were also consistent between the best Scatterer and As-Grown solar cells, however some cells with lower V_{oc} and FF were observed. For the As-Grown solar cells, obvious fabrication defects (cracking of the mounting wax prior to ITO deposition) may have resulted in the larger variation in cell performance. Between cells with similar performance (within each respective cell type), we attribute much of the variation in FF to the observed variations in the probe tip to ITO contact resistance.

Indium Tin Oxide:

Figure S4 plots the transmission as a function of wavelength for a glass coverslip with and without a 150 nm-thick indium tin oxide (ITO) layer. Transmission through the ITO was found to be > 80% for wavelengths > 500 nm, and at least 65% for wavelengths between 400 and 500 nm.

Strong oscillations in transmission were observed as a result of Fabry-Pérot interference. Thus, a 5 nm running average was used to smooth the oscillations in transmission for wavelengths > 700 nm. As can be seen by comparing the smoothed data below, the oscillations were inherent to the thin nature of the glass coverslip.

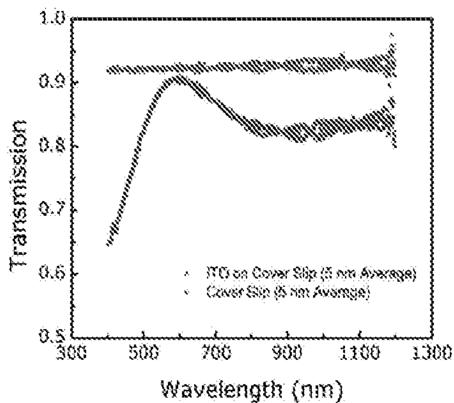

Fig. S4. Transmission as a function of wavelength for a glass coverslip with and without a 150 nm-thick indium tin oxide coating. A 5 nm running average was applied to smooth the oscillations in transmission at wavelengths greater than 700 nm.

Experimental:

Wire Array Growth. Si microwire arrays were grown as described previously.[5] The growth substrates were boron-doped p^{++}-Si (111) wafers, having a resistivity, $\rho < 0.001$ $\Omega\cdot$cm, that were coated with 450 nm of thermal oxide (Silicon Quest International). Arrays of 4-μm-diameter circular holes, on a square lattice with a 7 μm pitch, were defined in the oxide by photolithographic exposure and development of a photoresist layer (Microchem S1813), followed by a buffered HF(aq) (BHF) etch (Transene Inc.) The holes were then filled with 600 nm of Cu (ESPI metals, 6N) via thermal evaporation onto the patterned photoresist, followed by liftoff. Patterned substrates approximately 1.5 cm × 1.5 cm in dimension were then annealed in a tube furnace for 20 min at 1000 °C under H_2 flowing at a rate of 500 sccm. Wire growth was performed by the introduction of $SiCl_4$ (Strem, 99.9999+%), BCl_3 (Matheson, 0.25% in H_2), and H_2 (Matheson, research grade) at flow rates of 10, 1.0, and 500 sccm, respectively, for 30 min. Following growth, the tube was purged with N_2 at 200 sccm and was allowed cool to ~ 650 °C over the course of ~30 min.

p-n Junction Fabrication. Following growth the Cu catalyst was removed from the wire arrays by etching in 5% HF(aq) for 30 s, 6:1:1 by volume H_2O:H_2O_2(30% in H_2O):conc. HCl (aq.) at 75 °C for 15 min, and 20 wt % KOH (aq.) at 20 °C for 60 s. A conformal SiO_2 diffusion-barrier that was 200 nm in thickness was grown via dry thermal oxidation at 1100 °C for 2 h. The wire array samples were then coated with a solution that contained 4.4 g hexamethycyclotrisiloxane (Sigma-Aldrich), 1 g PDMS (Sylgard 184, Dow Corning), and 0.10 g of curing agent in 5 ml of dicholoromethane; spun at 1000 RPM for 30 s; and cured at 150 °C for 30 min, to produce a 10–20 μm thick PDMS layer selectively at the base of the wire array.[6] After a quick etch (~2 s) in a 1:1 mixture of 1.0 M tetrabutylammonium fluoride in tetrahydrofuran (Sigma-Aldrich) and dimethylformamide (PDMS etch)[26] and a DI rinse, these partially infilled arrays were immersed for 5 min in BHF, to remove the exposed diffusion-barrier oxide. The PDMS was then completely removed by etching for 30 min in PDMS etch. A 10 min piranha etch (3:1 aq. conc. H_2SO_4:H_2O_2) was performed to remove residual organic contamination. After etching the wires for 5 s in 10% HF (aq), thermal P diffusion was performed using solid source CeP_5O_{14} wafers (Saint-Gobain, PH-900 PDS) at 850 °C for 10 min (As-Grown and Scatterer) or 15 min (PRS) under an N_2 ambient, to yield a

radial p-n junction in the wire regions unprotected by the thermal oxide. A 30 s etch in BHF was used to remove the surface dopant glass.

Photovoltaic Device Fabrication. The *As-Grown* cell was fabricated as follows. After p-n junction fabrication, the wire array was heated to 150 °C on a hot plate, and mounting wax (Quickstick 135, South Bay Tech.) was melted into the array. Excess wax was removed from the array using a glass coverslip. The mounting wax was then etched in an O_2 plasma (400 W, 300 mTorr) until the wire tips were sufficiently exposed for electrical contacting (30-90 min). After etching with BHF for 30 s, 150 nm of indium tin oxide [0.0007 Ω·cm] was sputtered (48 W, 3 mTorr, 20:0.75 sccm Ar:10% O_2 in Ar) through a shadow mask, to serve as a transparent contact to the n-type shell of the Si microwires, thereby defining the area of the microwire solar cells. Contact to the p-type core of the Si microwires was established through the p^+-Si substrate by scribing a Ga/In eutectic onto the back side of the growth wafer.

Fabrication of the *Scatterer* cell was performed identically to that of the As-Grown cell, except that prior to infilling with wax, Al_2O_3 light-scattering particles (0.08 μm nominal-diameter, South Bay Technology) were added to the wire array. The wire-array was placed face-up in a flat-bottomed glass centrifuge tube and ~ 3 ml of an ethanolic dispersion of the particles (~0.3 mg/ml) were added. Centrifugation (~3000 RPM) for 5 min was used to drive the particles to the base of the wire-array.

Fabrication of the *PRS* cell was performed identically to that for the Scatterer cell, except that prior to the addition of the Al_2O_3 particles, an a-SiN_x:H passivating layer and a Ag back reflector were added to the cell. After p-n junction fabrication, the wire arrays were etched for 5 min in BHF, to completely remove the remaining oxide diffusion barrier. A standard clean was then performed (10 min in 5:1:1 by volume H_2O:H_2O_2(30% in H_2O): NH_4OH(15% in H_2O) at 75 °C, 30 s in BHF, 10 min in 6:1:1 by volume H_2O:H_2O_2(30% in H_2O):conc. HCl (aq.) at 75 °C, 30 s in BHF), prior to deposition of an a-SiN_x:H layer (~ 140 nm thick at the wire tip and ~ 60 nm thick at the wire base) using plasma-enhanced chemical vapor deposition, as described previously.[1] The a-SiN_x:H was then etched for 15 s in BHF, prior to the deposition of a total of 1 μm planar-equivalent of Ag via thermal evaporation (two successive 500 nm evaporations at two different specimen-tilt angles (± ~5 degrees) with

sample rotation, to ensure continuous coverage of the growth substrate). The array was then infilled with ~5 μm of PDMS using a process similar to the one described above. This PDMS etch barrier allowed the Ag at the wire tips and sidewalls to be selectively removed by etching for 6.5 min in 8:1:1 methanol: NH_4OH(15% in H_2O): 30 wt.% aq. H_2O_2. A thin layer (~40 nm) of SiO_2 was then sputtered to improve the incorporation of the Al_2O_3 particles. The Al_2O_3 scattering elements, mounting wax, and ITO were then added as described above.

Characterization. Dark and light current-voltage measurements were performed on a probe station with a 4-point source-measure unit (Keithley 238). Contact to the ITO top contact was made with a micromanipulator-controlled Au-coated tungsten probe tip. Simulated solar illumination was provided by a 1000 W Xe arc lamp with air mass (AM 1.5G) filters (Oriel), calibrated to 1-sun illumination by an NREL-traceable Si reference cell (PV Measurements, Inc.). Spectral response measurements were performed in an overfilled geometry using chopped (30 Hz) illumination from a 300 W Xe arc lamp coupled to a 0.25 m monochromator (Oriel) that provided ~2 nm spectral resolution. The specimen photocurrent was normalized (by area) to that of a 3 mm-diameter calibrated photodiode, to determine the external quantum yield. The signals were measured with independent lock-in detection of the sample and calibration channels. Scanning photocurrent microscopy measurements were performed using a confocal microscope (WiTEC) in a light-beam-induced current (LBIC) configuration described previously.[9] Scanning photocurrent microscopy (SPCM) images were formed by rastering each device beneath a ~1.0 μm-diameter laser spot (λ = 650 nm) while recording the short-circuit current (0 V bias) under otherwise dark conditions. Multiple 90 μm x 90 μm SPCM images were manually stitched together and post-processed to determine the active cell area using image processing software (Image J) (see Supporting Information Fig. S3.)

APPENDIX 2

Fabrication of Wire-Array Solar Cells

The inventions disclosed relate to the development of a new type of solar cell for the conversion of solar energy into either electrical or chemical energy.

The new type of solar cell involves the use of a structured semiconductor with high-aspect ratio dimensions. Two primary advantages of such a semiconductor are the dramatically reduced usage of semiconducting material and the ability to easily incorporate light trapping elements that ensure the efficient collection of all incident illumination.

In particular we have fabricated solar cells from arrays of vertically-aligned wires (which happen to be a few microns in diameter)

The most basic design involves the use of **1)** a transparent structural and dielectric infill (mounting wax). This mounting wax ensures effective electrical isolation between the n and p layers of the solar cell and planarizes the three-dimensional array, reducing the area that a top contact (presumably a transparent conducting oxide (TCO)) must cover.

More importantly, the mounting wax can be used **2)** as an etch mask in subsequent processing steps. By infilling the entire array with mounting wax and using O2 plasma etching, one can remove the mounting wax until a desired height is reached. Once a desired height has been reached, **3)** processing steps (such as wet chemical etches, e.g. etching a-Si_3N_4:H or SiO_2 in hydrofluoric acid) can be performed without affecting the wire array that is still covered by the mounting wax. This is how we locally remove our a-SiN_x:H passivation layer from the wire tips prior to the deposition of our TCO.

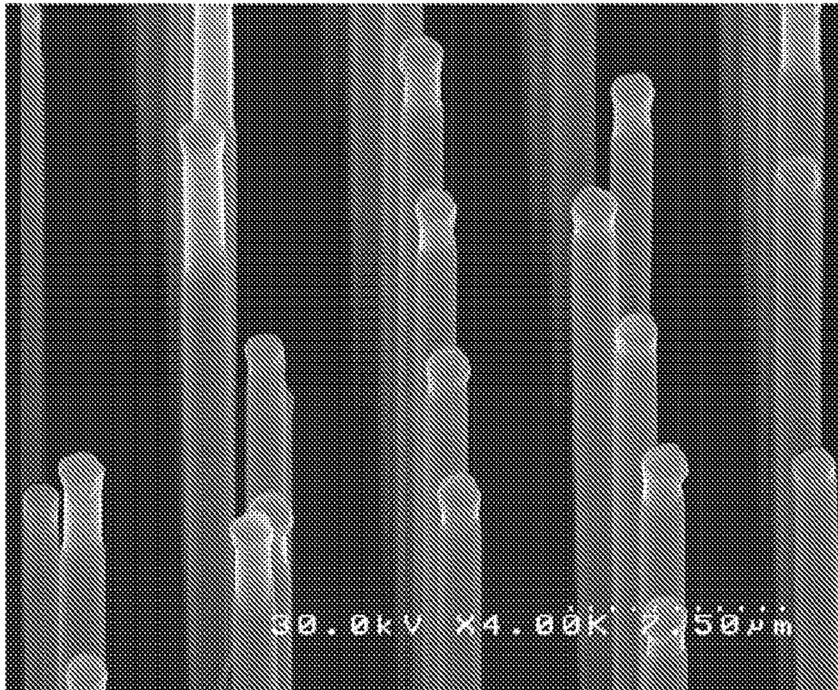

SEM image demonstrating the selective removal of a-SiN_x:H from the tips of the wires. The mounting wax has been removed for clarity.

4) For the successful use of mounting wax a slow cool step post infill (melt in) at 150 C was found to be critical to prevent the formation of large cracks (looks like dried mud), which prevent the formation of a continuous top-contact.

More advanced solar cell designs employ the use of Al_2O_3 scattering particles and a Ag back reflector. Both the use of Al_2O_3 scattering particles and a Ag back reflector have been discussed in one of our recent provisional patents. However in this work we developed **5)** a process for the deposition of a Ag back reflector in a wire array affixed to a substrate.

A reflective metal (Ag) was evaporated in such a manner (the use of sample rotation and the use of multiple evaporation angles) as to conformally coat the substrate (and the wires). In a process nominally identical to one of our previous provisional patents PDMS was then drop cast onto the substrate so as to produce a thin layer at the base of the wires. This thin layer of PDMS served as an etch barrier, such that a Ag etch could be performed to remove the Ag at the wire tips and sidewalls (where it would prevent the wires from absorbing the incident light) without removing the Ag from the substrate. Thus the fabrication of a Ag reflecting layer that exists only at the base of the wire array was achieved.

6) The deposition of a transparent top contact (TCO, specifically Indium Tin Oxide (ITO)) was used to produce a top contact that connected all of the wires together. ITO deposited at lower operating voltages was found to produce devices with higher open-circuit voltages. Presumably because the wires have a shallow pn-junction which was being damaged while sputtering at higher operating voltages.

7) Scanning photocurrent microscopy was demonstrated to be capable of resolving the photocurrent from individual wires in wire array solar cells. This may prove to be useful in indentifying local regions with poor performance in larger area solar cells so that subsequent processing steps can be used to remove the damaged cell regions (laser ablation ?)

Abstract

Si microwire array solar cells with open-circuit voltages of 500 mV, short-circuit current densities (J_{sc}) up to 24 mA/cm^2, and fill factors > 65% have been fabricated, achieving an AM 1.5G conversion efficiency up to $\eta = 7.9\%$ using a volume of Si equivalent to a < 7 μm thick Si wafer. These solar cells include Al_2O_3 dielectric particles that scatter light incident in the space between the wires, a Ag back reflector that prevents the escape of incident illumination from the back surface of the solar cell, and an *a*-SiN_x:H passivation/antireflection layer. Solar cells without some or all of these design features were also fabricated and used to demonstrate that a cell design that includes light trapping features is important to achieving high J_{sc}. Two-dimensional mapping of the photocurrent response within microwire array solar cells revealed that the higher J_{sc} of the most advanced cell design resulted from an increased efficiency in harvesting light incident in the space between wires.

Vertically aligned arrays of crystalline-Si (c-Si) microwires provide a photovoltaic geometry that enables the possibility for flexible c-Si solar cells with near unity internal quantum yield and capable of the absorption of > 85% of the day-integrated (above bandgap) solar illumination using a volume of Si equivalent to a 2.8 μm thick Si film.[1] Two advantages conferred by the three-dimensional geometry of vertically aligned, high-aspect ratio Si microwires are 1) the ability to create high-quality single crystal Si structures with passivated surfaces via a vapor growth process and 2) enhanced absorption relative to planar c-Si absorbers. Vapor phase growth of high-quality c-Si wires with large minority-carrier diffusion lengths is possible via a copper-catalyzed vapor-liquid solid chemical vapor deposition growth process[2]. The incorporation of light scattering particles located in the space between adjacent wires in combination with a metallic back reflector has recently been reported to enable very effective light trapping.[1] These two advantages in combination with the ability to grow arrays of Si microwires over large areas (> 1 cm^2)[3], to peel the the wire arrays from the growth substrate in a flexible polymer[4], and to re-use the growth substrate[5], offer the exciting possibility of fabrication of flexible, high efficiency c-Si solar cells.[6]

Wire solar cells have been fabricated using materials including c-Si[7 8 9 10 11 12 13 14 15 16], amorphous-Si[17], GaAs[18], III-Nitride[19], and InP[20] and via a variety of growth techniques including vapor-liquid-solid growth[4-13], metal-catalyzed chemical etching[11,14], molecular beam epitaxy[15], metal-organic chemical vapor deposition[16,17], and deep reactive-ion-etching[12]. In particular, the vapor-liquid-solid (VLS) chemical vapor deposition (CVD) growth method offers a materials-efficient, and scaleable route for the fabrication of

semiconducting wires. However, initial results for VLS-grown, c-Si, wire array and single wire solar cells have fallen short of photovoltaic performance predicted from simple considerations.[2] In particular these solar cells have failed to demonstrate high open-circuit voltages (V_{oc}), possibly indicative of significant recombination within the cell's depletion region.[2,21] Recently we have demonstrated >10 μm bulk minority-carrier diffusion lengths[22] and high V_{oc} (450 mV – near the limit of our photoelectrochemical cell's redox electrolyte system) and near-unity internal quantum yield for carrier collection in Cu-catalyzed, BCl_3 doped, Si microwires.[23,24] These results are indicative of a significant improvement in our materials quality and suggest the possibility for the fabrication of highly efficient solar cells.

Here we report on c-Si microwire array solar cells with V_{oc} = 500 mV, short-circuit current densities (J_{sc}) up to 24 mA/cm^2, and fill factors (FF) > 65% that achieve the 7.9% efficient conversion of AM 1.5G solar simulation to electrical energy with negligible photovoltaic response from the growth substrate. The most efficient cell design employed Al_2O_3 light scattering particles, an a-SiN_x:H passivation/antireflection layer and an Ag back reflector which we have previously shown to enhance optical absorption in microwire arrays.[1] Two-dimensional photocurrent mapping of Si microwire solar cells demonstrated improved collection of light incident between wires for cells employing these light trapping elements as compared to cells without light trapping elements. For all of the microwire solar cells studied the growth substrate provided no appreciable photovoltaic response.

Square-arrays of vertically-aligned Si microwires 2-3 μm in diameter on a 7 μm pitch were grown on a p^{++} Si (111) substrate using the vapor-liquid-solid (VLS) growth method as described previously.[3] The Si microwires were doped p-type during the growth process using BCl_3 as a gaseous dopant source. Four-point probe measurements of wires that were removed Si wire arrays grown under nominally identical growth conditions indicated that the wires were *p*-type with $\rho = 0.05$ Ω-cm. This value corresponds to an acceptor concentration N_A of 7×10^{17} cm^{-3}, assuming a bulk hole mobility (1.8×10^{2} cm^{2} V^{-1} s^{-1}) for Si.

A radial pn-junction was then defined as illustrated in Figure 1 and described below. As-grown wire arrays (Fig. 1*A*) were etched to remove the Cu-catalyst and a thin layer (~50 nm) of surface Si prior to the growth of a 200 nm thermal oxide (Fig. 1*B*). The thermal oxide was then selectively etched in a hydrofluoric acid (HF) solution (aq.) using polydimethylsiloxane (PDMS) as an etch barrier for the thermal oxide at the base of the microwires (Fig. 1*C*). After removal of the PDMS, radial pn-junctions were formed in the region of the Si microwires where a thermal oxide was not present during a phosphorous diffusion – the thermal oxide functions as a phosphorous diffusion barrier (Fig. 1*D*). Note that by appropriately choosing the thickness of the PDMS layer, the pn-junction can be defined in such a way as to approximate either a radial or an axial pn-junction, or some combination of the two (as in the PRS cell below). Equally importantly, the pn-junction does not extend to the base of the wire array, thus a back contact can be fabricated to a wire array which has been removed from the growth

substrate without fear of shunting the pn-junction.

Three different types of Si microwire solar cells were fabricated. The as-grown cell contained no light trapping elements or surface passivation. The scatterer cell incorporated light-scattering Al_2O_3 particles (nominally 80 nm in diameter) in-between the wires. The PRS cell contained an *a*-SiN_x:H passivation layer to minimize surface recombination and serve as an anti-reflection coating, a Ag back reflector to prevent the loss of incident illumination into the growth substrate, and Al_2O_3 particles to scatter light incident between the Si microwires. Following the inclusion of the selected light-trapping elements (see Methods), each wire array sample was filled to the tips of the wires with mounting wax, which served as a structural support for a sputtered indium tin oxide (ITO) ($\rho \sim 0.0007$ Ω-cm) top-contact pad.

Cross-sectional scanning electron microscope (SEM) images of a wire array after radial pn junction formation and for each microwire solar cell type are shown in Fig. 2. As seen in Fig. 2*A* the height of the thermal oxide (and thus the location of the radial pn-junction) is uniform across the wire array. Wire heights range from 57-63 µm, 71-78 µm, and 43-49 µm for the as-grown (Fig. 2*B*), scatterer (Fig. 2*C*), and PRS (Fig. 2*D*) microwire solar cells, respectively. Thermal oxide covers the lower 27-31 µm of the as-grown solar cells and 29-32 µm for the scatterer solar cells. These wire and thermal oxide heights translated to active wire lengths of 27-33 µm (as-grown), 41-48 µm (scatterer), and 43-49 µm (PRS). For the scatterer cells, the 80 nm Al_2O_3 particles are observed to form micron-sized agglomerates that are located primarily near the base of the wire array, as

evidenced by the granular texture of the mounting wax near the base of the wire array. A fraction of the Al_2O_3 particles are also found to coat the wire tip and sidewalls (Fig. 2*C*, inset.) For the PRS solar cells, the Al_2O_3 particles again collect near the base of the wire array but an increased fraction are found on the wire surfaces (Fig. 2*D*, inset.) The Ag back reflector in the PRS solar cells is visible covering the growth substrate and the tapered base of the wires (Fig. 2*D* and Supporting Information, SFig. 2). For all devices, the mounting wax was observed to uniformly infill the wire array. Additionally, the ITO was observed to conformally coat the mounting wax and the wire tips, thereby providing a continuous top contact despite the highly textured surface.

An important consideration for on-substrate measurement of the photovoltaic performance of wire-array solar cells is the current contribution from the growth substrate. Scanning photocurrent microscopy measurements indicate a < 0.5 μm minority-carrier diffusion length for electrons in the p-type wire core beneath the 200 nm thermal oxide, apparently due to a high surface recombination velocity.[24] Thus consequently photovoltaic response is not possible from either the growth substrate or the lower 27-32 μm of wires for both as-grown and scatterer microwire solar cells. For the PRS microwire solar cells, thermal oxide removal followed by the deposition of the *a*-SiN_x:H passivation layer produces an electron minority-carrier diffusion length $>> 30$ μm in the p-type wire core.[24] Hence photovoltaic response from the entire length of the wire and the substrate is possible. However the photovoltaic contribution from the substrate should be negligibly small. The optically-thick Ag back reflector will ensure that only illumination passing through the Si microwires is able to reach the substrate.

Therefore 95% of the illumination ≤ 800 nm should be absorbed over the 43-49 μm length of the wires according to a simple Beer-Lambert's law analysis. The remaining illumination will enter a p^{++} Si substrate ($\rho < 0.001$ Ω-cm) that has been shown to exhibit an external quantum yield < 0.05 for 800 nm -1100 nm illumination.[23.1]

In total, 15 as-grown cells, 12 scatterer cells, and 24 PRS cells were fabricated. The area of the fabricated cells spanned a range from 0.12 to 0.21 mm^2 as a result of variations in the distance between the top of the microwire arrays and the shadow mask during ITO deposition. For each cell type, the majority of cells was found to exhibit similar open-circuit voltages and fill-factors (see Supporting Information). In order to convert the measured short-circuit current to a short-circuit current density and to calculate a cell efficiency, scanning photocurrent microscopy measurements were performed to accurately determine the cell areas of 2-3 cells from each cell type by producing a photocurrent map of the cell perimeter (see Supporting Information, SFig. 1).

The current density as a function of voltage is plotted in Fig. 3 for the champion microwire solar cell of each cell type in the dark (Fig. 3*A*) and under 100 mW cm^{-2} of simulated AM 1.5G illumination (Fig. 3*B*). In the dark, each microwire solar cell type exhibits the diode behavior characteristic of a pn-junction with an exponential increase in current density under forward-bias ($V > 0$) and a greatly reduced current density under reverse-bias ($V < 0$). The roll-off in the current density near 0.5 V in forward-bias results from the series resistance of the solar cells, which ranged from 300 to 3000 ohms and was dependent upon the quality of the contact between the electrical probe and the ITO.

The diode ideality factor for all three solar cell types was ~ 1.8. Additionally, all three solar cell types exhibited a similar saturation-current density of ~ 0.001 mA/cm^2. Normalizing the saturation-current density per wire yields a saturation-current per wire of 5×10^{-10} mA, which is close to the measured saturation-current per wire of 1×10^{-10} mA for single microwire solar cells.[24]

Under simulated AM 1.5G illumination, the champion PRS solar cell exhibited a marked improvement in the short-circuit current density (J_{sc}) over the champion scatterer solar cell (24.3 mA/cm^2 vs. 16.6 mA/cm^2), which in turn exhibits a marked improvement in J_{sc} over the champion as-grown solar cell (16.6 mA/cm^2 vs. 11.2 mA/cm^2, Fig. 2*B*). This trend ($J_{sc,\ PRS} > J_{sc,\ Scatterer} > J_{sc,\ As\text{-}Grown}$) suggests that the use of optical light trapping elements (back reflector and dielectric scattering particles) is critical for realizing high J_{sc}.

The open-circuit voltage (V_{oc}), J_{sc}, fill-factor (FF), and cell efficiency (η) for all microwire solar cells with cell areas measured by SPCM are displayed in Table 1. V_{oc}'s near or above 500 mV and $FF > 65$ can be seen for all three cell types. We estimate the internal error in the measurement of the cell area to be 2% and the internal error in the AM 1.5G illumination intensity to be 5%, yielding a ~ 5 % internal error in the measurement of the cell efficiency.

To better understand the differences in J_{sc} between the PRS, Scatterer, and As-Grown solar cells, scanning photocurrent microscopy (SPCM) studies were undertaken to produce two-dimensional maps of the photocurrent as a function of local laser illumination (λ = 650 nm, ~ 500 nm beam waist). As can be seen in Fig. 4, the photocurrent is largest when the laser illumination is centered on a wire and lowest when centered between four adjacent wires. The magnitude (both relative and absolute) of the decay in photocurrent as the laser moves from a peak (centered on a wire) to a valley (between two adjacent wires) can be clearly seen to decrease from the as-grown cell (Fig. 4*A*) to the scatterer cell (Fig. 4*B*) and to decrease again from the scatterer cell to the PRS cell (Fig. 4*C*). The PRS solar cell exhibits nearly uniform absorption across the array, demonstrating that the Ag back reflector and Al_2O_3 dielectric scattering particles are capable of ensuring the collection of light incident between wires, whereas the as-grown and scatterer cells capture significantly less of the light incident between wires.

The two-dimensional photocurrent maps for both the scatterer and PRS solar cells exhibit four 'dead' spots where the photocurrent is greatly reduced. These dead spots coincide exactly with the location of a wire but are not correlated with defects in the wire array. Noting that the photocurrent is markedly decreased even when compared with the valley photocurrent and that uncontacted would be expected to produce a lower photocurrent response than wire vacancies because of their parasitic optical absorption, we conclude that these dead spots arise from wires that are present but not electrically contacted by the ITO.

In addition to measuring the photocurrent as a function of local laser illumination, the external quantum yield (EQY) for the champion cell of each cell type was measured from 300 nm to 1100 nm using a calibrated AM1.5G solar simulator. As seen in Fig. 5, the as-grown and scatterer solar cells have similarly shaped spectral response curves (though different in absolute magnitude), both exhibiting decay in the EQY starting around 550 nm. The shape of the spectral response curves for the as-Grown and scatterer solar cells agrees well with the shape of the recently reported optical absorption for Si microwire arrays with similar wire diameters and heights on the same square lattice with 7 μm pitch.[1] By comparison, the external quantum yield for the PRS solar cell is nearly constant between 500 nm and 800 nm, demonstrating the importance of a combination of light trapping elements for capturing photons of wavelengths where the absorption coefficient in c-Si is small (the absorption coefficient in c-Si decreases with increasing wavelength). Integrating the observed external quantum yield with the AM 1.5 solar spectrum predicts J_{sc} of 12.0 mA/cm^2, 18.0 mA/cm^2, and 23.3 mA/cm^2 for the As-Grown, Scatterer, and PRS solar cells respectively, in good agreement with the measured J_{sc}.

In conclusion we have demonstrated that microwire array solar cells fabricated from arrays of VLS-grown Si microwires can exhibit significant photovoltaic performance, achieving $V_{oc} > 500$ mV, $J_{sc} > 24$ mA/cm^2, FF approaching 70%, and $\eta = 7.9$ % with negligible photovoltaic response from the growth substrate. We have also shown that the combination of a Ag back-reflector and Al_2O_3 dielectric scattering particles enable the

efficient collection of light incident across the wire array, including light incident between wires. We anticipate that efficiencies of ~ 15% could potentially be achievement by optimization of J_{sc} (e.g., by using longer wires), FF (addition of a metallic grid on the top contact), and V_{oc} (improved surface passivation and junction engineering.)

Acknowledgements:

This work was supported by BP and in part by the Department of Energy, Basic Energy Sciences Energy Frontier Research Center program under grant DE-SC0001293 and also grant DE-FG02-07ER46405, and made use of facilities supported by the Caltech Center for Sustainable Energy Research, the Center for Science and Engineering of Materials - an NSF Materials Research Science and Engineering Center at Caltech (DMR 0520565), the Molecular Materials Research Center of the Beckman Institute at Caltech, and the Kavli Nanoscience Institute at Caltech. S.W.B. acknowledges the Kavli Nanoscience Institute for fellowship support. The authors acknowledge Dr. Michael Walter for helpful discussions.

Methods:

Wire Array Growth. Si microwires arrays were grown as previously described.[3] The growth substrates were boron-doped p^{++}-Si (111) wafers, having a resistivity, ρ <

0.001 Ω cm, that were coated with 450 nm of thermal oxide (Silicon Quest International). Arrays of 4-μm-diameter circular holes, on a square lattice with a 7 μm pitch, were defined in the oxide by photolithographic exposure and development of a photoresist layer (Microchem S1813) followed by a buffered HF(aq) etch. The holes were then filled with 600 nm of copper (ESPI metals, 6N) via thermal evaporation onto the patterned photoresist, followed by a subsequent liftoff of the resist. Patterned substrates approximately 1.5 × 1.5 cm in dimension were then annealed in a tube furnace for 20 min at 1000 °C under H_2 flowing at a rate of 500 sccm. Wire growth was performed by the introduction of $SiCl_4$ (Strem, 99.9999+%), BCl_3 (Matheson, 0.25% in H_2), and H_2 (Matheson, research grade) at flow rates of 10, 1.0, and 500 sccm, respectively, for 30 min. Following growth, the tube was purged with N_2(g) at 200 sccm and was allowed cool to ~ 650 °C over the course of ~30 min.

pn junction fabrication. The Cu catalyst was removed from the wire arrays following growth by etching in 5% HF(aq) for 30 s, 6:1:1 by volume H_2O:H_2O_2(30% in H_2O):conc. HCl (aq.) at 75 °C for 15 min, and 20 wt % KOH (aq.) at 20 °C for 60 s. A conformal SiO_2 diffusion-barrier 200 nm in thickness was grown via dry thermal oxidation at 1100 °C for 2 hr. The wire array samples were then coated with a solution containing 4.4 g hexamethycyclotrisiloxane (Sigma-Aldrich), 1 g PDMS (Sylgard 184, Dow Corning), and 0.10 g curing agent in 5 ml of dicholoromethane; spun at 1000 RPM for 30 s; and cured at 150 °C for 30 min, in order to produce a 10–20 μm thick PDMS layer selectively at the base of the wire array.[4] These partially infilled arrays were then immersed for 5 min in buffered HF (BHF) to remove the exposed diffusion-barrier oxide, after which the PDMS was removed by etching for 30 min in a 1:1 mixture of 1.0 M

tetrabutylammonium fluoride in tetrahydrofuran (Sigma-Aldrich) and dimethylformamide.[25] A 10 min piranha etch (3:1 aq. conc. H_2SO_4:H_2O_2) was performed to remove residual organic contamination. After etching the wires for 5 s in 10% HF (aq), thermal P diffusion was performed using solid source CeP_5O_{14} wafers (Saint-Gobain, PH-900 PDS) at 850°C for 10 min (As-Grown and Scatterer) or 15 min (PRS) under an N_2 ambient to yield a radial pn junction in the wire regions unprotected by the thermal oxide. A 30 s etch in BHF was used to remove the surface dopant glass.

Photovoltaic device fabrication. Three variations of Si microwire solar cells, As-Grown, Scatterer, and passivation-scatterer-reflector (PRS), were fabricated from the pn-junction wire arrays.

The As-Grown cell was fabricated as follows. The pn wire array was heated to 150 °C on a hot plate and mounting wax (Quickstick 135, South Bay Tech.) was melted into the array. Excess wax was removed from the array with a glass coverslip. The mounting wax was then etched in a O2 plasma (400 W, 300 mT) until the wire tips were sufficiently exposed for electrical contacting (30-90 min). After etching with buffered HF (BHF) for 30 s, 150 nm of indium tin oxide [0.0007 Ω-cm] was sputtered (48 W, 3 mTorr, 20.7:0.075 sccm Ar:O_2) through a shadow mask to serve as a transparent contact to the n-type shell of the Si microwires, thereby defining the area of the microwire solar cells. Contact to the p-type core of the Si microwires was established through the p^+-Si substrate by scribing a Ga/In eutectic onto the back side of the substrate.

Fabrication of the Scatterer cell was performed identically to that of the As-Grown cell, except that prior to infilling with wax, light-scattering particles (0.08 μm nominal-diameter Al_2O_3, South Bay Technology) were added to the wire array. The

wire-array was placed face-up in a flat-bottomed glass centrifuge tube and ~ 3 ml of an ethanolic dispersion of the particles (~0.3 mg/ml) were added. Centrifugation (~3000 RPM) for 5 min was used to drive the particles to the base of the wire-array.

Fabrication of the PRS cell was performed identically to that for the Scatterer cell, except that prior to the addition of the Al_2O_3 particles, a passivating layer and back reflector were added to the cell. After definition of the radial-pn junction, the wire arrays were etched for 5 min in BHF to completely remove the oxide diffusion barrier. The wire arrays then underwent the full standard clean for c-Si (10 min in 5:1:1 by volume H_2O:H_2O_2(30% in H_2O): NH_4OH(15% in H_2O) at 75 °C, 30 s in BHF, 10 min in 6:1:1 by volume H_2O:H_2O_2(30% in H_2O):conc. HCl (aq.) at 75 °C, 30 s in BHF), prior to deposition of an a-SiN_x:H layer (~ 140 nm thick at the wire tip and ~ 60 nm thick at the wire base) using plasma-enhanced chemical vapor deposition as described previously.[1] The a-SiN_x:H was then etched for 15 s in BHF prior to the deposition of a total of 1 μm planar-equivalent of Ag via thermal evaporation (two subsequent 500 nm evaporations at two different angles (± ~5 degrees) with sample rotation to ensure continuous coverage of the growth substrate). The sample was then coated with a solution containing 4.4 g hexamethycyclotrisiloxane, 0.5 g PDMS, and 0.05 g curing agent in 5 ml of dicholoromethane, spun at 1000 RPM for 30 s, and cured at 150 °C for 30 min, in order to produce a ~5-10 μm thick PDMS layer selectively at the base of the wire array. This PDMS etch barrier allowed the Ag at the wire tips and sidewalls to be selectively removed by etching for 6.5 min in 8:1:1 methanol: NH_4OH(15% in H_2O): 30 wt.% aq. H_2O_2. Al_2O_3 scattering elements, mounting wax, and ITO were then added as described above.

Characterization. Dark and light current-voltage measurements were performed on a probe station with a 4-point source-measure unit (Keithley 236). Contact to the ITO top contact was made with a micromanipulator-controlled Au-coated tungsten probe tip. Solar simulation was provided by a 1000 W Xe arc lamp with air mass (AM 1.5G) filters (Oriel), calibrated to 1-sun illumination by an NREL-traceable Si reference cell (PV Measurements, Inc.). Spectral response measurements were made in an overfilled geometry using chopped (30 Hz) illumination from a 300 W Xe arc lamp coupled to ¼ m monochromator (Oriel) that provided ~2 nm spectral resolution. Specimen photocurrent was normalized (by area) to that of a 3 mm-diameter calibrated photodiode to determine external quantum efficiency. The signals were measured with independent lock-in detection of the sample and calibration channels. SPCM measurements were performed using a confocal microscope (WiTEC) in a light-beam-induced current (LBIC) configuration. SPCM images were formed by rastering each device beneath a ~0.5 μm laser spot (λ = 650 nm) while recording the short-circuit current (0 V bias).

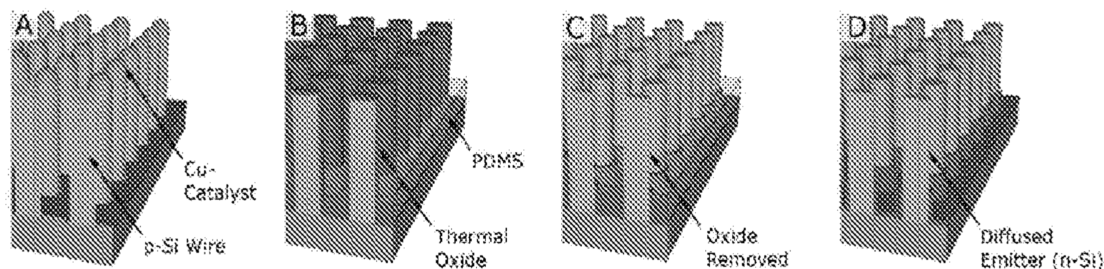

Fig. 1. Schematic of the radial pn-junction fabrication process. (*A*) As-grown p-Si microwire array. (*B*) Microwire array after catalyst removal, growth of a thermal oxide and deposition of a PDMS layer. (*C*)

Etching in a hydrofluoric acid solution removes the unprotected thermal oxide. (*D*) PDMS is removed and a phosphorous diffusion is performed to complete the fabrication of a radial pn-junction.

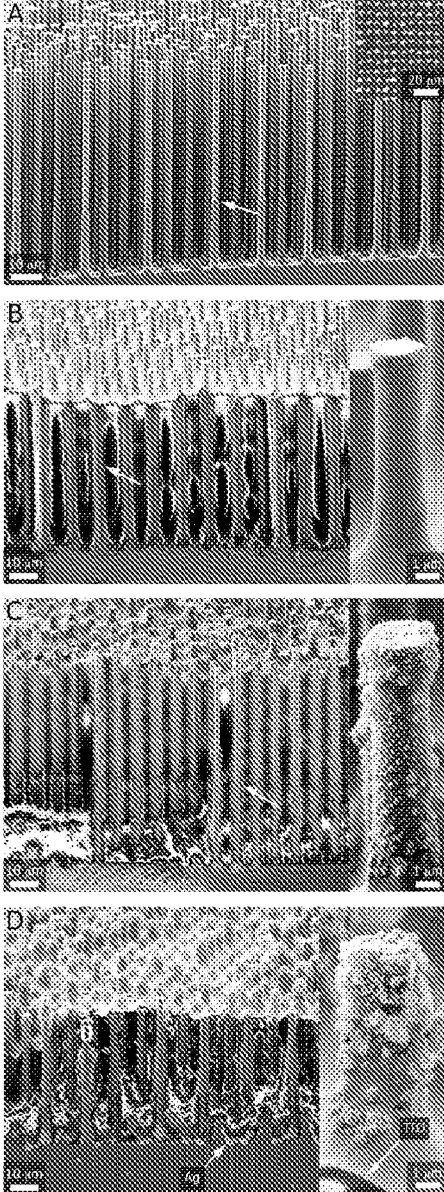

Fig. 2. Si microwire array solar cell device geometry. (*A*) Cross-sectional scanning electron microscope (SEM) image of a Si microwire array after radial pn-junction formation. The white arrow denotes the height of the thermal oxide (used as a phosphorous diffusion barrier in the radial pn-junction fabrication process.) *Inset*, top-down SEM image of the same Si microwire array illustrating the pattern fidelity and

slight variation in wire diameter. Cross-sectional SEM image of (*B*) as-grown solar cell, (*C*) scatter solar cell, and (*D*) PRS solar cell. *Insets,* higher magnification SEM images of the wire tips coated with ITO. For (*B*)-(*C*) the white arrow again denotes the height of the thermal oxide. For (*D*) the white arrow denotes the presence of the Ag back reflector. For the inset of (*D*) the white arrow denotes the ITO layer.

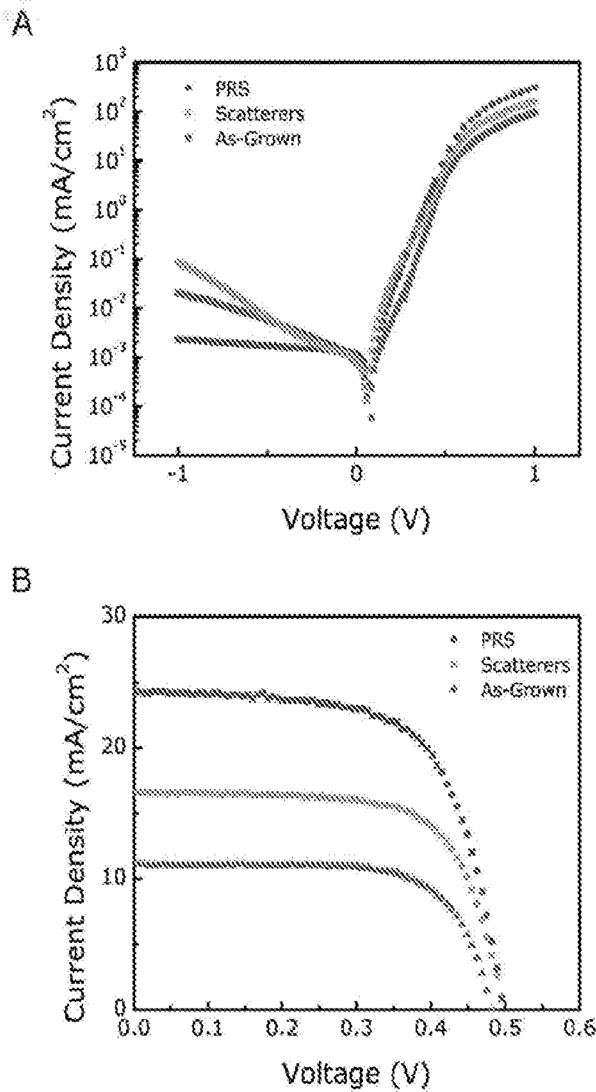

Fig. 3. Current density as a function of voltage for microwire solar cells (*A*) in the dark and (*B*) and under simulated AM 1.5G illumination.

Table 1:

Sample	V_{oc} (mV)	J_{sc} (mA/cm2)	*FF* (%)	η (%)
As-Grown C2R3	**482**	**11.2**	**69.4**	**3.75**
As-Grown C4R6	478	11.0-15.5*	59.1	3.1-4.4*
Scatterer C2R4	**499**	**16.6**	**68.0**	**5.64**
Scatterer C3R3	504	15.2	68.8	5.28
PRS C2R5	503	22.2	66.1	7.38
PRS C3R5	500	22.8	67.2	7.65
PRS C4R5	**498**	**24.3**	**65.4**	**7.92**

*The numbers shown reflect bounds on the active area of as-grown C4R6 at the time of IV characterization. See supporting information for a further discussion.

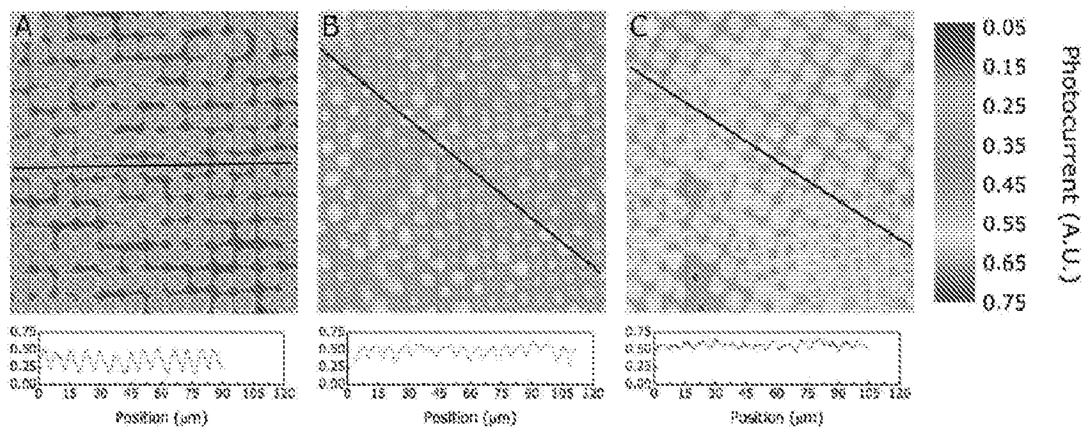

Fig. 4. Two-dimensional photocurrent maps (90 μm x 90 μm) and associated photocurrent line profiles from the center of (*A*) an as-grown solar cell, (*B*) a scatterer solar cell, and (*C*) a PRS solar cell. The black lines on each photocurrent map denote the cross-section used to produce the associated photocurrent line profiles.

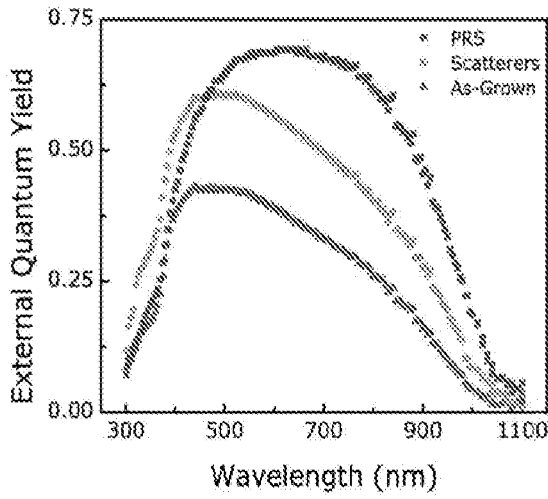

Fig. 5. External quantum yield for the champion Si microwire solar cells from 300 nm to the 1100 nm.

References:

[1] M. D. Kelzenberg, S. W. Boettcher, J. A. Petykiewicz et al., "Enhanced absorption and carrier collection in Si
wire arrays for photovoltaic applications," 239-244 Nat. Mater. **9** (2010).

[2] B. M. Kayes, H. A. Atwater, and N. S. Lewis, "Comparison of the device physics principles of planar and radial p-n junction nanorod solar cells," J. Appl. Phys. **97** (11), 114302-114311 (2005).

[3] B. M. Kayes, M. A. Filler, M. C. Putnam et al., "Growth of vertically aligned Si wire arrays over large areas (> 1 cm^2) with Au and Cu catalysts," Appl. Phys. Lett. **91** (10), 103110-103113 (2007).

[4] K. E. Plass, M. A. Filler, J. M. Spurgeon et al., "Flexible Polymer-Embedded Si Wire Arrays," Adv. Mater. **21** (3), 325-328 (2009).

[5] J. M. Spurgeon, K. E. Plass, B. M. Kayes et al., "Repeated epitaxial growth and transfer of arrays of patterned, vertically aligned, crystalline Si wires from a single Si(111) substrate," Appl. Phys. Lett. **93** (3) (2008).

[6] M. D. Kelzenberg, M. C. Putnam, D. B. Turner-Evans et al., in *34th IEEE PVSC* (Philadelphia, PA, 2009).

[7] J. R. Maiolo, B. M. Kayes, M. A. Filler et al., "High aspect ratio silicon wire array photoelectrochemical cells," Journal of the American Chemical Society **129** (41), 12346-12347 (2007).

[8] A. P. Goodey, S. M. Eichfeld, K. K. Lew et al., "Silicon nanowire array photoelectrochemical cells," Journal of the American Chemical Society **129**, 12344-12345 (2007).

[9] L. Tsakalakos, J. Balch, J. Fronheiser et al., "Silicon nanowire solar cells," Appl. Phys. Lett. **91** (23), 233117-233113 (2007).

[10] B. Z. Tian, X. L. Zheng, T. J. Kempa et al., "Coaxial silicon nanowires as solar cells and nanoelectronic power sources," Nature **449** (7164), 885-889 (2007).

[11] M. D. Kelzenberg, D. B. Turner-Evans, B. M. Kayes et al., "Photovoltaic measurements in single-nanowire silicon solar cells," Nano Lett. **8** (2), 710-714 (2008).

[12] O. Gunawan and S. Guha, "Characteristics of vapor-liquid-solid grown silicon nanowire solar cells," Solar Energy Materials and Solar Cells **93** (8), 1388-1393 (2009).

[13] T. J. Kempa, B. Z. Tian, D. R. Kim et al., "Single and Tandem Axial p-i-n Nanowire Photovoltaic Devices," Nano Lett. **8** (10), 3456-3460 (2008).

[14] K. Q. Peng, Y. Xu, Y. Wu et al., "Aligned single-crystalline Si nanowire arrays for photovoltaic applications," Small **1** (11), 1062-1067 (2005).

[15] E. C. Garnett and P. Yang, "Light Trapping in Silicon Nanowire Solar Cells," Nano Lett. (2010).

[16] T. Stelzner, M. Pietsch, G. Andra et al., "Silicon nanowire-based solar cells," Nanotechnology **19** (29) (2008).

[17] E. C. Garnett and P. D. Yang, "Silicon nanowire radial p-n junction solar cells," Journal of the American Chemical Society **130** (29), 9224-+ (2008).

[18] C. Colombo, M. Heiss, M. Gratzel et al., "Gallium arsenide p-i-n radial structures for photovoltaic applications," Appl. Phys. Lett. **94** (17) (2009).

[19] Y. J. Dong, B. Z. Tian, T. J. Kempa et al., "Coaxial Group III-Nitride Nanowire Photovoltaics," Nano Lett. **9** (5), 2183-2187 (2009).

[20] H. Goto, K. Nosaki, K. Tomioka et al., "Growth of Core-Shell InP Nanowires for Photovoltaic Application by Selective-Area Metal Organic Vapor Phase Epitaxy," Applied Physics Express **2** (3) (2009).

[21] M. C. Putnam, M. A. Filler, B. M. Kayes et al., "Secondary Ion Mass Spectrometry of Vapor-Liquid-Solid Grown, Au-Catalyzed, Si Wires," Nano Lett. **8** (10), 3109-3113 (2008).

[22] M. C. Putnam, D. B. Turner-Evans, M. D. Kelzenberg et al., "10 μm Minority-Carrier Diffusion Lengths in Si Wires Synthesized
by Cu-Catalyzed Vapor-Liquid-Solid Growth," Appl. Phys. Lett. **In Review** (2009).

[23] S. W. Boettcher, J. M. Spurgeon, M. C. Putnam et al., "Energy-Conversion Properties of Vapor-Liquid-Solid-Grown Silicon Wire-Array Photocathodes," Science **327** (5962), 185-187.

[24] M. D. Kelzenberg, D. B. Turner-Evans, M. C. Putnam et al., (2010).

[25] S. Takayama, E. Ostuni, X. Qian et al., "Topographical Micropatterning of Poly(dimethylsiloxane) Using Laminar Flows of Liquids in Capillaries," Adv. Mater. **13** (8), 570-574 (2001).

APPENDIX 3

Enhanced absorption and carrier collection in Si wire arrays for photovoltaic applications

Si wire arrays are a promising architecture for solar-energy-harvesting applications, and may offer a mechanically flexible alternative to Si wafers for photovoltaics[1-17]. To achieve competitive conversion efficiencies, the wires must absorb sunlight over a broad range of wavelengths and incidence angles, despite occupying only a modest fraction of the array's volume. Here, we show that arrays having less than 5% areal fraction of wires can achieve up to 96% peak absorption, and that they can absorb up to 85% of day-integrated, above-bandgap direct sunlight. In fact, these arrays show enhanced near-infrared absorption, which allows their overall sunlight absorption to exceed the ray-optics light-trapping absorption limit[18] for an equivalent volume of randomly textured planar Si, over a broad range of incidence angles. We furthermore demonstrate that the light absorbed by Si wire arrays can be collected with a peak external quantum efficiency of 0.89, and that they show broadband, near-unity internal quantum efficiency for carrier collection through a radial semiconductor/liquid junction at the surface of each wire. The observed absorption enhancement and collection efficiency enable a cell geometry that not only uses 1/100th the material of traditional wafer-based devices, but also may offer increased photovoltaic efficiency owing to an effective optical concentration of up to 20 times.

Arrays of Si wires with radial p–n junctions are being explored as an alternative to wafer-based Si geometries for photovoltaic applications[1-6]. The radial collection geometry can, in principle, tolerate the use of low-purity Si with a short minority carrier diffusion length, while allowing for high solar-energy-conversion efficiencies, by providing a short minority carrier collection path equal to the wire radius. Large-area arrays of Si wires can be grown on commonly available (for example, glass[4,5]) or re-usable[17] substrates using the vapour–liquid–solid (VLS) growth process[19]. Oriented horizontally, single-nanowire solar cells grown by the VLS process have demonstrated up to 3.4% conversion efficiency[7]. Si nanowire arrays have also been shown to have beneficial optical absorption properties for photovoltaic applications, owing to the subwavelength scale of the wires[8-12].

Obtaining optimal solar-energy-conversion efficiencies for macroscopic wire-array devices, however, requires not only that the wire array provide effective absorption of the photons incident onto the entire device—at a variety of wavelengths and angles of incidence—but also that the wires be optimally sized for efficient carrier collection. A theoretical treatment of radial p–n junctions[1] predicts optimal efficiency for wires that have a diameter of the order of the minority-carrier diffusion length, which is

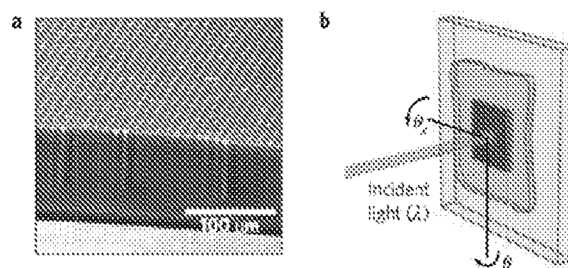

Figure 1 | Structure of Si wire arrays prepared for optical measurements. **a**, SEM image of a peeled-off, polymer-embedded wire array, viewed upside-down (at 60° tilt) to illustrate the order and fidelity of the embedded wires. **b**, Schematic of the illumination conditions and definition of the incidence angles θ_x and θ_y.

2–10 μm for our VLS-grown Si wires[20,21]. On the basis of these diffusion lengths, micrometre-scale-diameter single-wire solar cells have been predicted to achieve over 17% conversion efficiency[22]. This framework motivates the study of the optical absorption of Si microwire arrays, as these structures will interact with light differently from the subwavelength structures previously studied. We report herein the design, implementation and demonstration of Si microwire-array devices that show, over macroscopic device areas, effective incident light absorption as well as efficient charge-carrier collection.

To study the optical absorption of Si wire arrays independently from the optical effects of the growth substrate, the arrays were grown by a photolithographically patterned VLS process[23], then embedded in the transparent polymer polydimethylsiloxane (PDMS) and peeled intact from the growth wafer as flexible films[16] (Fig. 1a). These films were well suited for optical transmission and reflection measurements, which were carried out using an integrating sphere, as a function of wavelength and incidence angle (Fig. 1b). Numerous high-fidelity arrays of varying wire length, diameter, spacing and tiling patterns (including periodic, quasi-periodic and random motifs) were investigated in this fashion. The areal wire packing fractions, η_f, ranged from 1.6 to 16%. Figure 2 shows an example wire array of each of the seven investigated tiling patterns (top rows). Following peel-off, the transmitted optical diffraction patterns (third row) were used to orient the wire lattice patterns relative to the tilt directions (θ_x, θ_y), and angularly resolved transmission measurements were carried out (bottom row).

Owing to the vertical orientation of the wires, all of the arrays showed lower absorption at normal incidence ($\theta_{x,y} = 0°$) than at other angles. The well-aligned rows and columns of

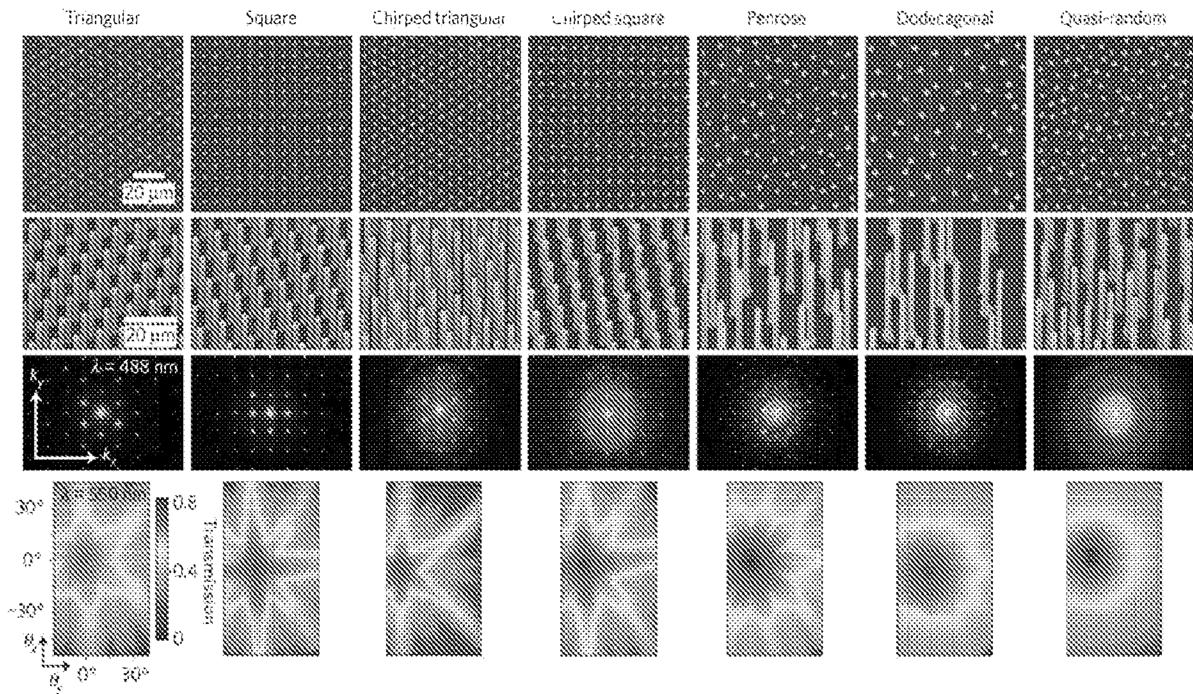

Figure 2 | Representative composition and optical properties of each wire-array tiling pattern. The scale bars in the left column apply to all images across each row. Top row: SEM images of as-grown wire arrays viewed from a top-down perspective. Second row: SEM images viewed at a 20° angle. Third row: Transmitted diffraction patterns of polymer-embedded wire arrays on a quartz slide, observed at $\lambda = 488$ nm. The axes indicate 4,000 cm^{-1} in the direction of k_x and k_y. Bottom row: Integrated transmission of each wire array observed at $\lambda = 550$ nm as a function of the beam incidence angle (θ_x, θ_y).

wires produced by periodic arrangements led to greater areal packing fractions (and thus higher overall optical absorption) than were obtained by quasi-periodic or random arrangements. However, the periodic arrangements also showed a strongly anisotropic angular absorption profile, which would produce low-absorbing 'dead spots' in a photovoltaic device. Alteration of the VLS catalyst template pattern to produce mild randomization (chirping) of the wire position within the periodic arrays was not sufficient to eliminate the obvious optical absorption minima at certain angles of incidence. Furthermore, increasing the areal packing fraction of the wire arrays to $\eta_f > 12\%$ increased their reflectivity, presumably because of the increasing area of the reflective Si/PDMS dielectric interface at the top of each wire, which in turn reduced their overall absorption (see Supplementary Information). These observations suggested that, for Si wire arrays to achieve maximal absorption over the relevant wavelengths and incidence angles of solar illumination, the reflectivity of the Si surfaces must be reduced, and the light passing between the wires must be randomized.

Figure 3 demonstrates the light-trapping techniques that were used to maximize the absorption of a square-tiled array of 67-μm-long Si wires. With an areal packing fraction of $\eta_f = 4.2\%$, this array contained the same volume of Si as a 2.8-μm-thick planar sheet of Si. As expected, the peak absorption was relatively low at normal incidence (<0.5) and increased at steeper angles of incidence (Fig. 3a). The wire array was then placed on a mirror-like Ag back-reflector (Fig. 3b), to emulate a metal back contact to a prototypical wire-array solar cell, as well as to increase the optical path length within the array. Although this step substantially increased the absorption of the array (approaching peak normal-incidence values of 0.8), the normal-incidence absorption remained significantly weaker than that at off-normal-incidence angles. To further improve absorption, two more light-trapping measures were implemented on a different portion of the wire array. Before being embedded in PDMS, a SiN_x antireflective coating (80 nm nominal thickness) was conformally deposited onto the tops and sides of these wires (Supplementary Fig. S1). In addition, Al_2O_3 particles (0.9 μm nominal diameter) were added to the PDMS infill, to scatter the light that might otherwise pass between the wires (Supplementary Fig. S3). These materials were chosen because they have negligible absorption across the wavelengths studied here (Supplementary Figs S2,S4), and thus enabled the direct observation of absorption enhancement within the Si wires themselves. As shown in Fig. 3c, these light-trapping measures virtually eliminated the angular sensitivity of the wire array's absorption, and increased the peak normal-incidence absorption to 0.92. When placed on a Ag back-reflector, the array's peak absorption increased to 0.96 (Fig. 3d), which is nearly the maximal absorption achievable by any material fully embedded within PDMS (owing to the ~3% reflectivity of the PDMS–air dielectric interface.)

To provide a figure of merit for the absorption measurements, the overall fraction of above-bandgap photons that each wire array would absorb throughout a day of operation as a non-tracking solar cell, A_{avg}, was calculated on the basis of a time-resolved reference spectrum of direct solar insolation[24] in conjunction with the measured angle- and wavelength-dependent absorption values of the wire arrays (Supplementary Fig. S10). Figure 3e shows the A_{avg} calculations that correspond to the absorption measurements shown in Fig. 3a–d. Also shown, for comparison, is the A_{avg} calculation that corresponds to the measured absorption of a commercial, 280-μm-thick polycrystalline Si solar cell with a dielectric antireflective coating. The optimal Si wire array showed $A_{avg} = 0.85$, which although slightly below that of the commercial Si solar cell ($A_{avg} = 0.87$), is remarkable considering that this wire-array film contained ~1% as much Si (per specimen area) as the commercial solar cell. This volume reduction implies substantial optical concentration within the Si wires.

To further gauge the absorption enhancement of the wire-array geometry, the measured absorption, $A_{WA}(\theta_i, \lambda)$, of the optimal wire array from Fig. 3d was compared with the theoretical absorption limits of a 2.8 μm planar Si absorber, which contains the same average volume of Si per unit area as the wire array (Fig. 4). On the basis of bulk Si properties[25] and neglecting interference

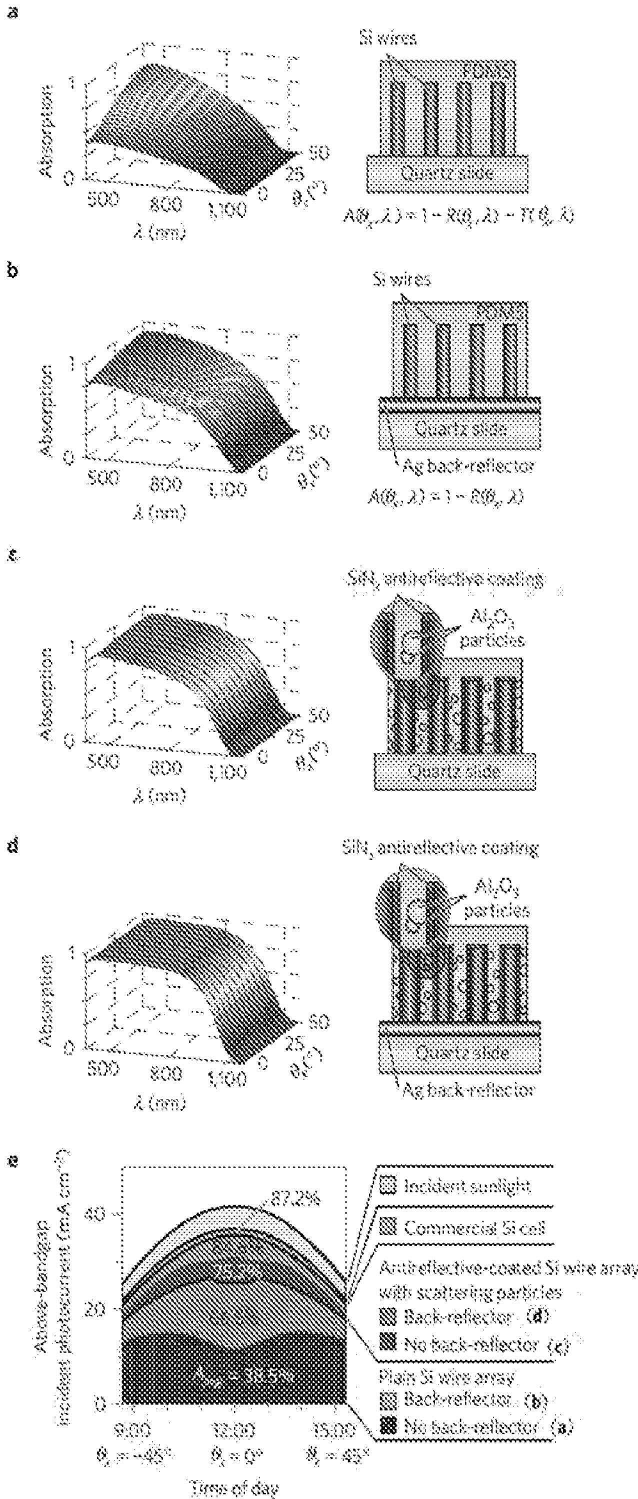

Figure 3 | Light-trapping techniques and figure of merit (A_{avg}) calculation. a,b, Schematic and measured absorption of a η_f = 4.2% square-tiled wire array on a quartz slide (**a**) and on a Ag back-reflector (**b**). **c,d**, Schematic and measured absorption of this array with an antireflective coating and embedded light-scatterers, measured on a quartz slide (**c**) and on a Ag back-reflector (**d**). **e**, A plot of A_{avg} calculations corresponding to each absorption measurement shown in **a**–**d**, showing the incident sunlight and spectrally weighted absorption of each throughout the day, compared with the measured absorption of a commercial, antireflective-coated, polycrystalline Si solar cell.

effects, two theoretical absorption limits were calculated for the equivalently thick Si slab: A_{Si}, which results from the use of bare, non-textured Si surfaces (black), and A_{LT}, which results from ideal classical light-trapping at the Si surfaces (blue). The latter case,

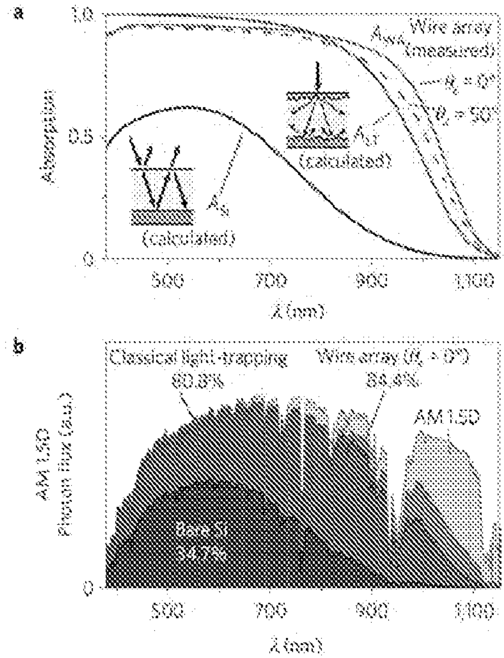

Figure 4 | Measured Si wire-array absorption versus theoretical absorption of an equivalently thick, planar Si absorber. a, Measured absorption (A_{WA}, red) of the Si wire array from Fig. 3d (which had an equivalent planar Si thickness of 2.8 µm), at normal (solid) and 50° (dashed) incidence, versus the calculated normal-incidence absorption of a 2.8-µm-thick planar Si absorber, with an ideal back-reflector, assuming: bare, non-texturized surfaces (A_{Si}, black) and ideally light-trapping, randomly textured surfaces (A_{LT}, blue). **b**, Illustration of the normal-incidence, spectrally weighted absorption of the AM 1.5D reference spectrum, corresponding to each of the three absorption cases plotted above.

the 'ergodic limit', is the maximally achievable absorption (in the ray-optic limit) of a planar-sheet absorber that uses ideally random (for example, Lambertian) light-trapping[18,26].

As shown in Fig. 4a, the wire array's absorption exceeded the planar light-trapping limit for infrared wavelengths (λ > 800 nm). This behaviour exemplifies a useful property of microstructured, non-planar absorber geometries (including wire arrays), in that they can achieve greater absorption per material volume than achievable by a randomly textured, planar-sheet absorber geometry. This effect has been described, through use of a statistical ray optics model, for idealized films of polymer-embedded Si granules[30], and has also been simulated for Si wire arrays[5,9]. Figure 4b shows, using the AM 1.5D spectrum at normal incidence, that the enhanced infrared absorption of the Si wire array yielded a greater overall absorption of above-bandgap photons than the equivalently thick, ideally light-trapping planar absorber. In fact, taking all measured incidence angles into account, the day-integrated absorption of the wire array (A_{avg} = 0.85) slightly exceeded that of the planar light-trapping case (A_{avg} = 0.82). Thus, the Si wire-array geometry can enable solar cells that reach, and potentially even exceed, the theoretical absorption limit, per volume of Si, of ideal light-trapping within a conventional planar geometry.

The enhanced absorption properties of Si wire arrays enable high quantum efficiencies for photovoltaic applications. To demonstrate this, a photoelectrochemical cell (Fig. 5a) was used to measure the external quantum efficiency (EQE) of Si wire-array photoelectrodes, which consisted of p-type wire arrays grown on degenerately doped (and thus photovoltaically inactive, see Supplementary Fig. S15) Si wafers. The transparent electrolyte formed a rectifying junction to the top and sides of each wire (analogous to a radial p–n junction[27]), enabling photoelectrochemical characterization of the

angle- and wavelength-dependent EQE of the wire-array electrode. However, because the wires were immersed in an electrolyte and attached to their growth substrate, this technique did not permit the use of a polymer infill, a dielectric antireflective coating and/or a planar metal back-reflector. Thus, relatively long (130 μm) and sparse ($\eta_f = 6.2\%$) square-tiled wire arrays were grown, to minimize the transmission of light into the photovoltaically inactive growth substrate while also minimizing the area of the reflective top surface of the Si wires (Fig. 5b, upper left). This geometry yielded up to 0.85 peak EQE (lower left), but suffered from substantially reduced EQE at normal incidence (centre left). Evaluating the EQE across the day-integrated solar spectrum (as carried out for A_{avg} above) yielded $EQE_{avg} = 0.56$ (Supplementary Fig. S19). When Al_2O_3 light-scattering particles were drop-cast into this wire array (Fig. 5b, upper right), the normal-incidence 'dead spot' was virtually eliminated (centre right), the peak EQE increased to 0.89 (lower right) and the day-integrated EQE_{avg} increased to 0.68. This value is significant, considering that the photoelectrochemical cell configuration precluded the use of a metal back-reflector or an antireflective coating, both of which are known to substantially improve the optical absorption (Fig. 3), and both of which could be used within a solid-state, radial p–n junction wire-array solar cell. Thus, the results presented here represent lower bounds, rather than upper limits, on the EQE that could be achieved by use of the Si wire-array geometry.

A particular concern for photovoltaic applications of VLS-grown wire arrays is the possibility of parasitic absorption, which could be caused by the presence of surface states, impurities or residual VLS catalyst metal deposits[28]. To determine the extent of useful (that is, non-parasitic) absorption, the internal quantum efficiency (IQE) of the Si wire-array electrodes was determined by normalizing their measured EQE to their measured absorption. To mitigate difficulties in peeling the Al_2O_3 particles intact with the array described above, this measurement was carried out on less-densely packed ($\eta_f = 3.0\%$) arrays of shorter (90 μm) wires without light-scatterers (Fig. 5c, inset). Figure 5c compares the measured normal-incidence EQE of this wire-array electrode (blue) to the measured normal-incidence absorption of the wires after being polymer-embedded and peeled from the growth substrate (black). Owing to the similarity between these illumination conditions (for example, the similar refractive indices of the surrounding PDMS/electrolyte solution, see Supplementary Information), this comparison was used to determine the approximate IQE of the wire-array electrode (red). The IQE exceeded 0.9 for most above-bandgap photon energies ($\lambda = 400$–900 nm), in good agreement with radial junction theory, which predicts a near-unity IQE for any wire having a radius of less than the minority carrier diffusion length[15]. Although the reported IQE decreased for $\lambda > 900$ nm, the measured absorption nevertheless differed from the measured EQE by no more than 0.05 throughout the entire measurement range, confirming that the absorption was predominately non-parasitic, while also providing a compelling demonstration of the broadband, near-unity IQE expected for a radial-junction, Si wire-array photovoltaic device.

The observed absorption enhancement and collection efficiency suggest that Si wire-array solar cells can benefit from the well-known improvements in open-circuit voltage (and thus photovoltaic efficiency) that are achievable under optical concentration[29]. When sunlight illuminates a wire array, the absorption is laterally confined within the relatively small cross-sectional area of the wires. In this regard, the $\eta_f = 4.2\%$ wire array that showed $A_{avg} = 0.85$ can be considered, to first order, as a ×24 lateral geometric concentrator that achieved a ×20 average intensity concentration without the use of conventional focusing optics. Several theoretical studies have discussed the enhanced photogeneration rates in wire-array absorbers[5,8,30].

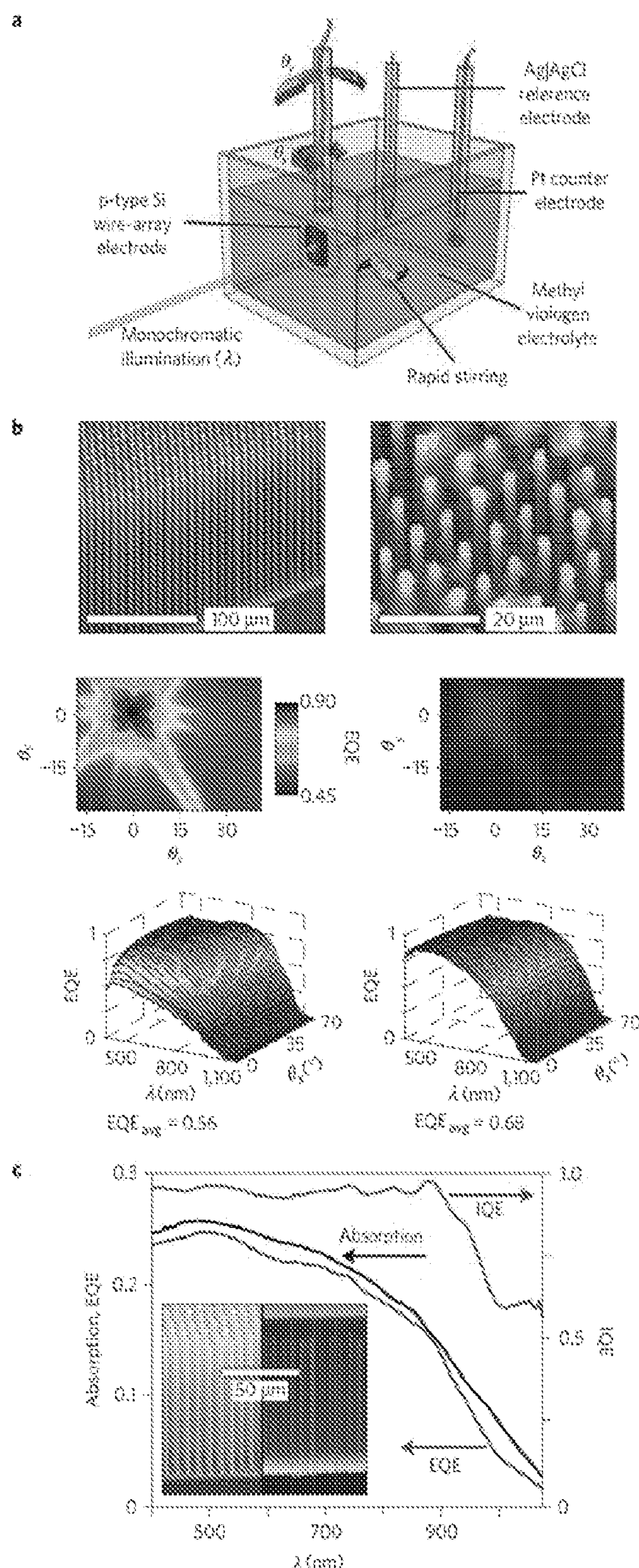

Figure 5 | Photoelectrochemical characterization of Si wire arrays. **a**, Schematic of the photoelectrochemical cell and definition of illumination angles. **b**, Effect of light-scattering particles on wire-array electrode EQE. Top: SEM image; centre: two-dimensional angle-resolved EQE at $\lambda = 550$ nm; bottom: wavelength-angle-resolved EQE at $\theta_y = 0°$, of a Si wire-array electrode without (left) and with (right) Al_2O_3 light-scattering particles. **c**, Normal-incidence absorption measurement of a polymer-embedded wire array (black) and normal-incidence EQE of a wire-array electrode (blue). A 50 nm running average was applied to the absorption, to reduce interference fringes in the experimental data. The resulting IQE is plotted in red. Inset: SEM images of the wire-array electrode (left) and the polymer-embedded wire array (right).

We have experimentally demonstrated that Si wire arrays have advantageous optical properties for photovoltaic applications, including reasonable absorption of sunlight despite low areal packing fractions, extended near-infrared absorption compared with planar-sheet absorbers and effective optical concentration over a wide range of incidence angles. We note that the observations reported herein are not limited to Si wire-array solar cells. The wire-array geometry, along with other microstructured, non-planar absorber geometries (for example, the microcell geometry[31] or CdS/CdTe nanopillars[32]), offers opportunities to manipulate the ratio of illumination area to absorption volume, and may be useful in improving the efficiency or reducing the materials consumption of many photovoltaic technologies.

Methods

Wire-array fabrication. Si wire arrays were grown by a photolithographically patterned VLS process as described previously[33]. Wires were grown on p-type (111) Si wafers ($\rho < 0.001$ Ω cm), using a 300 nm thermal oxide for catalyst confinement and evaporated Au, Cu or Ni (400–700 nm thickness) as the VLS catalyst. No notable differences were observed between the optical properties of wires grown using Au, Cu or Ni catalyst metal. Following growth, the wire arrays were etched in 5% HF(aq) for 30 s. To remove the catalyst metal, Au-catalysed wires were then etched for 30 min in a solution of 9:1 Gold Etchant TFA (Transene) to 36% HCl(aq) and then rinsed for 30 s in 5% $HCl_{(aq)}$. Cu- and Ni-catalysed wires were instead etched for 20 min at 70 °C in a 6:1:1 solution of $H_2O/H_2O_2/HCl$. Both groups of wires were then HF-etched as described above, dried and momentarily dipped in a 50% (wt) aqueous solution of KOH at 55 °C, to remove ~20 nm of Si, thus removing the metal-rich surface layer observed in similarly grown wires[33]. For the antireflective-coated structures, a SiN_x film of 80 nm nominal thickness was then conformally deposited onto the wire arrays by plasma-enhanced chemical vapour deposition at 350 °C (Supplementary Fig. S1).

The lengths, diameters and areal fractions of each wire array were determined by computer processing of high-resolution scanning electron microscope (SEM) images, taken from a 200 × 200 μm area at the centre of each array. Only near-perfect wire arrays, defined as those that had at most one defect within this area (for example, non-vertical or spurious growth or a wire missing from the pattern), were considered. Arrays were embedded in PDMS and peeled-off as previously described[16]. The PDMS was drop-cast, spun at 3,000 rpm and then cured at 120 °C for ≥1 h, resulting in a smooth film with an overall thickness that ranged from 10 to 50 μm greater than the height of the wire array. For arrays that incorporated Al_2O_3 light-scatterers, particles of 0.9 μm nominal diameter, the surfaces of which had been modified with trimethylchlorosilane, were dispersed into CH_2Cl_2 by sonication. This solution was mixed into the PDMS to yield a ratio of 1:10:10 Al_2O_3/CH_2Cl_2/PDMS by weight. The suspension was drop-cast, spun and cured as described above; however, before curing, the arrays were centrifuged for several minutes to drive the Al_2O_3 particles towards the bottom of the PDMS layer (Supplementary Fig. S3).

Optical measurements. The transmitted diffraction patterns were observed by illuminating several square millimetres of each wire array at normal incidence with a 488 nm Ar ion laser beam. A greyscale digital camera recorded the image produced on a screen positioned approximately 30 cm behind the wire array. The images were corrected for the tilt of the camera relative to the screen, and were falsely coloured to indicate the illumination wavelength.

Integrated reflection and transmission measurements were carried out with a custom-built, motorized integrating-sphere apparatus (Supplementary Fig. S5). A supercontinuum laser (Fianium) was coupled to a monochromator to provide a tunable (λ = 400–1,600 nm), collimated illumination beam, which was monitored by a reference photodiode. Before measurement, the diffraction pattern and specular reflection of each non-random wire array were used to align the orientation of the wire lattice relative to the axes of rotation (θ_x, θ_y), following the convention of Fig. 2. Transmission measurements were normalized to that of the uncovered area of the underlying quartz slide ($T \sim 0.92$), whereas reflection measurements were normalized to a reflectance standard (Labsphere) within the sphere.

Photoelectrochemical measurements. Cu-catalysed, square-tiled wire arrays with 7 μm pitch were grown as described above, with the exception that BCl_3 was present during the VLS growth, to produce wires with an estimated p-type doping of $\sim 5 \times 10^{17}$ cm^{-3}. Following growth, the wire arrays were etched in 10% $HF_{(aq)}$ for 10 s, then in 30% $FeCl_{3(aq)}$ for 30 min and finally in 20% $KOH_{(aq)}$ for 1 min at room temperature. Electrodes were fabricated from ~5 mm² portions of the wire arrays (Supplementary Fig. S16), using a GaIn eutectic to make ohmic contact to the back side of the growth wafer. Immediately before measurement, each electrode was etched in 5% $HF_{(aq)}$ for 10 s, then placed in the photoelectrochemical cell. The electrolyte contained 0.5 M $KCl_{(aq)}$ and 0.01 M aqueous methyl viologen redox couple at pH 1 (adjusted with HCl)[15]. The photoresponse of the wire-array electrodes was measured at a bias of −0.4 to −0.5 V versus a Ag|AgCl reference electrode (chosen to place the liquid junction near short-circuit conditions, see Supplementary Fig. S14), using a Pt coil as the counter electrode. The apparatus described above provided a referenced, chopped (f = 30 Hz) light beam and motorized articulation of the electrode within the cell. To determine the EQE, the photoresponse of each electrode was normalized to that of a calibrated Si photodiode that had been placed at the same position within the cell. Measurements were carried out in the dark (aside from the chopped illumination beam) and the cell was continuously stirred and purged with Ar. Light-scattering particles were added to the wire-array electrodes by dispersing 0.08-μm-nominal-diameter Al_2O_3 particles in ethanol, placing the wire-array electrode at the bottom of this solution and centrifuging until sufficient particle density was observed at the base of the wire array. The structures were lightly rinsed with isopropanol and water and then measured as described above. No substantial loss of the Al_2O_3 particles was observed during the course of these measurements.

To determine the IQE, a wire array of nominally identical geometry to the electrode shown in Fig. 5c (inset left), which originated from the same growth and processing, was prepared and peeled-off for optical measurements as described above (Fig. 5c, inset right). The reflectivity of the recovered Si growth wafer was measured, to determine its maximal effectiveness as a back-reflector beneath the wire-array electrode (Supplementary Fig. S16). The EQE of this recovered growth wafer was also measured, by using it as an electrode in the same photoelectrochemical cell, to confirm that it was photovoltaically inactive (Supplementary Fig. S15). The optical absorption of the polymer-embedded wire array, placed on a quartz slide, was then measured to determine the approximate IQE of the wire-array electrode.

Received 4 September 2009; accepted 14 January 2010; published online 14 February 2010; corrected online 19 February 2010

References

1. Kayes, B. M., Atwater, H. A. & Lewis, N. S. Comparison of the device physics principles of planar and radial p–n junction nanorod solar cells. *J. Appl. Phys.* 97, 114302–114311 (2005).
2. Garnett, E. C. & Yang, P. Silicon nanowire radial p–n junction solar cells. *J. Am. Chem. Soc.* **130**, 9224–9225 (2008).
3. Kelzenberg, M. D., Putnam, M. C., Turner-Evans, D. B., Lewis, N. S. & Atwater, H. A. *Proc. 34th IEEE Photovoltaic Specialists Conference* 1–6 (IEEE, 2009).
4. Tsakalakos, L. *et al.* Silicon nanowire solar cells. *Appl. Phys. Lett.* **91**, 233117 (2007).
5. Stelzner, T. *et al.* Silicon nanowire-based solar cells. *Nanotechnology* **19**, 295203 (2008).
6. Gunawan, O. & Guha, S. Characteristics of vapor–liquid–solid grown silicon nanowire solar cells. *Sol. Energy Mater. Sol. Cells* **93**, 1388–1393 (2009).
7. Peng, K. *et al.* Aligned single-crystalline Si nanowire arrays for photovoltaic applications. *Small* **1**, 1062–1067 (2005).
8. Sivakov, V. *et al.* Silicon nanowire-based solar cells on glass: Synthesis, optical properties, and cell parameters. *Nano Lett.* **9**, 1549–1554 (2009).
9. Altermatt, P. P., Yang, Y., Langer, T., Schenk, A. & Brendel, R. *Proc. 34th IEEE Photovoltaic Specialists Conference* 1–6 (IEEE, 2009).
10. Hu, L. & Chen, G. Analysis of optical absorption in silicon nanowire arrays for photovoltaic applications. *Nano Lett.* **7**, 3249–3252 (2007).
11. Muskens, O. L., Rivas, J. G. m., Algra, R. E., Bakkers, E. P. A. M. & Lagendijk, A. Design of light scattering in nanowire materials for photovoltaic applications. *Nano Lett.* **8**, 2638–2642 (2008).
12. Zhu, J. *et al.* Optical absorption enhancement in amorphous silicon nanowire and nanocone arrays. *Nano Lett.* **9**, 279–282 (2009).
13. Tian, B. *et al.* Coaxial silicon nanowires as solar cells and nanoelectronic power sources. *Nature* **449**, 885–889 (2007).
14. Goodey, A. P., Eichfeld, S. M., Lew, K.-K., Redwing, J. M. & Mallouk, T. E. Silicon nanowire array photoelectrochemical cells. *J. Am. Chem. Soc.* **129**, 12344–12345 (2007).
15. Maiolo, J. R. I. *et al.* High aspect ratio silicon wire array photoelectrochemical cells. *J. Am. Chem. Soc.* **129**, 12346–12347 (2007).
16. Plass, K. E. *et al.* Flexible polymer-embedded Si wire arrays. *Adv. Mater.* **21**, 325–328 (2009).
17. Spurgeon, J. M. *et al.* Repeated epitaxial growth and transfer of arrays of patterned, vertically aligned, crystalline Si wires from a single Si(111) substrate. *Appl. Phys. Lett.* **93**, 032112–032113 (2008).
18. Tiedje, T., Yablonovitch, E., Cody, G. D. & Brooks, B. G. Limiting efficiency of silicon solar-cells. *IEEE Trans. Electron Devices* **31**, 711–716 (1984).
19. Wagner, R. S. & Ellis, W. C. Vapor–liquid–solid mechanism of single crystal growth. *Appl. Phys. Lett.* **4**, 89–90 (1964).
20. Putnam, M. C. *et al.* 10 μm minority-carrier diffusion lengths in Si wires synthesized by Cu-catalyzed vapor–liquid–solid growth. *Appl. Phys. Lett.* **95**, 163116 (2009).
21. Kelzenberg, M. D. *et al.* Photovoltaic measurements in single-nanowire silicon solar cells. *Nano Lett.* **8**, 710–714 (2008).

22. Kelzenberg, M. D. et al. *Proc. 33rd IEEE Photovoltaic Specialists Conference* 1–6 (IEEE, 2008).
23. Kayes, B. M. et al. Growth of vertically aligned Si wire arrays over large areas (>1 cm^2) with Au and Cu catalysts. *Appl. Phys. Lett.* **91**, 103110–103113 (2007).
24. Marion, B. et al. Validation of a photovoltaic module energy ratings procedure at NREL. Report No. NREL/TP-520-26909 (1999).
25. Aspnes, D. E. in *Properties of Crystalline Silicon* (ed. Robert, H.) 683–690 (INSPEC, IEE, 1999).
26. Yablonovitch, E. Statistical ray optics. *J. Opt. Soc. Am.* **72**, 899–907 (1982).
27. Boettcher, S. W. et al. Energy-conversion properties of vapor–liquid–solid-grown silicon wire-array photocathodes. *Science* **327**, 185–187 (2010).
28. Tsakalakos, L. et al. Strong broadband optical absorption in silicon nanowire films. *J. Nanophoton.* **1**, 013552 (2007).
29. Campbell, P. & Green, M. A. The limiting efficiency of silicon solar cells under concentrated sunlight. *IEEE Trans. Electron Devices* **33**, 234–239 (1986).
30. Kupec, J. & Witzigmann, B. Dispersion, wave propagation and efficiency analysis of nanowire solar cells. *Opt. Express* **17**, 10399–10410 (2009).
31. Yoon, J. et al. Ultrathin silicon solar microcells for semitransparent, mechanically flexible and microconcentrator module designs. *Nature Mater.* **7**, 907–915 (2008).
32. Fan, Z. et al. Three-dimensional nanopillar-array photovoltaics on low-cost and flexible substrates. *Nature Mater.* **8**, 648–653 (2009).
33. Putnam, M. C. et al. Secondary ion mass spectrometry of vapor–liquid–solid grown, Au-catalyzed, Si wires. *Nano Lett.* **8**, 3109–3113 (2008).

Acknowledgements

This work was supported by BP and in part by the Department of Energy EFRC program under grant DE-SC0001293, and made use of facilities supported by the Center for Science and Engineering of Materials, an NSF Materials Research Science and Engineering Center at Caltech. S.W.B. acknowledges the Kavli Nanoscience Institute for fellowship support. The authors acknowledge D. Pacifici for useful discussions and assistance in generating the quasi-periodic hole-array patterns, B. Kayes and M. Filler for their contributions at the outset of this project and M. Roy and S. Olson for their advice and skill in machining the components of the experimental apparatus.

Author contributions

M.D.K. participated in the design and execution of the experiments, analysed the results and prepared the manuscript under the advisement of H.A.A. and the guidance of N.S.L. and S.W.B. J.A.P. contributed to the design and fabrication of the array template photomasks, the integrating-sphere apparatus and the image processing software. S.W.B., J.M.S., J.A.P., M.C.P. and D.B.T-E. assisted in the fabrication of the wire arrays and R.M.B. carried out the deposition and characterization of the SiN$_x$ antireflective coating. S.W.B., E.L.W. and J.M.S. assisted with the photoelectrochemical measurements and fabricated the electrodes. All authors discussed the results and commented on the manuscript.

Additional information

The authors declare no competing financial interests. Supplementary information accompanies this paper on www.nature.com/naturematerials. Reprints and permissions information is available online at http://npg.nature.com/reprintsandpermissions. Correspondence and requests for materials should be addressed to H.A.A.

Device fabrication

Silicon nitride deposition

Silicon nitride antireflective (AR) coatings were deposited onto Si wire arrays using an Oxford Instruments Plasmalab System100 plasma-enhanced chemical vapor deposition (PECVD) tool. Silane and ammonia gas chemistry was used at 350 °C and 1 torr, and the gas ratio was adjusted to produce films with a refractive index near 2. The PECVD process was performed with in-situ stress control by alternately pulsing a 13.56-MHz radio-frequency generator and a 50-kHz low-frequency generator, both with 20 W of forward power. Due to the large surface area and aspect ratio of the arrays, the coating required a much longer deposition time than would be required for a planar film of the same thickness.

The nitride final film thickness was measured by SEM, using focused-ion beam (FIB) milling to produce wire cross-sections (Fig. S1). Individual wires were removed from the growth substrate, and deposited (horizontally) onto a Si wafer that was coated with 80 nm SiN_x (for contrast reference). This was coated with various layers of metal (Ag, Al) to facilitate milling and imaging. The deposited nitride thickness was observed to increase gradually along the length of the wires, reaching ~2x the base thickness at the top sidewall of the wire, and ~2.5x the base thickness on the top surface of the wires (Fig. S1a). Thickness appeared uniform around the diameter of the wires (Fig. S1b). The nitride thickness of the actual wire array whose absorbance is plotted in Fig. 3 was verified by milling a cross section of a single wire within the center of the array, at approx. half the height of the adjacent wires (Fig. S1c).

Multiple-angle spectroscopic ellipsometry was used to measure the optical properties of a planar film of PECVD silicon nitride. Ψ and Δ spectra, ranging from 350–2200 nm, were measured at angles of 60°, 65°, and 70°, as shown in Fig. S2a. The spectra were then fit to a Forouhi-Bloomer model for amorphous dielectric materials.[1] The real and imaginary parts of the index produced by the fit are plotted in Fig. S2b. Based on these values, the absorption of an 80-nm nitride film is negligible (<2%) throughout most of the measurement range in this study (λ > 500 nm).

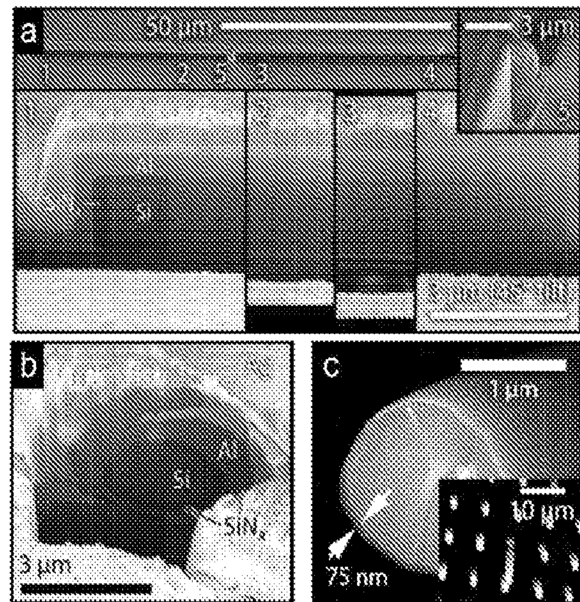

Figure S1. Determination of nitride thickness. a,b, cross-sectional SEM images of nitride-coated wires removed from growth substrate. Partial false-coloring added for clarity. **c,** cross-sectional SEM image of nitride-coated wire from center of wire array, with inset showing milling area.

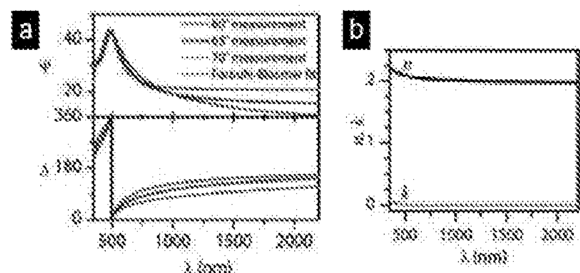

Figure S2. Spectroscopic ellipsometry characterization of silicon nitride film.

SUBSTITUTE SHEET (RULE 26)

Al_2O_3 light-scattering particles

Alumina particles were embedded within the PDMS infill of selected wire arrays, to scatter the light that might otherwise pass between the wires without being absorbed. Al_2O_3 particles (< 0.9 μm nominal particle size) were hydrophobicized via surface functionalization (> 1 hr in 10 μl/ml trimethylchlorosilane in CH_2CL_2). After washing several times to removed excess trimethylchlorosilane, the particles were suspended in CH_2CL_2 by sonication. This suspension was mixed with uncured PDMS to yield a ratio of 1:10:10 Al2O3:CH2Cl2:PDMS by weight. The suspension was drop cast onto the wire arrays and spun at speeds of 1500–3000 RPM (depending on device area). Prior to curing, the arrays were centrifuged for several minutes to drive the Al_2O_3 particles towards the bottom of the PDMS layer. Wire array films were cured and peeled-off as described in the *Methods* section.

Following characterization of the optical absorption, a wire array with the SiN_x AR-coating and embedded Al_2O_3 particles was sliced in half with a razor blade for cross-sectional imaging. Due to the insulating nature of the PDMS, an environmental SEM was employed, using H_2O vapor at 2–4 mbar to mitigate charging effects. Fig. S3a shows the cross-section of the wire array whose absorption is plotted in Fig. 3. Alumina particles were observed between the wires, distributed within the lower half of the PDMS film. Near the edge of this specimen, larger agglomerates of alumina particles were also observed above the top of the wire array (Fig. S3b), although these areas were not illuminated during optical measurements. Some wires were inadvertently severed during the cross-sectioning process, allowing the ~80 nm SiN_x AR-coating to be observed (Fig. S3b, inset).

The optical properties of the PDMS-embedded Al_2O_3 particles were also measured, to ensure that they did not contribute to parasitic absorption within the Si wire arrays. A drop of the PDMS with suspended Al_2O_3 particles was cured on a quartz slide without spinning or centrifuging, to yield a film thickness comparable to that of the wire arrays (est. 300 μm). The absorption of this film is shown in Fig. S4, indicating absorption was less than 2% throughout the spectral range of this study.

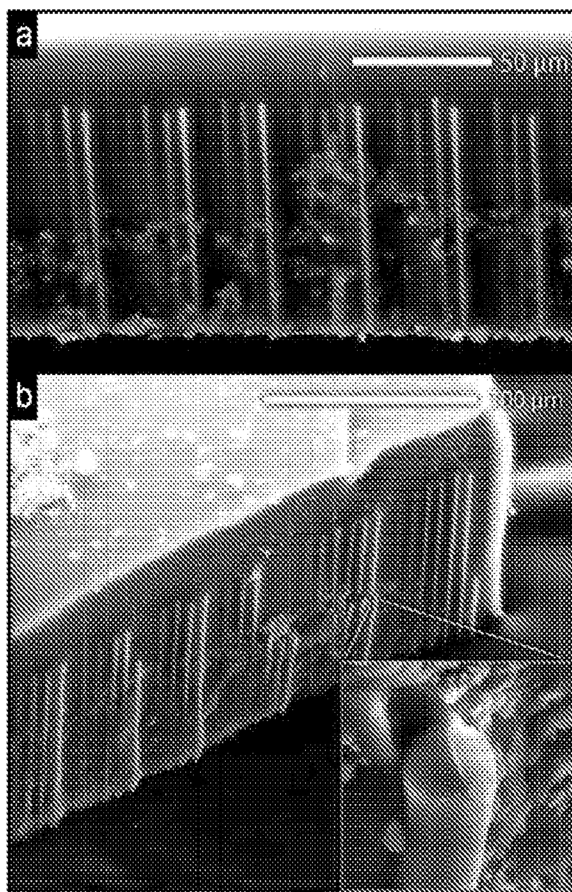

Figure S3. SEM images of the polymer-embedded Si wire array that was measured in Fig. 3. **a,** cross-section of central area of array showing distribution of Al_2O_3 particles. **b,** view of edge of array, with inset showing the ~80 nm SiN_x AR-coating visible on wire sidewall.

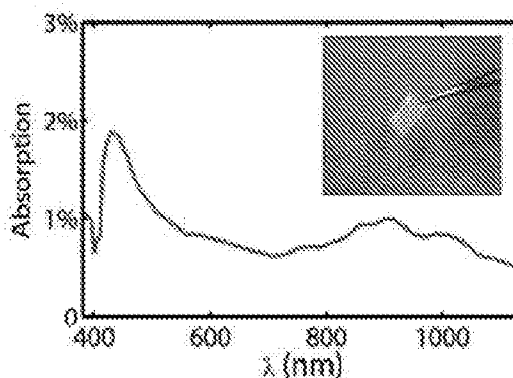

Figure S4. Integrated normal-incidence absorption of ~300 μm-thick film of Al_2O_3 particles embedded within PDMS. Inset: Digital photograph of this specimen.

Integrating sphere measurements

Experimental apparatus

Integrated reflection and transmission measurements were performed with a custom-built 4" integrating sphere apparatus, as shown in Figure S5. The internal surfaces of the sphere, baffles, port apertures, and stages were sandblasted, then cleaned and coated with a $BaSO_4$ integrating sphere coating (LabSphere, Inc) to achieve nearly ideal Lambertian reflectivity. Illumination was provided by a chopped supercontinuum laser source (Fianium) coupled to a 0.25 m monochromator, allowing tunable excitation from 400 nm to > 1600 nm with a typical passband of < 0.5 nm. The illumination beam was focused to produce a 1 mm spot size (FWHM) with < 0.1° of beam divergence. A pair of calibrated Si (400–1150 nm) or Ge (1000–1600 nm) photodiodes was used to simultaneously monitor the light intensity of the incident beam (referenced via a quartz beam-splitter) and the light intensity internal to the sphere. Measurements were typically performed from 400–1150 nm in 2 nm increments, except between 1058 and 1070 nm where the reported values were interpolated from measurements at either endpoint due to an unstable peak in the illumination intensity at 1064 nm.

In transmission mode, each specimen was placed over a 10 mm-diameter entrance port of the integrating sphere (Fig. S5a). Motorized operation permitted eucentric rotation and translation in two dimensions with 0.1° and 100 μm resolution, respectively. The wire array transmission was normalized to the previously measured transmission of the quartz slides which was accessed by motorized translation of the sphere at the beginning of the measurement sequence. In reflection mode, each specimen was placed at the center of the sphere over a 5 mm-diameter light trap that absorbed any light transmitted through the specimen (Fig. S5b). Motorized operation permitted eucentric rotation in one dimension (θ_x) with 0.1° resolution. The tilt in the second (θ_y) dimension was typically fixed at ~0.5°, to prevent the specular reflection from escaping the sphere through the 1 mm-diameter illumination port aperture. The wire array reflection was normalized to a

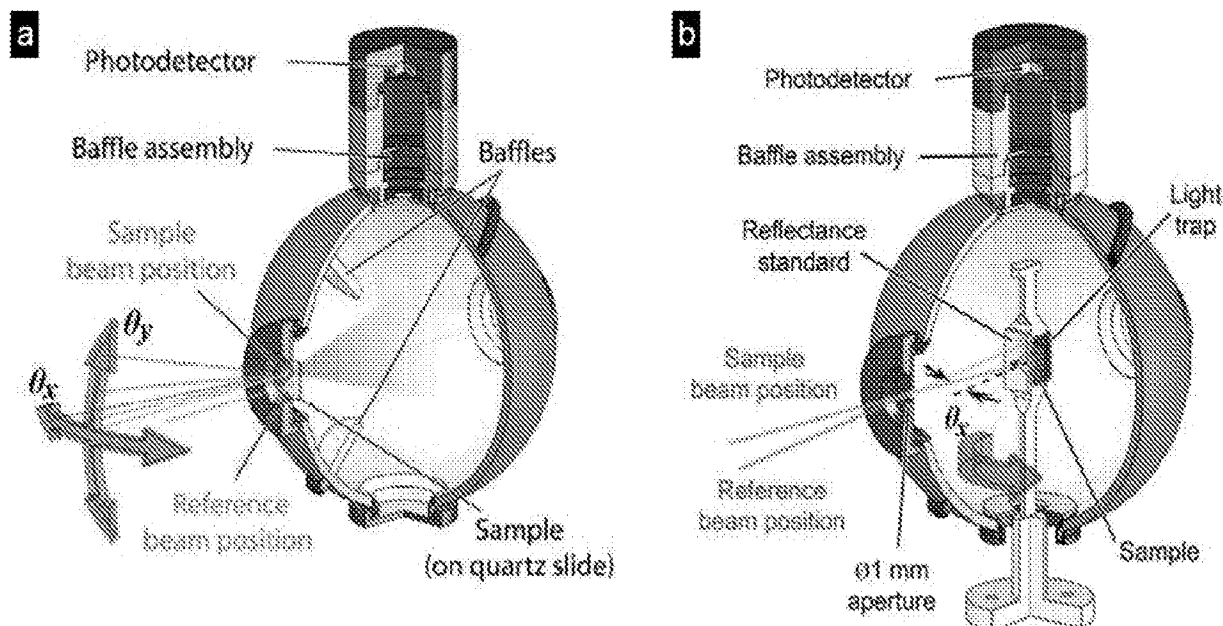

Figure S5. Illustration of integrating sphere measurements. a, configuration for transmission measurements. The incidence beam angle variation was achieved by the eucentric tilt of the entire sphere apparatus. **b,** configuration for reflection measurements. The incidence beam angle variation was achieved by rotation of the reflection stage within the sphere.

reflectance standard (LabSphere, Inc) within the sphere, which was accessed by motorized translation and rotation of the specimen stage and sphere assembly. For the measurements performed on specular back-reflectors, each wire array film was removed from the transparent quartz slide and placed onto a slide which had been coated with >100 nm of evaporated Ag. For the Lambertian back reflector studies, each wire array film was removed from the transparent quartz slide and placed onto a sheet of Al, that had been cleaned, roughened, and coated with $BaSO_4$ like the other internal surfaces of the integrating sphere. The reflectivity of such surfaces exceeded 97% throughout most of the measurement range (see Fig. S6).

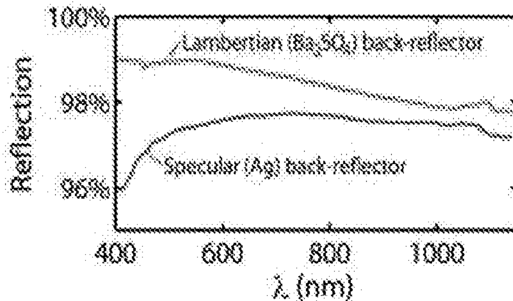

Figure S6. Integrated reflection measurements of the back-reflectors used in these studies.

Determination of absorption

The absorption of each specimen was determined from the wavelength- and angle-resolved integrated transmission and reflection measurements. For non-opaque specimens (e.g. wire arrays placed upon quartz slides), absorption was calculated as:

$$A(\lambda,\theta)=1-R(\lambda,\theta)-T(\lambda,\theta) \quad (1)$$

For opaque specimens (e.g. the commercial Si solar cell) or those placed on opaque back-reflectors, absorption was calculated from reflectivity measurements only:

$$A(\lambda,\theta)=1-R(\lambda,\theta) \quad (2)$$

Example transmission, reflection, and resulting absorption measurements of a triangular-tiled

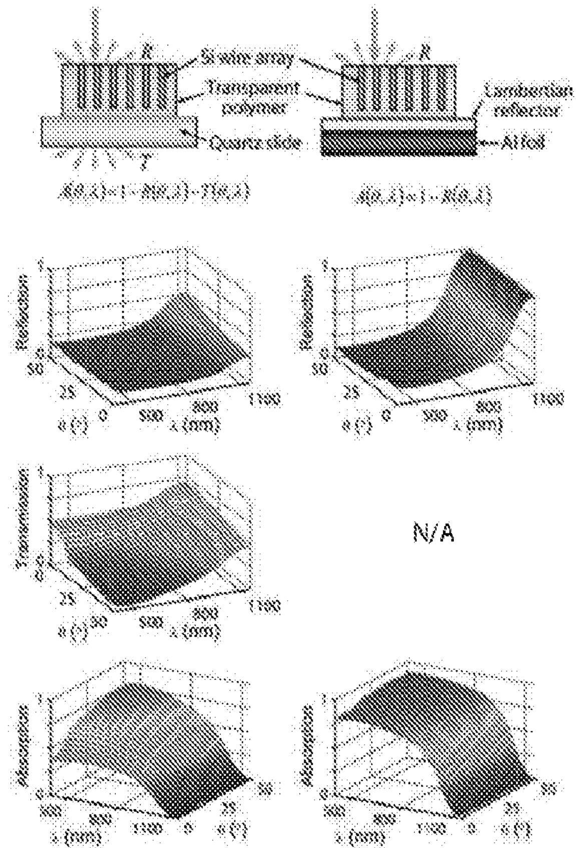

Figure S7. Example absorption measurements. Schematic (top row) and measurements of reflection (second row), transmission (third row), and absorption (bottom row) of a triangular-tiled wire array (η_f = 8.8%), placed on a quartz slide (left column) or a Lambertian back-reflector (right).

array (η_f = 8.8%, 68 μm wire length) are shown in Fig. S7. Similar measurements were performed on all wire arrays in this study.

In Eqns. (1) and (2), θ represents the direction of tilt during measurements, which was usually θ_x as defined in Fig. 1. Due to the angularly anisotropic optical properties of the periodic (e.g. square-tiled) wire arrays (see Fig. 2), it was important that each array be tilted in the same direction with respect to the lattice pattern of the wires—especially when combining angle-resolved reflection and transmission measurements to calculate absorption. Fiducial markings at the corner of each array provided approximate alignment marks; however to ensure reproducible orientation of the periodic arrays within the tilt plane, their transmitted (or reflected) diffraction patterns were used to align

each array's lattice pattern orientation to the match the convention depicted in Fig. 2. Furthermore, the specular reflection from each specimen was used to align the equipment to normal-incidence illumination conditions prior to each measurement.

Sub-bandgap absorption

Spectrally resolved measurements of the wire arrays were also performed at wavelengths exceeding the Si band edge (1150–1200 nm), where no band-to-band absorption is expected. In the absence of a back-reflector, the observed sub-bandgap absorption did not exceed -4% to +12%, and was typically below 5%. Some deviation from zero absorption (negative values in particular) can be attributed to an experimental artifact arising from the spatial variation in the array's optical density, because the transmission and reflection measurements were not necessarily performed at the same location on each wire array specimen. Variations of up to 0.08 in absolute transmission were observed across the wire arrays; however this artifact alone could not account for the larger instances of sub-bandgap absorption, nor that observed when the arrays were placed on the back-reflector (1–16%). Thus, this sub-bandgap absorption may be due to parasitic (non-photovoltaically useful) absorption processes. Parasitic absorption at above-bandgap wavelengths would be detrimental to any photovoltaic device, and must be addressed in this absorption study.

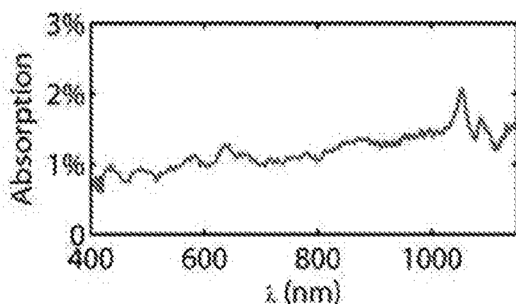

Figure S8. Integrated normal-incidence absorption of ~1-mm-thick PDMS film.

Free-carrier absorption is an intrinsic source of parasitic absorption within Si solar cells.[2] However the absorption due to free-carrier processes was likely negligible at these wavelengths, because most wires were nominally undoped, and the illumination levels were low (<< 1-sun equivalent intensity). Absorption due to the PDMS was also negligible: A relatively thick (est. 1 mm thick) film of cured PDMS exhibited absorption below ~0.02 throughout the measurement range (Fig. S8).

Others have reported sub-bandgap absorption in Au-catalyzed, VLS-grown Si wire arrays (up to ~0.6 at these wavelengths), and this has been primarily attributed to the presence of surface states, defects, or catalyst metal particles[3-5]. It is well-known that certain defects or impurities introduce energy levels or bands within a semiconductor's bandgap, and can give rise to extrinsic (trap-assisted) sub-bandgap absorption.[6] Known as the impurity photovoltaic (IPV) effect, this theoretically useful sub-bandgap absorption mechanism has been proposed and studied as route to exceed the efficiency limit of a single-junction solar cell,[7-9] particularly in non-planar junction geometries.[10-11]

The IPV effect has been experimentally observed at roughened Si surfaces[12] and for Au traps in bulk Si,[13-14] both of which may be present in Au-catalyzed, VLS-grown Si wires. However, IPV absorption has not yet been shown to produce an overall increase in efficiency vs. comparable conventional Si solar cells. Moreover, no sub-bandgap photogeneration has been reported for either surface-state-induced or Au-trap-induced IPV absorption within a purely photovoltaic device. Because of this, and the well-known deleterious properties of surface damage and deep-level traps within Si solar cells, we conclude that IPV absorption, if present, should not presently be considered useful for the purpose of estimating photovoltaic performance limits from absorption measurements.

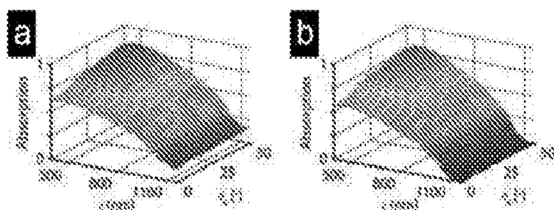

Figure S9. Example of scaling procedure, applied to the measurements of a triangular-tiled wire array (nf = 4.9%) that exhibited ~14% sub-bandgap absorption (placed on a Lambertian back-reflector). **a**, raw absorption data, and **b**, scaled absorption data.

Thus in this study it was assumed that observed sub-bandgap absorption, when present, was parasitic. Parasitic behavior at above-bandgap photon energies could not be determined from the optical measurements, because it cannot be distinguished from Si absorption. If present, however, the above-bandgap parasitic absorption should not be included in the estimation of a solar cell's sunlight utilization potential (A_{avg}), nor should it be included in the comparison of a wire array's absorption to planar absorption limits (as in Fig. 4). Thus to minimize the potential contribution of parasitic absorption to these analyses (as well as to mitigate the experimental artifact described above), the absorption of each wire array was scaled based on its observed sub-bandgap absorption. This was achieved by uniformly scaling (by up to 1.19x) the transmission and reflection measurements of each wire array, so as to produce an absorption (averaged from 1150–1200 nm) equal to that of a PDMS film (~0.01). An example of one of the most extreme cases of this scaling is shown in Fig. S9. Most wire arrays did not require substantial scaling (e.g. Fig 7, in which data appears unscaled.)

Note that the scaling procedure was not applied to the data used to calculate the I.Q.E. of the wire array electrode (Fig. 5), because this experiment sought to investigate parasitic absorption. Furthermore, no scaling was applied to any of the control measurements, or those of non-wire-array absorbers (e.g. the commercial Si solar cell of Figs. 3e and S11). Scaling was also not applied to the photoelectrochemical measurements of external quantum efficiency, since those measurements directly measure useful (non-parasitic) absorption.

It was not clear what caused some samples to exhibit sub-bandgap absorption, while others were virtually transparent at these wavelengths. Because each wire array was subject to identical etching conditions during processing, we suspect that this absorption may be due to entrapped particles of catalyst metal, rather than surface-state or bulk-trap assisted absorption as previously suggested. Catalyst metal inclusions have been observed in Au-catalyzed VLS-grown Si wires,[15] and it is known that Cu and Ni readily precipitate upon rapid cooling within crystalline Si.[16] Unfortunately, the cooling rate of wires following VLS growth varied greatly (and was not controlled) in this study.

Figure of merit calculations

Figure of merit definition

The figure of merit (FOM) utilized in this study calculates the approximate fraction of above-bandgap sunlight (i.e. photocurrent) that a wire array might absorb in a day of operation as a non-tracking solar cell. This calculation combines the angle- and wavelength- dependent absorption measurements $A(\theta,\lambda)$ of each wire array with a standard reference spectrum that specifies the photon flux of direct normal radiation (Γ) at each hour (t) and wavelength (λ) throughout the day[17]. This spectrum represents direct solar insolation typical of a summer day in the southwest U.S.*

Figure S10 depicts the FOM calculation and the associated simplifying conditions. We considered an absorbing device, tilted so as to face the sun at noon, but which did not otherwise track the sun (i.e. oriented at global tilt). The path of the sun across the sky was simplified as an equatorial arc; that is, confined within the equatorial plane such that a single angle $\theta_x(t)$ describes the incidence angle of direct sunlight throughout the day. In this case, $\theta_x = 0°$ at noon and progresses at 15°/hr. Under these assumptions, the fraction of above-bandgap incident photons that would be absorbed from this reference spectrum, A_{avg}, can be expressed as:

$$A_{avg} = \frac{\iint \Gamma(t,\lambda) A(\theta_x(t),\lambda) \cos(\theta_x(t))\, \mathrm{d}\lambda\, \mathrm{d}t}{\iint \Gamma(t,\lambda) \cos(\theta_x(t))\, \mathrm{d}\lambda\, \mathrm{d}t} \quad (3)$$

This calculation is performed for each wire array, over the range $400 < \lambda < 1100$ nm and $-50° < \theta_x < 50°$ (8:40 to 13:20). These limits are imposed by the spectral range of the illumination source ($\lambda_{min} = 400$ nm) and the Si band edge ($\lambda_{max} \sim 1100$ nm), as well as the

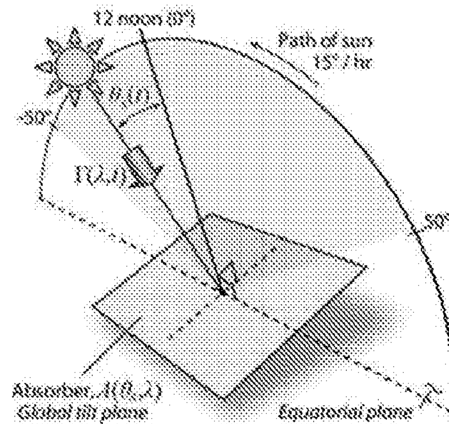

Figure S10. Schematic of FOM calculation

mechanical rotation limits of the integrating sphere. This integration range encompasses 255 mAH/cm² of the 305 mAH/cm² of above-bandgap photon-equivalent charge that would strike the global tilt plane under this reference spectrum and associated simplifying assumptions. This calculation (resolved by time of day, t) is plotted as Fig. 3e.

Although this figure of merit calculation effectively utilizes the full extent of the angle- and wavelength-dependent absorption measurements presented herein, it clearly is not a comprehensive model of solar cell efficiency, nor does it attempt to fully approximate realistic solar illumination. One primary limitation is that diffuse, global illumination (which can account for a majority of annual solar irradiation in some areas of the world) is not taken into account. Although a diffuse illumination profile could be broken down by wavelength and incidence angle to assess the absorption of a wire array, diffuse solar irradiation varies greatly by geography, time of day, season, atmospheric conditions, and numerous other factors. This is the subject of much research and modeling, and is beyond the scope of this study. Furthermore, the lack of wire array absorption data corresponding to > 50° incidence angles limits the extent to which the diffuse absorption could be evaluated.

* Note that the reference spectrum was time-shifted to yield maximum direct normal irradiation intensity at noon, to partially correct for differences between solar noon and local time of the reference conditions.

In this study, the omission of diffuse irradiation considerations is partially mitigated by the choice of a reference spectrum that is representative of a desert climate. Diffuse irradiation accounts for only ~10% of the total above-bandgap photon current striking the global tilt plane under the reference conditions. Furthermore, since diffuse sunlight strikes a solar cell from all angles, the day-integrated absorption of direct sunlight over ±50°, calculated herein is likely also a reasonable indicator of the wire array's effectiveness at absorbing diffuse sunlight.

Although our figure of merit makes several simplifying assumptions, does not consider diffuse illumination, and neglects additional output efficiency consideration (such as the cell operating voltage) it nevertheless provides an instructive gauge to compare the solar-energy utilization-potential of the wire arrays as a percentage of the theoretical limit of an ideally absorbing Si solar cell. To provide a reference point for this figure of merit calculation, we have also measured the absorption characteristics of a commercial, AR-coated, polycrystalline solar cell using the same integrating sphere apparatus (Fig. S11). This cell's figure of merit (A_{avg} = 0.87) is compared to those of the wire arrays in Fig. 3e.

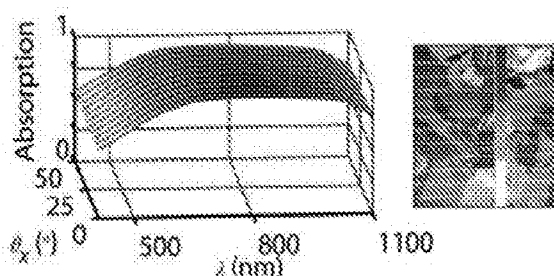

Figure S11. Measured integrated absorption of 280-μm-thick, commercial polycrystalline Si solar cell with dielectric AR-coating. Right: Photograph of ~2 cm square area of this solar cell.

Study of wire array geometry

In this study, 28 unique Si wire arrays were grown by a photolithographically patterned VLS process as previously described.[18] This was achieved using a photomask that included 28 unique hole array patterns derived from seven tiling patterns, with diameters of 3 or 5 μm and minimum pitch (center-to-center distance between adjacent holes) of 7, 9, or 12 μm. The tiling patterns included: periodic (square, triangular); chirped-periodic (square and triangular lattices where each wire had been randomly displaced by up to ±1 μm); quasi-periodic (Penrose, dodecagonal); and quasi-random (random placement of wires not less than the minimum pitch from one another). Wire length was nominally controlled by VLS growth time, however, arrays with higher areal packing fraction exhibited slower growth rates than those with lower packing fractions. In total, wire arrays of each of the 28 unique tiling patterns were grown, with packing fractions ranging from 1.6% to 16%, wire diameters ranging from 1.4 to 4.0 μm, and wire lengths ranging from 24 to 97 μm. The wire array specimens were approximately 5 mm × 5 mm in extent, and had varying optical properties visible to the naked eye (Fig. S12).

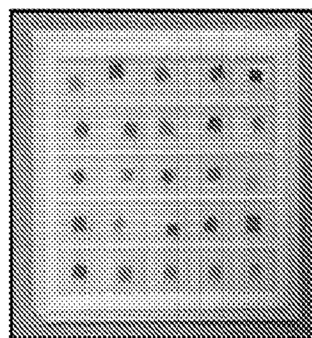

Figure S12. Digital photograph of several wire array samples (in no particular order) illustrating the variation in optical properties visible to the naked eye.

Figures S13a and S13b show the figures of merit for the wire arrays measured in this study, both with (b) and without (a) a Lambertian back-reflector; as a function of areal packing fraction, wire size, and array lattice pattern. The use of a Lambertian back reflector may overestimate the randomization of light that could be achieved by

a metallic back-reflector to a solar cell (which is why the Ag back-reflector used elsewhere in this study, see Figs. 3 and 4). However it was chosen here to approximate the absorption enhancement that was achieved by the use of light-scattering particles (e.g. Al_2O_3) elsewhere in this study, without requiring duplicate arrays to be fabricated with the embedded light-scattering particles.

In general, we found that arrays of moderate (8–10%) packing fraction achieved the highest values of A_{avg}. Although wire arrays with low packing fractions (< 7%) exhibited lower absorption, their A_{avg} values were often many times (10x–25x) their areal packing fractions, with the greatest $A_{avg}:\eta_f$ ratios corresponding to the longest (up to ~100 µm) wires. This enhancement likely arises from the inherent scattering and diffraction of light along the length of polymer-embedded wire arrays. The wire arrays with the highest packing fractions (12–16%) did not exhibit the greatest absorption, partially because these wires were shorter (~25 µm in length) as a result of a slower VLS growth rate observed for these arrays. Additionally, these dense-packed arrays exhibited greater reflectivity than the moderately packed arrays, presumably due to the increasing surface area of the reflective top surfaces of the wires. Thus, moderate (8–10%) packing fractions with longer (40–60 µm) wire lengths were found to optimize the tradeoff between optical opacity and low reflectivity.

Based on this study, it was determined that reasonable absorption could be obtained with relatively low (< 10%) areal packing fraction of wires. For convenience of growth and characterization, square-packed arrays of relatively long (>60 µm) wires were chosen for further study of optical absorption enhancement, including the use of AR-coatings and light-scattering particles.

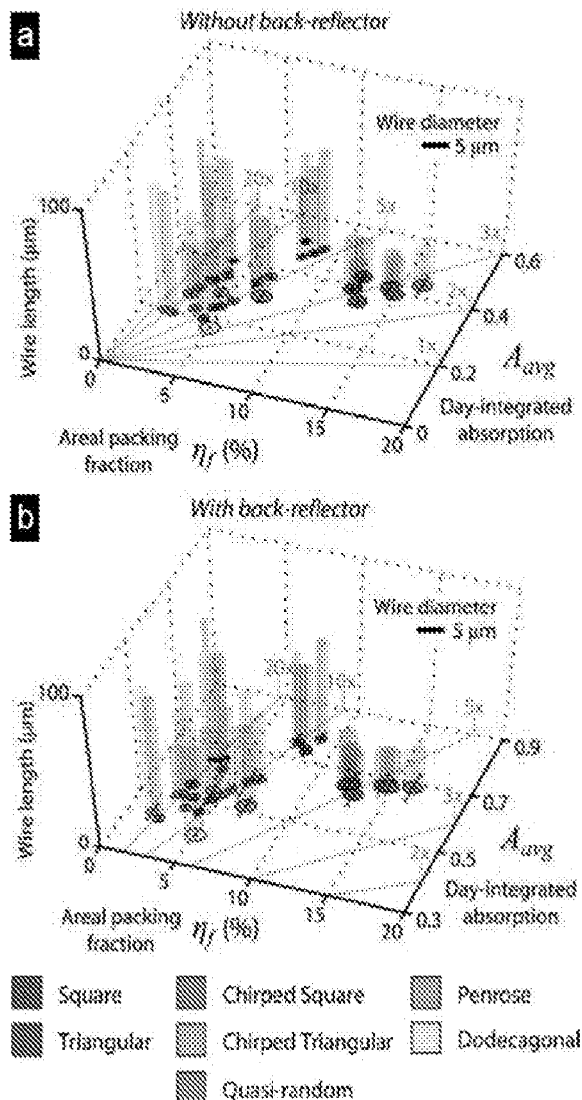

Figure S13. A_{avg} values for the wire arrays of this study, a, measured with no back reflector (quartz slide), and **b,** measured with a Lambertian (Ba_2SO_4) back-reflector. A_{avg} is plotted on the y-axis, as a function of the areal packing fraction, η_f (x-axis), wire length (cylinder height on z-axis), wire diameter (cylinder width vs. scale bar), and array lattice pattern (by color: red, triangular; blue, square; orange, chirped-triangular; purple, chirped-square; green, Penrose; yellow, dodecagonal; gray, quasi-random.) The gray lines indicate $A_{avg}:\eta_f$ ratios of 1, 2, 3, 5, 10, and 20, as labeled. A_{avg} error bars indicate the extent of any sub-bandgap absorption factor (discussed above); η_f error bars originate from the variance the diameters of the wires in each array.

Photoelectrochemical measurements

Photoelectrochemical cell

Figure S14 compares the electrochemical current-density-voltage data for the p-Si wire arrays with that for a photo-inactive conducting glassy carbon electrode. The measurements were performed in the methyl-viologen-containing electrolyte under illumination from an 808-nm laser diode. For the glassy carbon electrode, the onset of reduction current occurs at ~ -0.55 V vs. the Ag|AgCl reference electrode. Under illumination the photocurrent onset for the p-Si wire arrays occurs at a significantly more oxidizing potential, ~ -0.15 vs. Ag|AgCl, implying a photovoltage of ~0.4 V for this particular sample under these test conditions. Spectral response and external quantum efficiency measurements were made between -0.4 to -0.5 V vs. Ag|AgCl. In this potential regime the dark current measured at the glassy carbon electrode was negligible while the photocurrent response from the wire array was relatively flat and scaled linearly with incident light intensity. A detailed account of the energy conversion properties of similar p-Si wire array electrodes is given elsewhere.[18]

E.Q.E. measurements were performed under chopped (f = 30 Hz) illumination using lock-in detection to record the photocurrent from the wire-array electrode (and reject the contribution of dark current) as a function of wavelength.

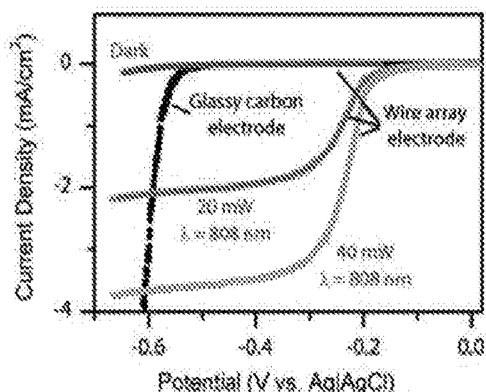

Figure S14. Current-voltage behavior of photoelectrochemical cell

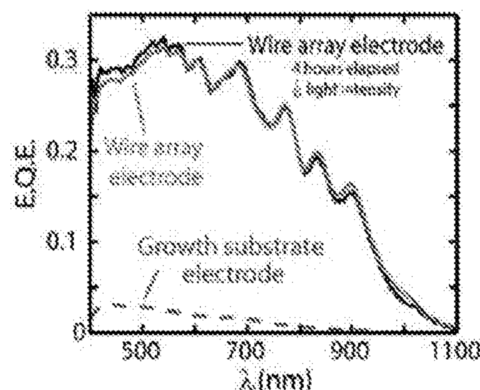

Figure S15. Photoelectrochemical E.Q.E. measurements of the wire-array electrode demonstrating experimental repeatability (red, black). Also shown is the E.Q.E. of the recovered wire-array growth-substrate electrode (blue).

The light source provided relatively low illumination levels (< 10 μA beam photocurrent), which avoided mass transport issues within the cell. The E.Q.E. measurements were repeated under varying light intensities and chop rates, over a course of several hours, with negligible difference in the recorded data (Fig. S15). The spectrally-resolved E.Q.E. measurements could be used to predict the J_{SC} of each wire-array electrode by weighting the observed E.Q.E. by the solar spectrum. This was performed to calculate $E.Q.E._{avg}$ (See Fig. S19).

Determination of I.Q.E.

In this study, the internal quantum efficiency (I.Q.E.) of a radial-junction wire array device was calculated by normalizing the E.Q.E. of a wire array electrode in a photoelectrochemical cell to the optical absorption of a nominally identical, peeled-off wire array. A control electrode was fashioned from the growth substrate of a similarly grown wire array of nearly identical geometry. This wire array had been embedded in PDMS and peeled-off (Fig. 5b, inset right), allowing its optical absorption to be measured. The recovered growth substrate

(Fig. S16, inset) was prepared as an electrode and used for two control experiments.

First, Fig. S15 shows the E.Q.E. of the recovered growth-substrate electrode when measured under identical conditions in the photoelectrochemical cell. The E.Q.E. of the growth substrate was very low (below 0.04) throughout the measurement range, as expected for degenerately doped p^+-Si contaminated with VLS-growth catalyst. The contribution of the growth substrate to the measured E.Q.E. of the wire-array electrodes was likely even less than this, because the wire arrays would partially shade this underlying substrate. Furthermore, a portion of the observed growth-substrate electrode response was likely due to the wire stubs remaining on the growth substrate. Thus, it can be reasonably assumed that the measured E.Q.E. of the wire array electrode corresponds closely to the photoresponse of the wires themselves.

Second, the reflectivity of the recovered growth-substrate was measured (Fig. S16.) The relatively low reflectivity (0.04–0.16) suggests that the growth wafer beneath the wire array electrode did not contribute significantly as an optical back-reflector.

These control experiments validated our approach in approximating the I.Q.E. of the wire array electrode by comparing its E.Q.E. (measured on the growth substrate) to the optical absorption of the identically grown, peeled-off wire array (measured on a quartz slide). Only small differences existed between these experimental configurations. The peeled-off array, embedded in a polymer film of refractive index, $n \approx 1.42$, was placed on a quartz slide (typically exhibiting a reflectivity of ~0.08) for measurement, with a small gap between slide and the array. The wire array electrode, immersed in an electrolyte solution of $n \approx 1.33$ for measurement, remained on its growth substrate with the approximate maximal reflectivity of 0.04–0.15 shown in Fig. S4.

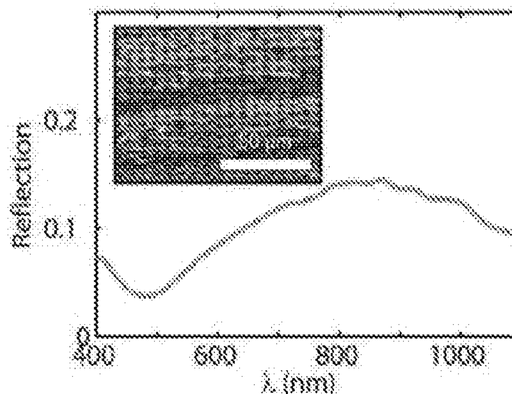

Figure S16. Reflectivity of the growth substrate following peel-off. Inset: SEM image of the recovered growth substrate, remaining wire stubs, and residual PDMS layer (viewed at 45°)

The optical properties of both the wire-array electrode and the peeled-off wire array were highly dependent on the incidence angle of illumination. To assure that the optical and photoelectrochemical measurements were performed at the same illumination incidence angle, θ_t and θ_g were tuned to yield the minimum transmission and E.Q.E., respectively. This corresponded to normal-incidence illumination under both measurement configurations.

At infrared wavelengths (λ > 900 nm), the calculated I.Q.E. deviated from unity, whereas radial-junction theory predicts no such decline for wires of this diameter.[20] We believe that this is likely due to the experimental differences between the absorption and E.Q.E. measurement configurations. Infrared light is weakly absorbed in Si, and thus could be guided to reach the bottom of the wires before being completely absorbed. In the peeled-off configuration, light reaching the bottom of the wires would experience a partial reflection due to the Si/air dielectric interface (~0.32) which could increase absorption. However, light that reaches the bottom of the wires in the electrode configuration would experience no reflection, and would instead be transmitted into (and absorbed within) the thick, photovoltaically inactive growth wafer. This partially explains the drop in inferred I.Q.E. at wavelengths exceeding ~900 nm.

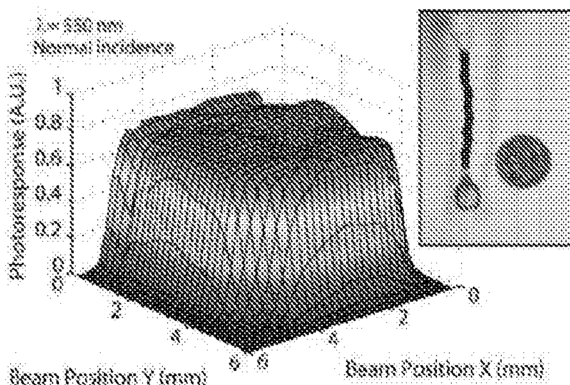

Figure S17. Spatial E.Q.E. uniformity of a wire array electrode. Inset: photograph of wire array electrode.

Supplementary E.Q.E. measurements

Figure S17 demonstrates the spatial uniformity of the E.Q.E. of a Si wire array electrode. In this experiment, the electrode was rastered across a λ = 550 nm beam (approx. spot size of 1 mm²) at normal incidence. No more than ±10% variation in E.Q.E. was observed across the entire device area, indicating excellent uniformity of array geometry and electrical properties.

Figure S18 shows the two-dimensional, angle-resolved E.Q.E. of a square-tiled wire array electrode at λ = 550 nm and λ = 800 nm. The high pattern fidelity of this wire array gave rise to an E.Q.E. profile which was highly dependent on incidence angle. The E.Q.E. was substantially lower at illumination angles parallel to the rows or columns of wires within the array. By convention, most of the absorption/E.Q.E. measurements in this study were performed by varying θ_x with $\theta_y = 0°$, which traverses the

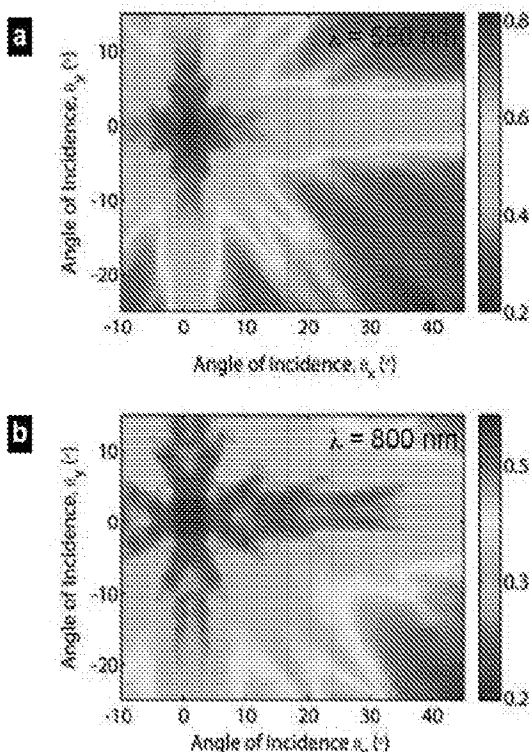

Figure S18. Angle-resolved E.Q.E. of square-tiled wire array electrode, measured at **a**, λ = 550 nm, and **b**, λ = 800 nm.

angles where periodic arrays exhibit minimal absorption/E.Q.E. Thus we note that many of the wire arrays in this study might exhibit increased absorption/E.Q.E. if they were simply oriented differently 8/within the measurement plane. This effect was partially realized by the wire-array electrode of Fig. 5b, which was oriented ~40° compared to the convention followed elsewhere in this study.

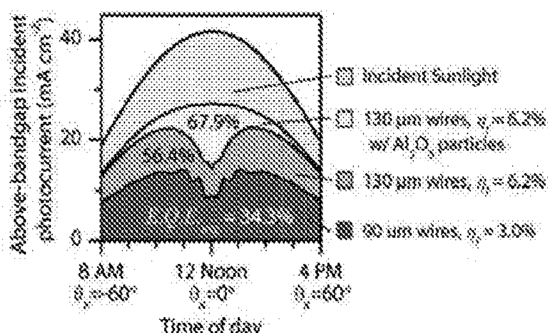

Figure S19. Illustration of $E.Q.E._{avg}$ calculations corresponding to measured wire array electrodes.

E.Q.E. figure of merit

To provide a figure of merit for the E.Q.E. of a wire array electrode, the A_{avg} calculation (defined previously) was performed on the measured E.Q.E. (rather than absorption) of each wire-array electrode, to yield a day-integrated value of external quantum efficiency, $E.Q.E._{avg}$. Fig. S19 illustrates the evaluation of this figure of merit for the wire arrays investigated here. The effectiveness of the Al_2O_3 light-scattering particles can be clearly seen in the improved normal-incidence response of the 130-μm-long wire-array electrode.

References

1 Forouhi, A. R. & Bloomer, I. Optical dispersion relations for amorphous semiconductors and amorphous dielectrics. *Physical Review B* **34**, 7018 (1986).

2 Tiedje, T., Yablonovitch, E., Cody, G. D. & Brooks, B. G. Limiting efficiency of silicon solar-cells. *IEEE Trans. Electron Devices* **31**, 711-716 (1984).

3 Tsakalakos, L. *et al.* Silicon nanowire solar cells. *Appl. Phys. Lett.* **91**, 233117-233113 (2007).

4 Tsakalakos, L. *et al.* Strong broadband optical absorption in silicon nanowire films. *Journal of Nanophotonics* **1**, 013552-013510 (2007).

5 Stelzner, T. *et al.* Silicon nanowire-based solar cells. *Nanotechnology*, 295203 (2008).

6 Pankove, J. I. *Optical processes in semiconductors.* (Prentice-Hall, Inc, 1971).

7 Guttler, G. & Queisser, H. J. Impurity photovoltaic effect in silicon. *Energy Conversion* **10**, 51 (1970).

8 Wolf, M. Limitations and Possibilities for Improvement of Photovoltaic Solar Energy Converters: Part I: Considerations for Earth's Surface Operation. *Proceedings of the IRE* **48**, 1246-1263 (1960).

9 Shockley, W. & Queisser, H. J. Detailed balance limit of efficiency of p-n junction solar cells. *J. Appl. Phys.* **32**, 510-519 (1961).

10 Keevers, M. J. & Green, M. A. in *Photovoltaic Specialists Conference, 1993., Conference Record of the Twenty Third IEEE.* 140-146.

11 Brown, A. S. & Green, M. A. Impurity photovoltaic effect: Fundamental energy conversion efficiency limits. *J. Appl. Phys.* **92**, 1329-1336 (2002).

12 Huang, Z. *et al.* Microstructured silicon photodetector. *Appl. Phys. Lett.* **89**, 033506-033503 (2006).

13 Sah, C. T., Tasch, A. F. & Schroder, D. K. Recombination properties of the gold acceptor level in silicon using the impurity photovoltaic effect. *Phys. Rev. Lett.* **19**, 71 (1967).

14 Guttler, G. & Queisser, H. J. Photovoltaic effect of gold in silicon. *J. Appl. Phys.* **40**, 4994-4995 (1969).

15 Wagner, R. S. Defects in silicon crystals grown by the VLS technique. *J. Appl. Phys.* **38**, 1554-1560 (1967).

16 Seibt, M. & Graff, K. Characterization of haze-forming precipitates in silicon. *J. Appl. Phys.* **63**, 4444-4450 (1988).

17 Marion, B. *et al.* Validation of a photovoltaic module energy ratings procedure at NREL. Report No. NREL/TP-520-26909, (1999).

18 Kayes, B. M. *et al.* Growth of vertically aligned Si wire arrays over large areas (> 1 cm^2) with Au and Cu catalysts. *Appl. Phys. Lett.* **91**, 103110-103113 (2007).

19 Boettcher, S. W. *et al.* Energy-conversion properties of vapor-liquid-solid-grown silicon wire-array photocathodes. *Submitted* (2009).

20 Kelzenberg, M. D., Putnam, M. C., Turner-Evans, D. B., Lewis, N. S. & Atwater, H. A. in *Photovoltaic Specialists Conference, 2009. PVSC '09. 34th IEEE.* 1-6.

CLAIMS

1. A structure comprising:

an array of elongated semiconductor elements;

an infill material located in a space between the elongated semiconductor elements; and

a reflective material, configured to reflect incident light and direct the incident light to the elongated semiconductor elements.

2. The structure of claim 1, wherein the reflective material is a metal material.

3. The structure of claim 1 or 2, including a light scattering texture applied to the reflective material.

4. The structure of any one of the preceding claims, including a light concentrating texture applied to the reflective material.

5. The structure of any one of the preceding claims, wherein the elongated semiconductor elements extends from a substrate, and the reflective material is interposed between the infill material and the substrate.

6. The structure of any one of the preceding claims, wherein the reflective material also transmits at least some of the light at photon energies below that of a semiconductor bandgap energy.

7. A structure comprising:

an array of elongated semiconductor elements;

an infill material located between the elongated semiconductor elements; and

an antireflective coating at least partially and superficially covering a respective elongated semiconductor element, the antireflective layer being interposed between the infill material and the respective elongated semiconductor element.

8. The structure of claim 7, further comprising a plurality of antireflective coatings, wherein each coating at least partially and superficially covers the respective elongated semiconductor element.

9. The structure of claim 7 or 8, wherein the antireflective coating varies in thickness along a surface of the elongated semiconductor elements.

10. The structure of claim 7 or 8, wherein the antireflective coating varies in composition along a surface of the elongated semiconductor elements.

11. The structure of any one of claims 7 to 10, further comprising light scattering material applied on the antireflective coating.

12. A structure comprising:

an array of elongated semiconductor elements;

an infill material located in a space between the elongated semiconductor elements; and

a light scattering material included in the infill material and surrounding the elongated semiconductor elements.

13. The structure of claim 12, wherein the infill material includes an infill bottom zone closer to a bottom of the structure than to a infill top zone, and wherein a concentration of the light scattering elements is higher in the infill bottom zone than in the infill top zone, the bottom of the structure being opposite to a zone exposed to incident light.

14. The structure of claim 12 or 13, wherein the light-scattering elements comprise one element selected from the group including void, bubble, dielectric composition, particle of metal, and a polymer.

15. The structure of claim 14, wherein the dielectric composition comprises one element selected from the group including Al_2O_3, $BaSO_4$, TiO_2, SiO_2.

16. The structure of claim 14, wherein the particle of metal comprises one element selected from the group including Ag, Au, Ni, Al and Cu.

17. The structure of any one of claims 13 to 16, wherein the elongated semiconductor elements have minor dimension of at least 1 μm.

18. The structure of any one of claims 13 to 16, wherein the array of elongated semiconductor elements has a packing fraction less than 10%.

19. A structure comprising:

an array of substantially vertically oriented elongated semiconductor elements;

an infill material located in a space between the elongated semiconductor elements; and

a material applied at least partially on a surface of the infill material, said material being selected from the group consisting of: light scattering material, concentrating material, and a texture.

20. A solar cell comprising the structure of any one of claims 1-19.

21. A photoconverter device, comprising:

a top transparent contact,

a bottom metal contact, and

the structure of any one of claims 1 to 19, interposed between the top transparent contact and the bottom metal contact, wherein the bottom metal contact also serves in part or in whole as the reflective material of said structure.

22. A photoelectrochemical device comprising a liquid electrolyte solution and the structure of any one of claims 1 to 19 placed in the liquid electrolyte solution, wherein the liquid electrolyte partially or wholly comprises the infill material of said structure.

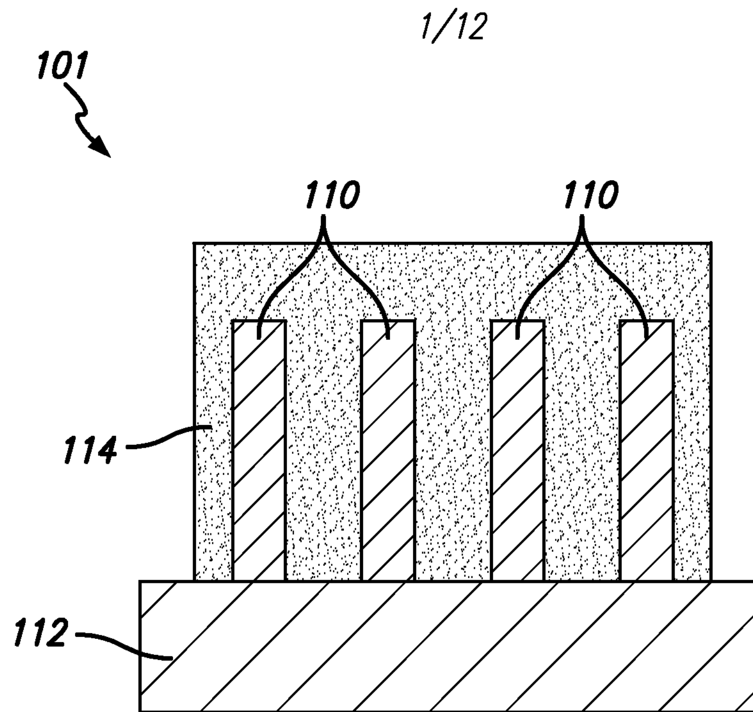

FIG. 1

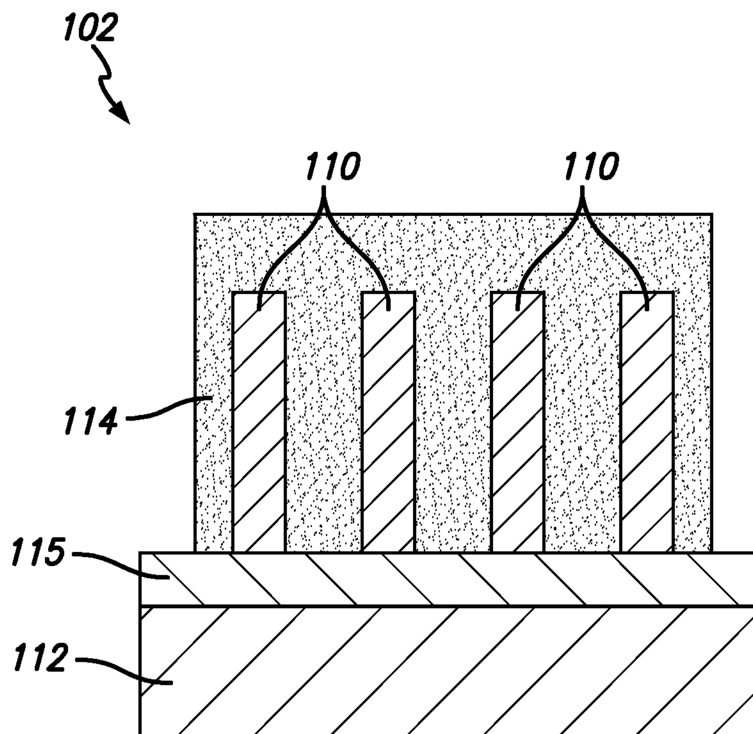

FIG. 2

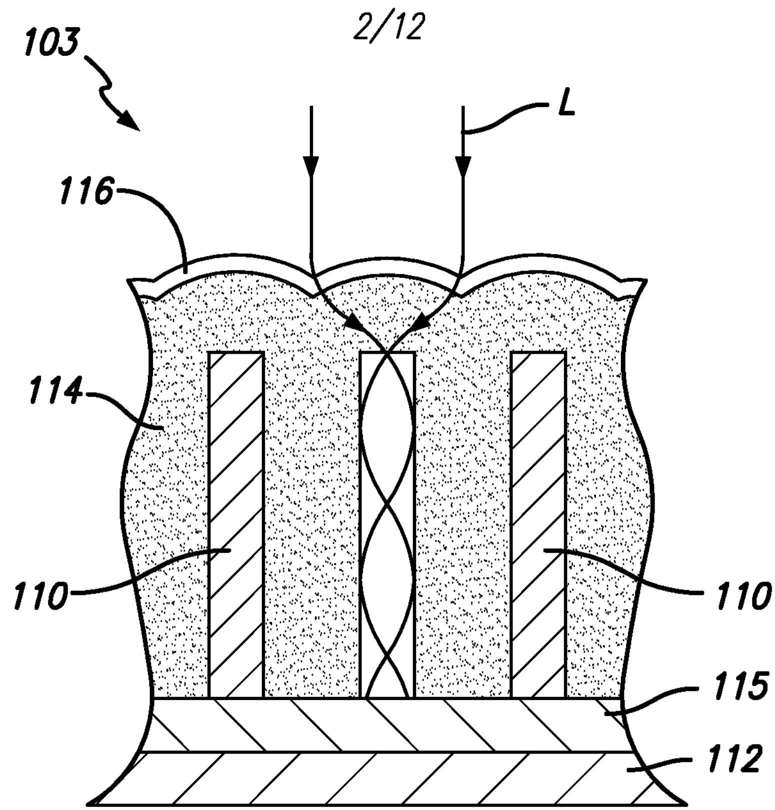

FIG. 3

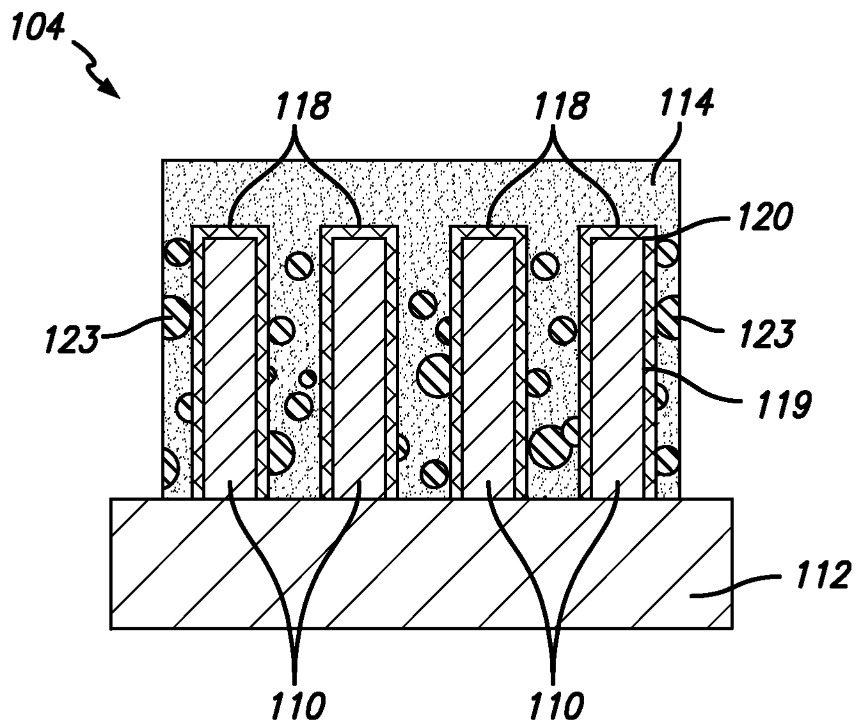

FIG. 4

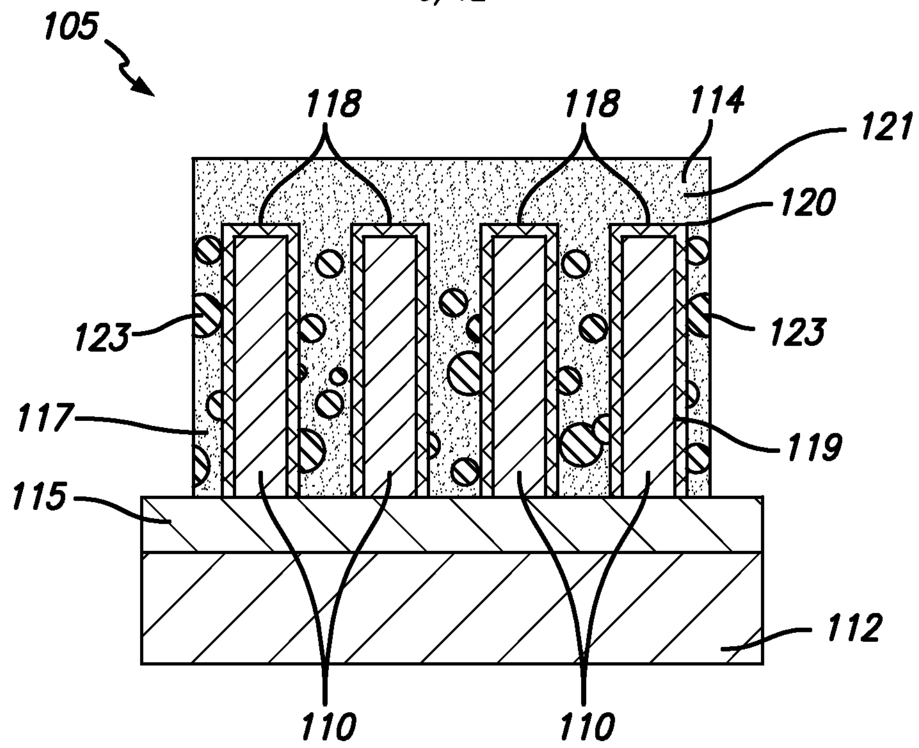

FIG. 5

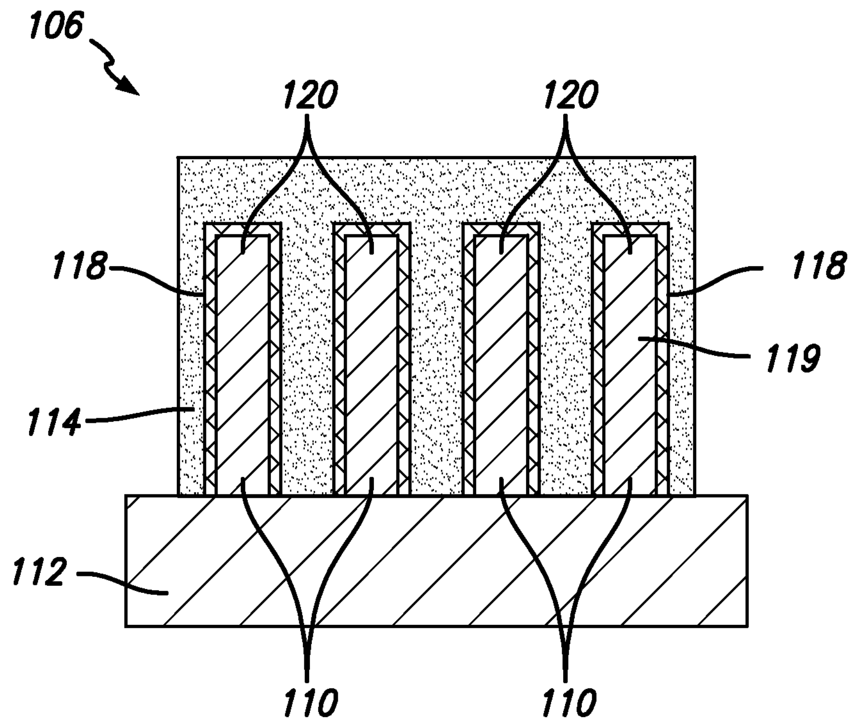

FIG. 6

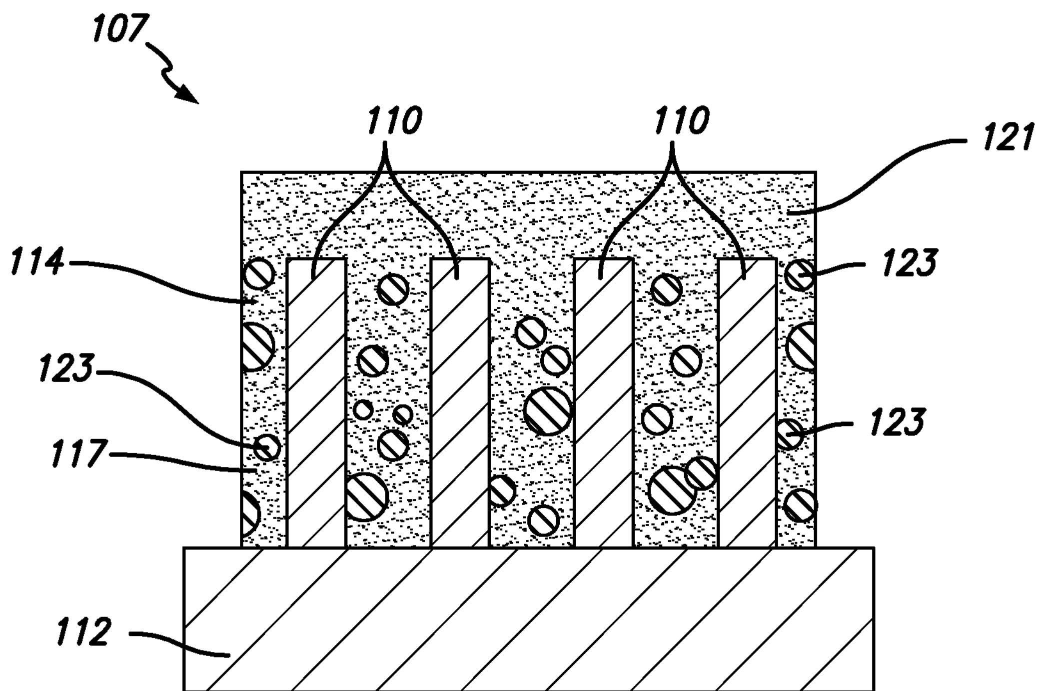

FIG. 7

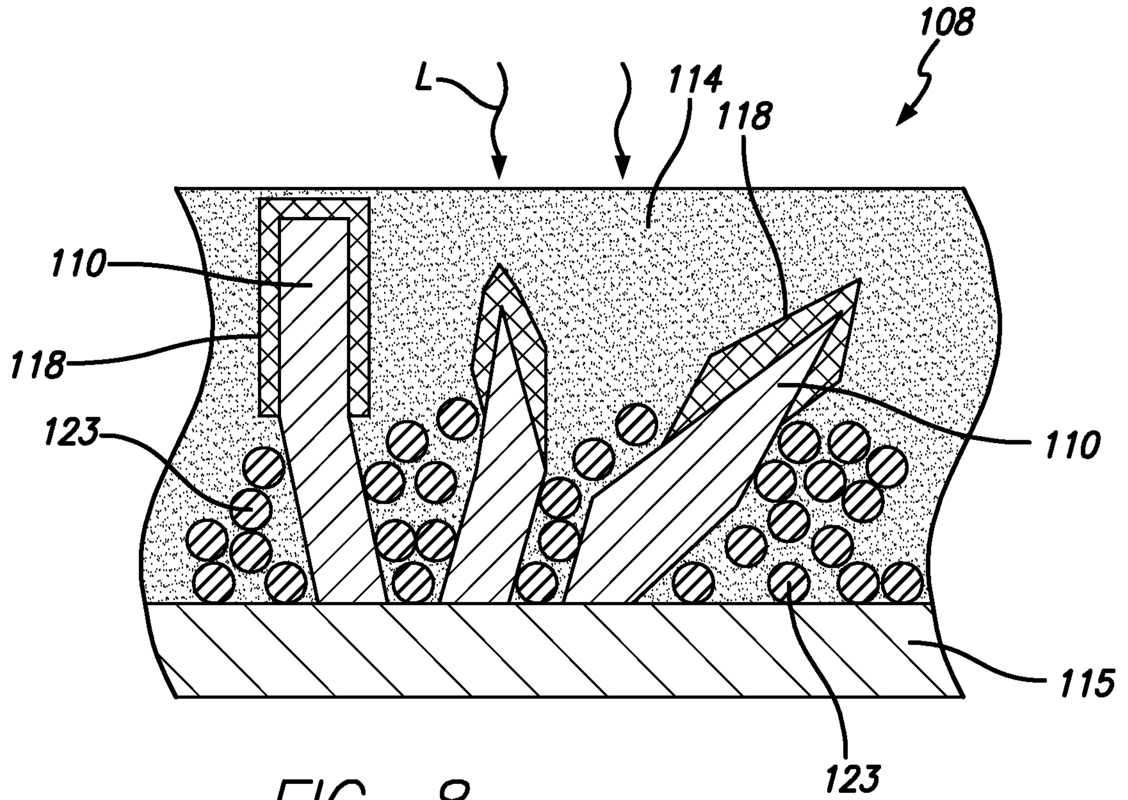

FIG. 8

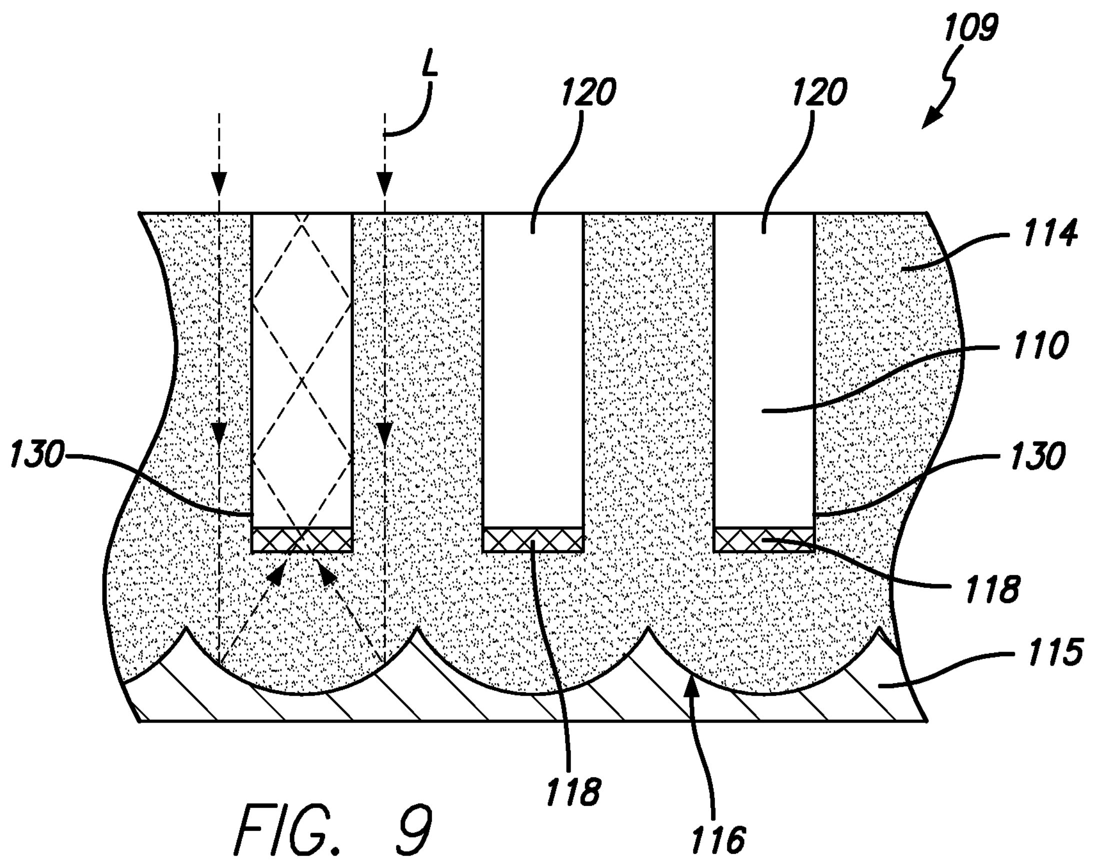

FIG. 9

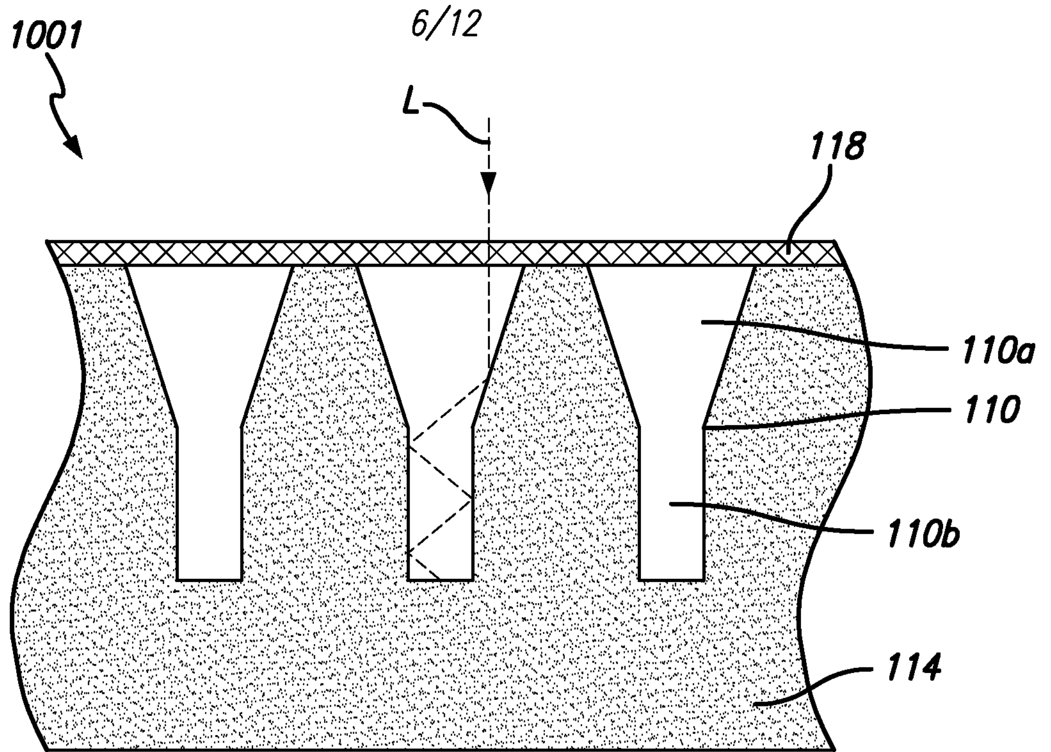

FIG. 10

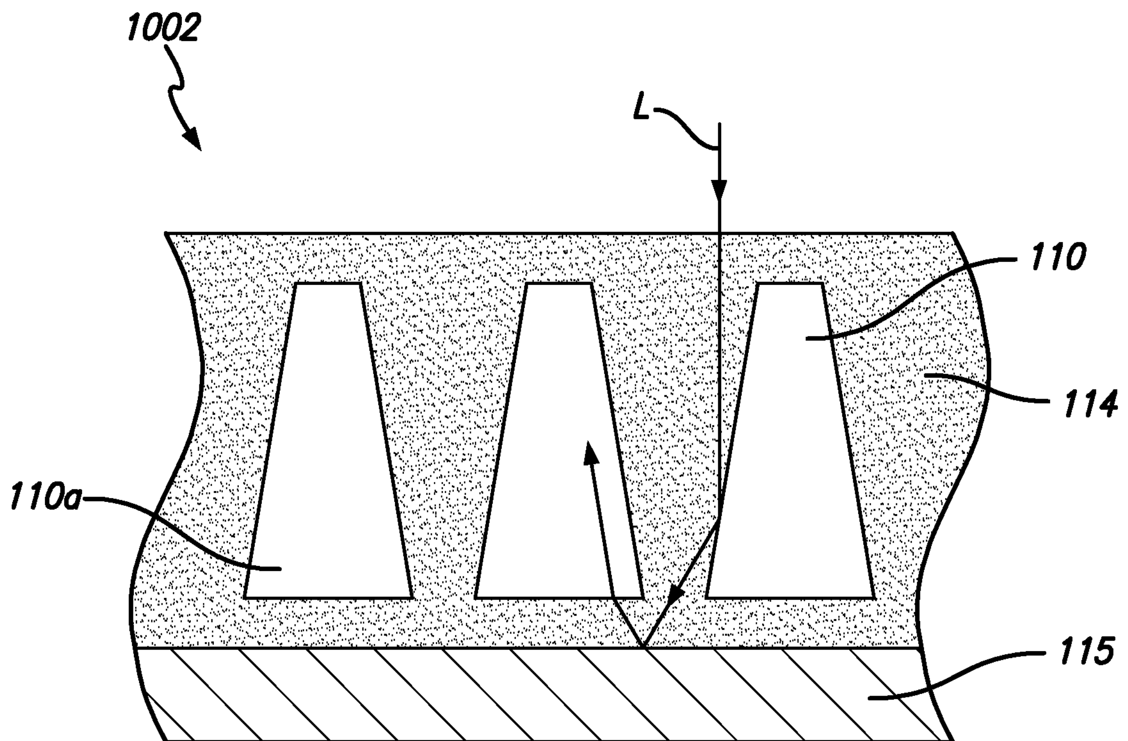

FIG. 11

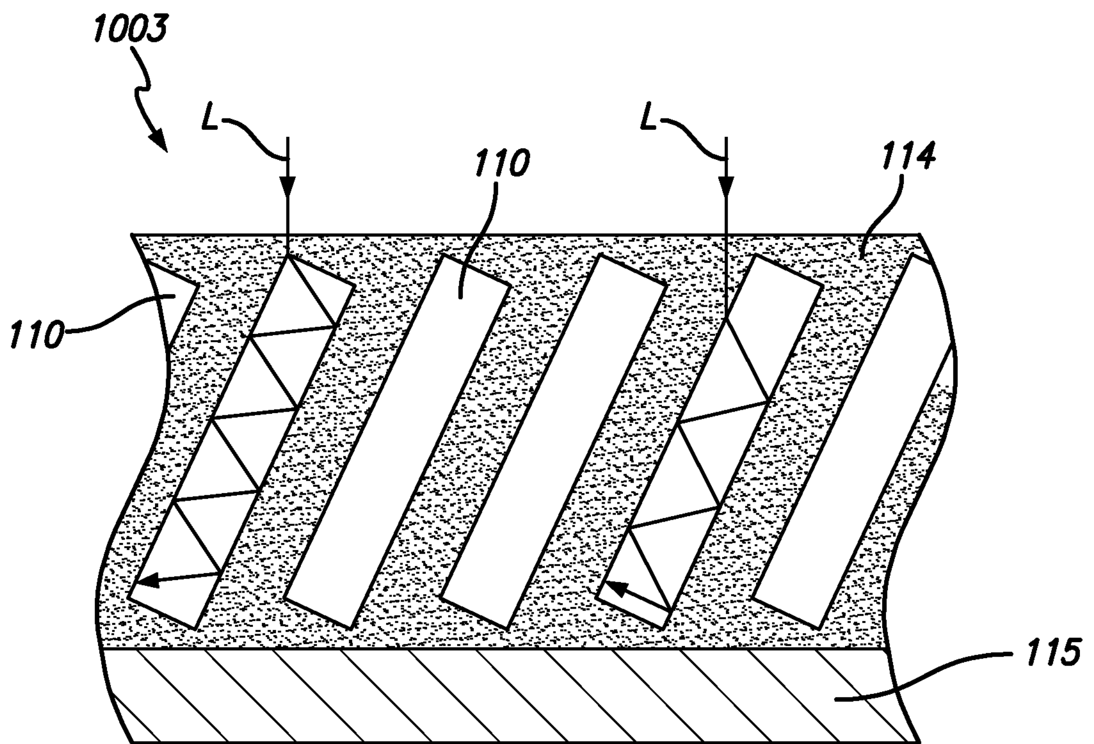

FIG. 12

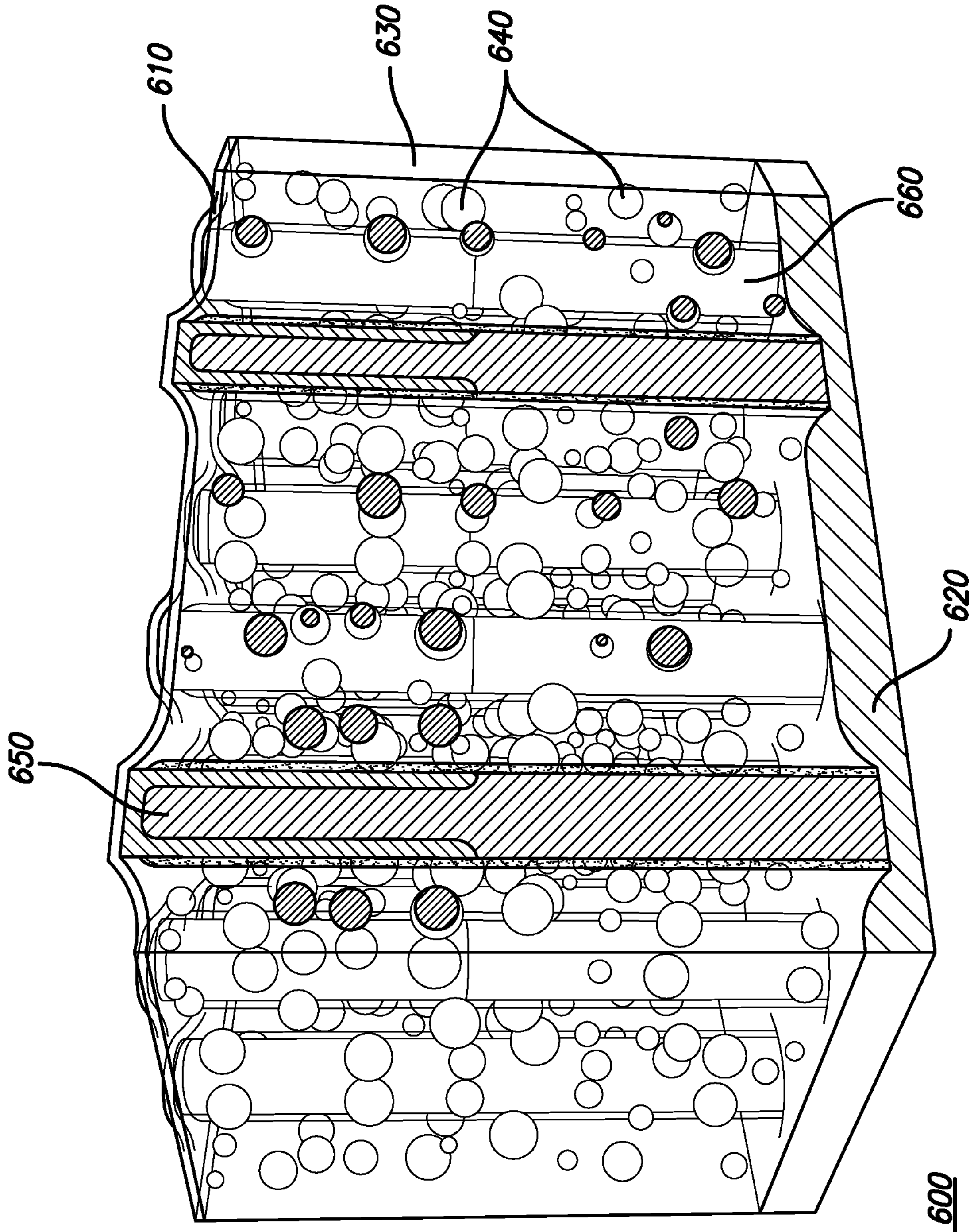

FIG. 13

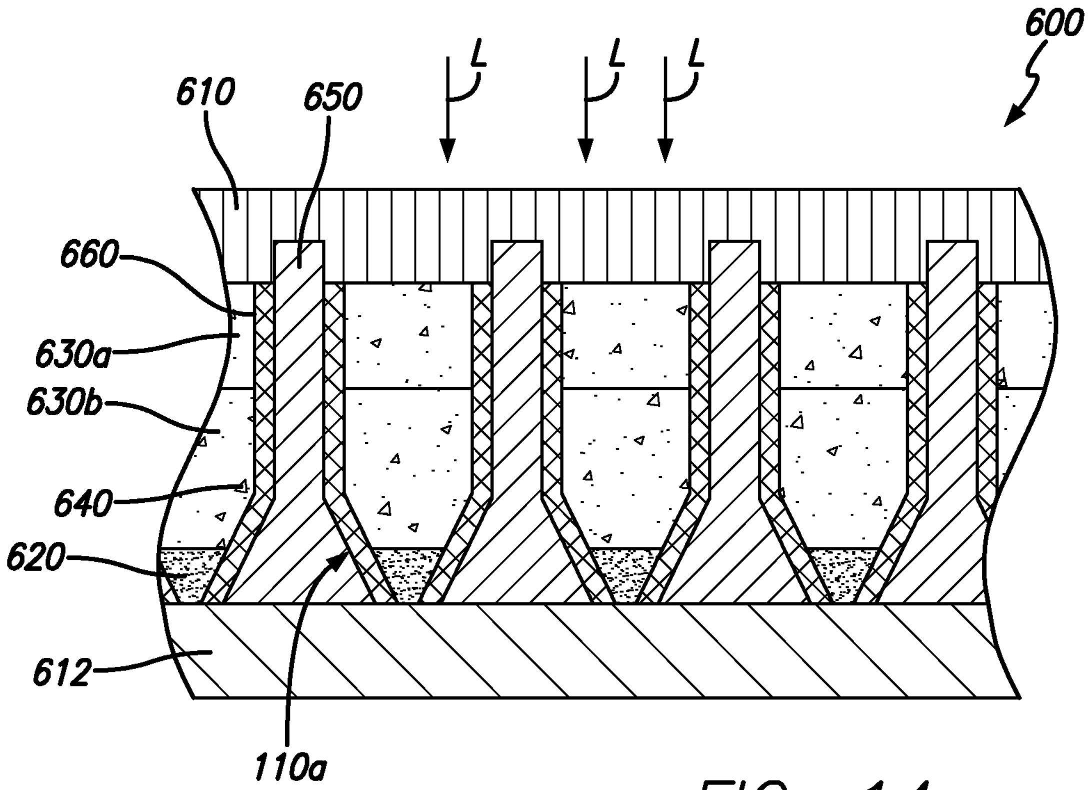

FIG. 14

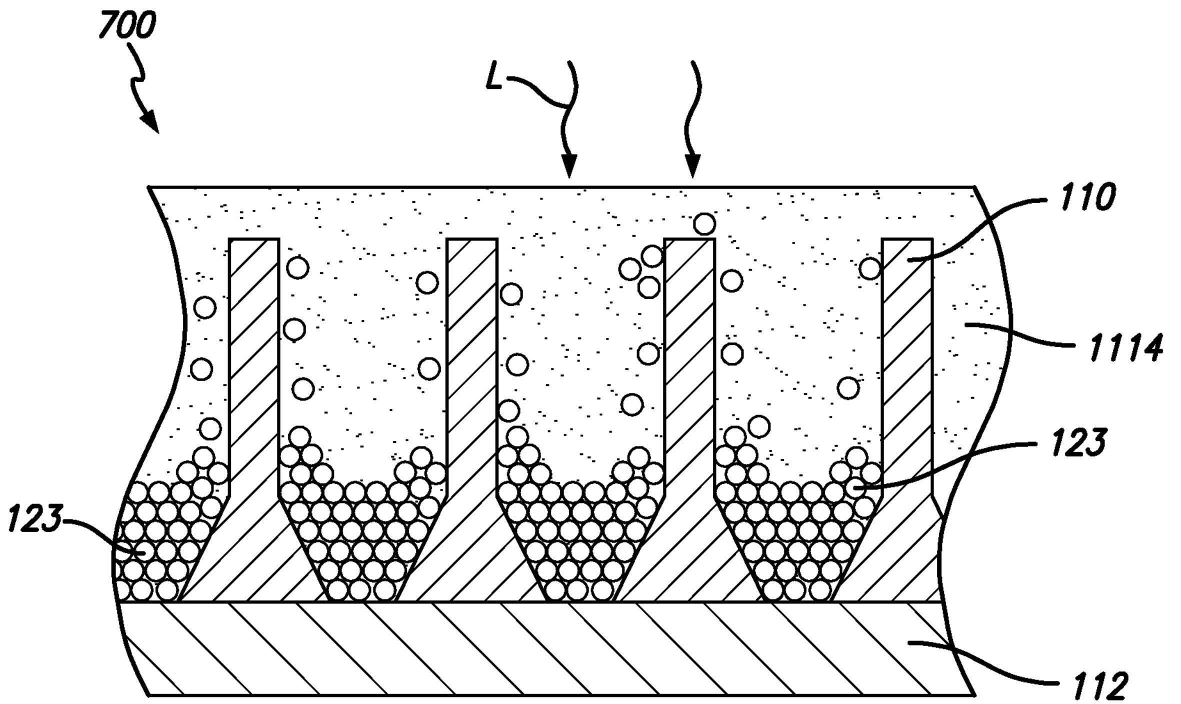

FIG. 15

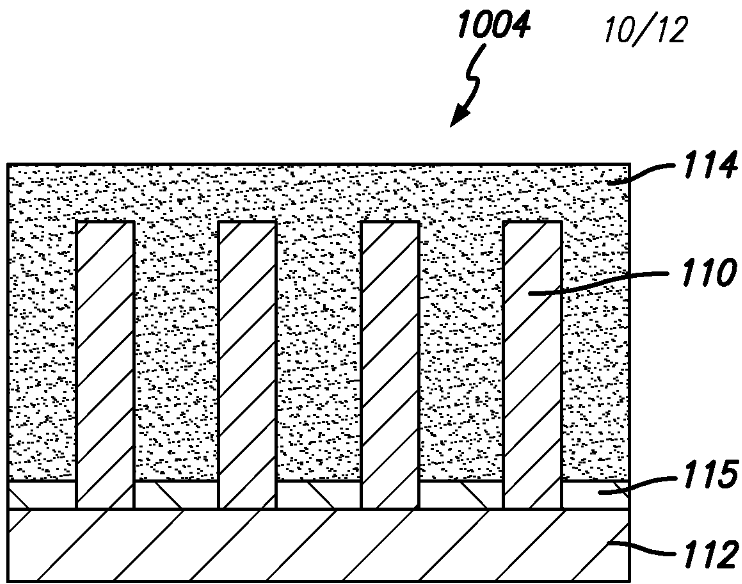

FIG. 16

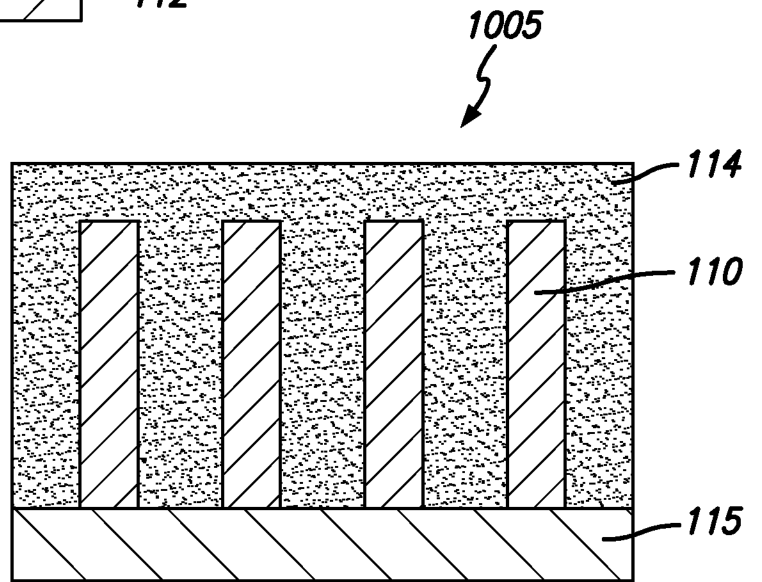

FIG. 17

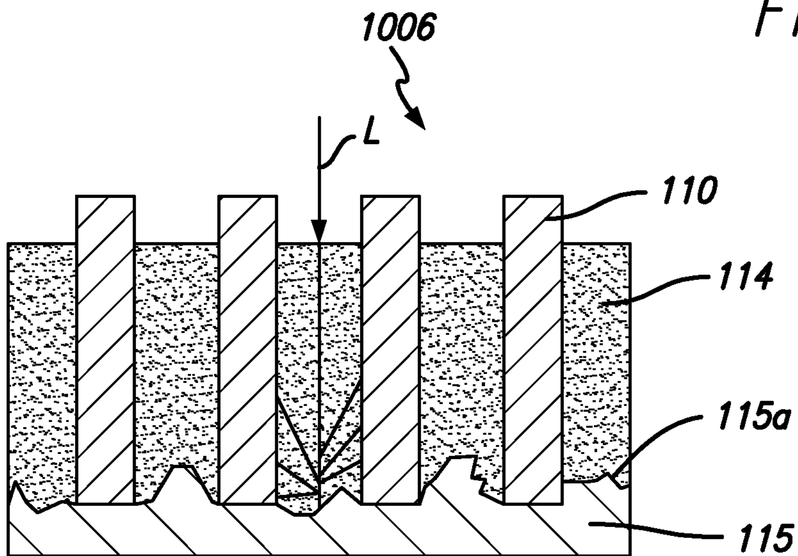

FIG. 18

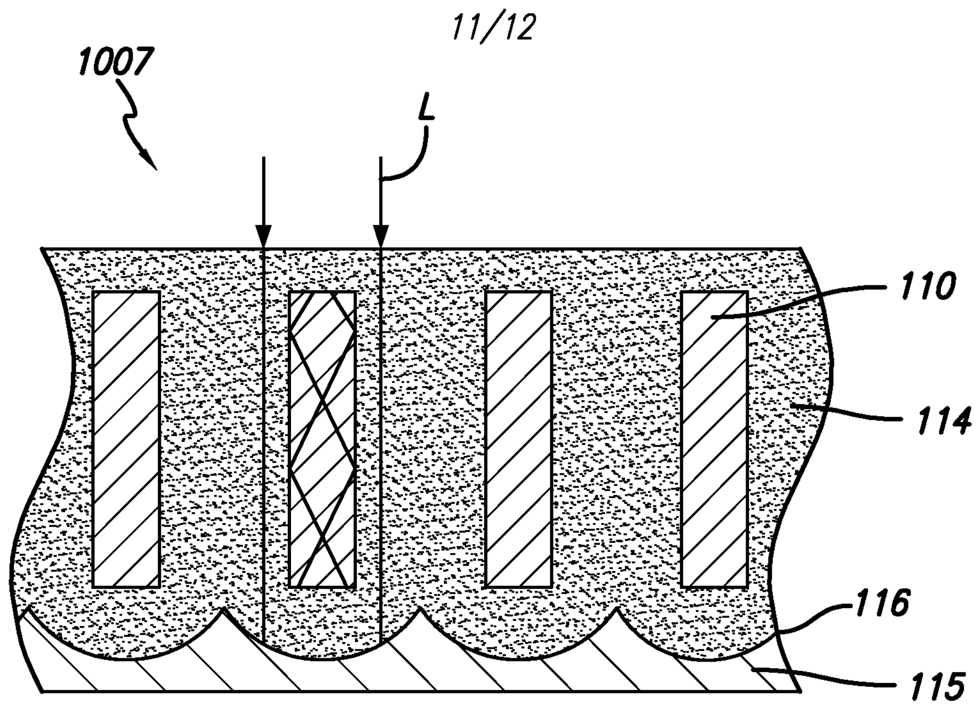

FIG. 19

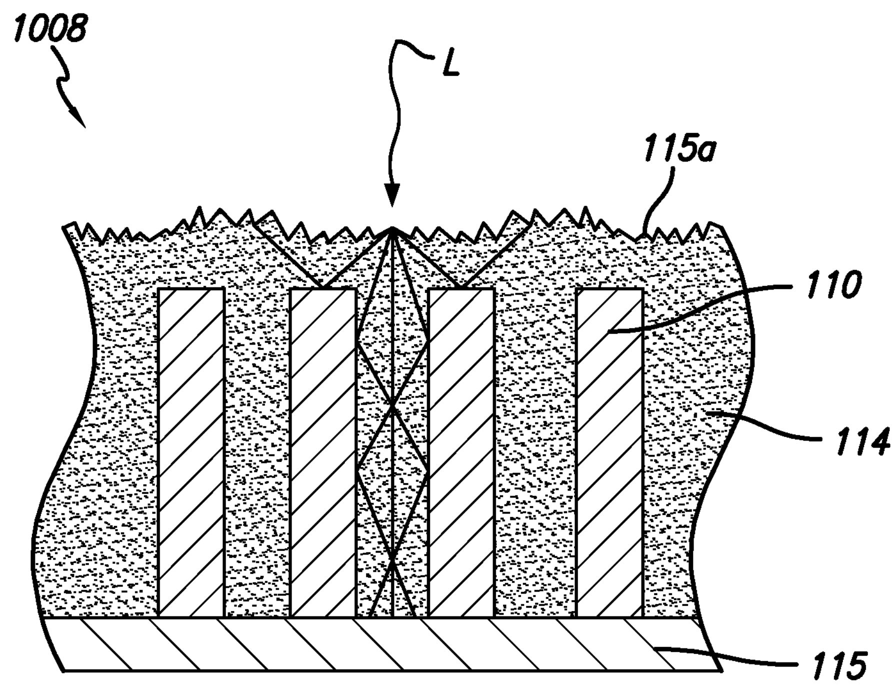

FIG. 20

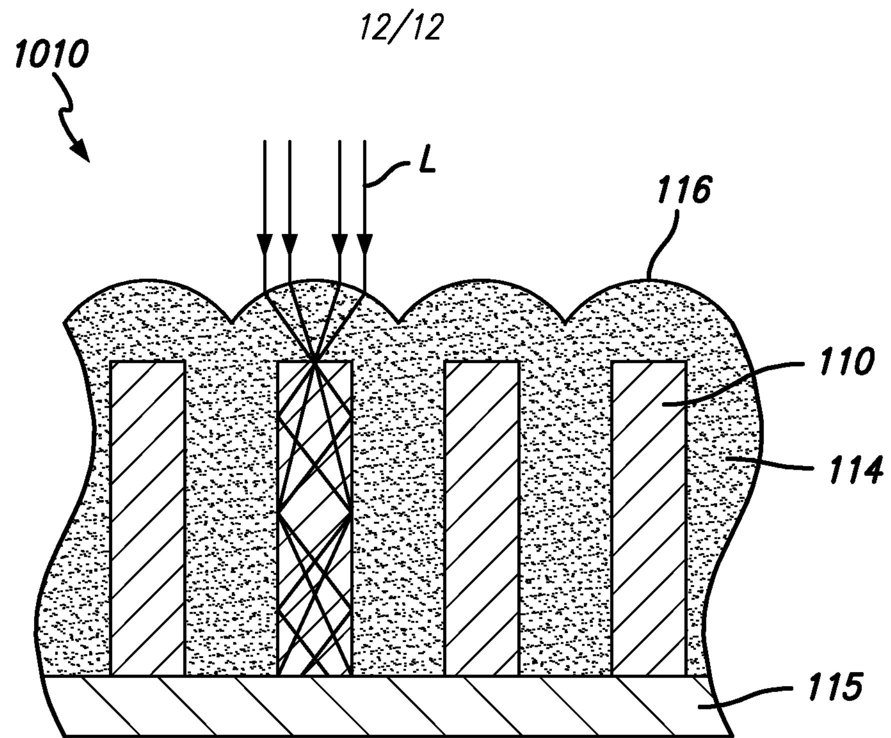

FIG. 21

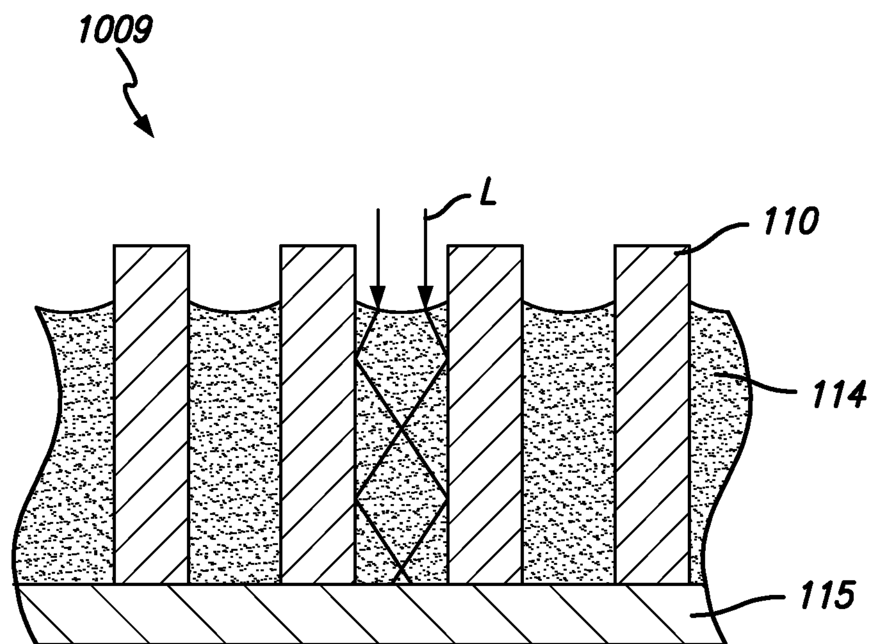

FIG. 22